Novel manufacturing approaches to solid-state batteries



Christopher Dörrer

Mansfield College

University of Oxford

A thesis submitted for the degree of
Doctor of Philosophy

Michaelmas 2022

Supervised by

Prof P. S. Grant & Prof M. Pasta

Novel manufacturing approaches to solid-state batteries

Christopher Dörrer

Mansfield College
University of Oxford

A thesis submitted for the degree of Doctor of Philosophy

Michaelmas 2022

Abstract

All-solid-state batteries (SSBs) based on sulfide solid electrolytes (SEs) have the potential to increase safety and provide greater energy density compared to lithium-ion batteries (LIBs). To match the high capacity of metallic anodes, SSBs require high energy density, long-lasting composite cathodes such as those based on lithium Ni-Mn-Co (NMC) oxide mixed with a solid-state electrolyte (SE). However in practice, cathode capacity typically fades due to NMC cracking and increasing NMC/SE interface debonding because of NMC pulverization. Using smart processing protocols, a single-crystal particulate $LiNi_{0.83}Mn_{0.06}Co_{0.11}O_2$ and Li_6PS_5Cl SE composite cathode was fabricated with outstanding discharge capacity of 210 mA h g^{-1} and high areal capacity of 8.7 mA h cm^{-2} at 30 °C. A first cycle coulombic efficiency of >85%, and >99% thereafter, was achieved despite a 5.5% volume change during cycling.

Many battery applications target fast charging that increase the state of charge (SOC) to at least 80% in <15 min. However, most SSBs take several hours to reach >80% SOC and a typical specific energy of 400 W h kg_{cell}^{-1}. This arises because of current density limitations at the anode and high interfacial resistances in the cathode, leading to high overpotentials even at elevated temperature. The fast-charging capability of a low resistance sulfide based single crystal NMC all-solid-state cathode was investigated using a 3-electrode arrangement that allowed differentiation between anodic and cathodic contributions. At 30 °C and charging at 15 mA cm^{-2}, a specific capacity of 150 mA h g^{-1} in ∼8 min was achieved, with 80% capacity retention after 3000 cycles. There was a low void formation rate during cycling highlighting the importance of optimized cathode fabrication. At 80 °C, a current density of 50 mA cm^{-2} charged a cathode areal capacity of 8 mA h cm^{-2} in only 10 min, suggesting SSB cathodes for fast charging at 400 W h kg_{cell}^{-1} may be within reach.

Although there has been steady improvements in the performance of SSBs, most research has focused on small (∼10 mm diameter) and thick (up to a 1 mm or more) pellet-type cells that are based on non-scalable manufacturing routes. Inevitably, these approaches lead to a low energy density at the cell scale. Practical applications require higher energy densities (typically 1000 W h L_{cell}^{-1}) and therefore thinner and larger area sheet-type cells made by scalable techniques. A scalable layer-by-layer spray printing approach has been explored for the manufacture of sheet-type SSB components, including the SE separator, cathode, and anode. Sprayed sulfide SE separators with a low thickness of 10 µm and high ionic conductivity of 1 mS cm $^{-1}$ were fabricated. A sprayed cathode was demonstrated and cycled for 800 cycles with a capacity retention of 63%. The high potential for process integration of the spraying approach was highlighted by the fabrication of a Li metal-free cell consisting of a sprayed Ag-C layer and a sprayed SE layer.

Declaration

All of the research presented was carried out by the author in the *Department of Materials* at the *University of Oxford* under the supervision of Prof P. S. Grant & Prof M. Pasta. The project was primarily funded by the UK Engineering and Physical Sciences Research Council (EPSRC) in alignment with the theme *Energy and Manufacturing the Future*, and conducted in close collaboration with the Faraday Institution programme of solid-state batteries (SOLBAT). The work is original and where work from others has been included it has been clearly referenced and acknowledged. No part of this thesis has been submitted or accepted for any other degree at this university or elsewhere.

Christopher Dörrer
Michaelmas 2022

Acknowledgements

First and foremost, thank you Patrick and Mauro for your supervision and the many invaluable discussions throughout my time in Oxford. It's been a pleasure to work together, to find and conceptualize solutions to make better batteries, and to implement many emerging ideas in the amazing lab spaces. Special thanks go to Peter and Harish for their assessment and helpful comments during my transfer and confirmation of status.

I want to thank Jitti for the training on working with sulfide solid electrolytes, as well as Jenny for the microscopy training, and Dimitrios for the support with the spray deposition system. Thank you Boyang for your collaborative spirit which led to the development of a better cell set-up. For their assistance with experiments, thanks is also given to Isaac (DLS), Sudarshan (XPS), Junliang and Chris (EBSD), Guillaume (Pt coating), Michael (spraying), and Junfu (P-FIB). Thank you Xiangwen, Sam W., and Dom S.J. for sharing your electrochemical knowledge on various occasions.

I would also like to thank my colleagues in Begbroke and the Rex Richards Building for their help, advice, and friendship during this work. Special thanks go to Yige, Jack, Lukas, Stan, Julia, Marveh, Enzo, Ann, Zeyang, Peng, Yeon Jeong, Zach, Brigita, Po-Yuan, Max S., Dom M., Gareth, Varnika, Stefanie, George, Shengda, John-Joseph, Max J., Rob, Stephen, and those who joined the weekly online SOLBAT meetings. I would like to thank Robin, Gideon, Greg, Andrew, Nadia, and Esther for realizing some of my designs and for securing smooth lab operations.

I am grateful to the EPSRC, the Faraday Institution, and the Henry Royce Institute for funding my research activities and providing essential equipment for this work.

My thanks and appreciations also go to Adrian, Marion, Paul, Leigh, Anja, and Sam P. for their help with administrative and organizational activities.

Finally, I would like to express my gratitude towards my family and all other friends who accompanied and supported me throughout this project outside the laboratories.

Publications

Parts of the work presented in this thesis have been published elsewhere. An index is provided here:

[1] **Doerrer, C.**, Capone, I., Narayanan, S., Liu, J., Grovenor, C. R. M., Pasta, M. & Grant, P. S. High Energy Density Single-Crystal NMC/Li_6PS_5Cl Cathodes for All-Solid-State Lithium-Metal Batteries. *ACS Appl. Mater. Interfaces* **13**, 37809–37815 (2021). https://doi.org/10.1021/acsami.1c07952

[2] **Doerrer, C.**, Gao, X., Bu, J., Wheeler, S., Pasta, M., Bruce, P. G. & Grant, P. S. Fast-charging all-solid-state battery cathodes with long cycle life. (submitted).

[3] **Doerrer, C.**, Metzler, M., Matthews, G., Jolly, D. S., Bu, J., Bruce, P. G., Pasta, M. & Grant, P. S. Spray-printing functional layers for sulfide-based all-solid-state batteries. (in preparation).

[4] Gao, X., Liu, B., Hu, B., Ning, Z., Jolly, D. S., Zhang, S., Perera, J., Bu, J., Liu, J., **Doerrer, C.** Darnbrough, E., Armstrong, D., Grant, P. S. & Bruce, P. G. Solid-state lithium battery cathodes operating at low pressures. *Joule* **6**, 636–646 (2022). https://doi.org/10.1016/j.joule.2022.02.008

[5] Zhou, Y., **Doerrer, C.**, Kasemchainan, J., Bruce, P. G., Pasta, M. & Hardwick, L. J. Observation of Interfacial Degradation of Li_6PS_5Cl against Lithium Metal and $LiCoO_2$ via In Situ Electrochemical Raman Microscopy. *Batteries & Supercaps* **3**, 1–7 (2020). https://doi.org/10.1002/batt.201900218

[6] Pasta, M., Armstrong, D., Brown, Z.L., Bu, J., Castell, M.R., Chen, P., Clocks, A., Corr, S.A., Cussen, E.J., Darnbrough, E., Deshpande, V., **Doerrer, C.**, Dyer, M.S., El-shinawi, H., Fleck, N., Irvine, J.T.S., Lee, H.J., Li, G., Liberti, E., Mcclelland, I., Monroe, C., Nellist, P.D., Shearing, P.R., Shoko, E., Song, W., Jolly, D.S., Thomas, C.I., Turrell, S.J., Vestli, M., Williams, C.K., Zhou, Y. & Bruce, P.G. 2020 roadmap on solid-state batteries. *Journal of Physics: Energy* **2**, 032008 (2020). https://doi.org/10.1088/2515-7655/ab95f4

[7] Liu, B., Gao, X., Pu, S., **Doerrer, C.**, Jolly, D. S., House, R., Melvin, D., Adamson, P., Grant, P. S. & Bruce, P. G. The effect of volume change and stack pressure on solid-state battery cathodes. (submitted).

[8] Jolly, D. S., Agarwal, V., **Doerrer, C.**, Hu, B., Zhang, S., Melvin, D.L.R., Gao, H., Gao, X., Adamson, P., Magdysyuk, O., Grant, P. S., House, R.A. & Bruce, P. G. Structural changes in the silver-carbon composite anode interlayer of solid-state batteries. (submitted).

Contents

Nomenclature xiii

1 Introduction **1**

2 Literature Review **7**

2.1 The bulk-type all-solid-state battery 7

2.1.1 Anode 8

2.1.2 Solid electrolyte 10

2.1.3 Composite cathode 14

2.2 Manufacturing challenges of all-solid-state batteries 16

2.3 Fabrication of particulate composites for SSBs 20

2.3.1 Wet-chemical methods 22

2.3.2 Dry powder mixing 34

2.3.3 Infiltration methods 37

2.4 Conclusions and new science 40

3 Experimental techniques **45**

3.1 Cell manufacturing 45

3.1.1 Material preparation 45

3.1.2 Dry composite SSB electrodes 46

3.1.3 Metal anodes 46

3.1.4 Layer-by-layer spray printing 47

3.1.5 SSB assembly 49

3.2 Physical characterization 53

3.2.1 Sample cross-sectioning 53

3.2.2 Scanning electron microscopy (SEM) 53

3.2.3 Energy-dispersive X-ray spectroscopy (EDX) 53

3.2.4 X-ray diffraction (XRD) 54

3.3 Electrochemical characterization 54

3.3.1 Galvanostatic cycling 54

3.3.2 Electrochemical impedance spectroscopy (EIS) . . . 57

4 High energy density single crystal NMC/LPSCl cathodes 61
4.1 Introduction . . . 61
4.2 Results and discussion . . . 63
4.2.1 Optimization of the cathode architecture . . . 63
4.2.2 Microstructure after initial cycle . . . 73
4.2.3 Impact of stack pressure during cycling. . . . 77
4.3 Conclusions . . . 84
4.4 Experimental details . . . 85

5 Fast-charging SSB cathodes with long cycle life 89
5.1 Introduction . . . 89
5.2 Results and discussion . . . 92
5.2.1 Fast-charging rate performance at 30 °C . . . 92
5.2.2 Fast-charging cycle performance at 30 °C . . . 98
5.2.3 Pore evolution in the composite cathode . . . 104
5.2.4 Increased cathode loading performance at 80 °C . . . 105
5.2.5 Specific energy and current density comparison . . . 107
5.3 Conclusions . . . 109
5.4 Experimental details . . . 110

6 Spray printing of thin layers for sulfide-based SSBs 113
6.1 Introduction . . . 113
6.2 Results and discussion . . . 115
6.2.1 Thin sulfide solid electrolyte separators. . . . 115
6.2.2 A spray-printed composite cathode . . . 122
6.2.3 A Ag-C layer for an anode-free cell design . . . 125
6.3 Conclusions . . . 131
6.4 Experimental details . . . 132

7 Conclusions 135
7.1 Summary . . . 135
7.2 Future work . . . 138

References 141

Nomenclature

a, c lattice constants
A area
C capacity
d diameter
E Young's modulus
f fraction
I current
i current density
l loading
$\dot{m}$ mass flow
N cycle number
$\dot{q}$ heat flow
R resistance
σ ionic conductivity
t thickness
θ angle
T temperature
U voltage
W_{grav} gravimetric energy density
W_{vol} volumetric energy density

AAM anode active material
BBP benzyl butyl phthalate
BC band contrast
BM ball milling
CAM cathode active material
CB carbon black
CE coulombic efficiency
C-El counter electrode
CNF carbon nanofibre
CNT carbon nanotube
CPE constant phase element
DIB dual-ion battery
DLS dynamic light scattering
EA ethyl acetate
EBSD electron backscatter diffraction
EDX energy-dispersive X-ray spectroscopy
EIS electrochemical impedance spectroscopy
FEM finite element method
GITT galvanostatic intermittent titration technique
GoF goodness of fit
ICE internal combustion engine
IPA isopropyl alcohol
IPF inverse pole figure
LCO Li-Co oxide
LFP Li-Fe phosphate
LGPS $Li_{10}GeP_2S_{12}$
LIB lithium-ion battery
LiPON lithium phosphorus oxynitride
LLZO $Li_7La_3Zr_2O_{12}$
LP large particle
LPS Li_3PS_4
LPSCl Li_6PS_5Cl
LSB Li-S battery
LTO $Li_4Ti_5O_{12}$

LTS $LiTiS_2$
MSB Mg-S battery
NA not available
NBR nitrile butadiene rubber
NCA Li-Ni-Co-Al oxide
NMC, NCM Li-Ni-Mn-Co oxide
NMP N-Methyl-2-pyrrolidone
NWS non-woven scaffold
PC polycrystal
PEEK polyether ether ketone
P-FIB plasma focused ion beam
PMMA poly(methyl methacrylat)
PPC polypropylene carbonate
PPTA poly(paraphenylene terephthalamide)
PTFE polytetrafluoroethylene
PVB polyvinyl butyral
PVC polyvinyl chloride
PVDF polyvinylidene fluoride
PVP polyvinylpyrrolidone
QSS quasi-solid-state
R-El reference electrode
RT room temperature
SC single crystal
SE, SSE solid electrolyte
SEBS styrene-ethylene-butylene-styrene
SEM scanning electron microscopy
SOC state of charge
SP small particle
SSB, ASSB solid-state battery
SUS stainless steel
TEM transmission electron microscopy
THF tetrahydrofuran
VGCF vapour grown carbon fibre
W-El working electrode
WIP warm isostatic pressing
WS-El working sense electrode
XPS x-ray photoemission spectroscopy
XRD x-ray diffraction

Introduction

Due to a higher awareness of the limited availability of fossil fuels and the desire for a more sustainable use of resources among modern society, leading industrial nations have started to initiate significant changes to their energy policies. A major goal pertaining to the generation of electrical energy is to move from fossil to renewable energy sources such as wind and solar and thus to reduce associated environmental and climate impact. Furthermore, in the transport sector local emissions are particularly problematic in big cities and have to be cut to support reduction of global carbon dioxide concentration to pre-millennial levels. As a consequence, several nations including the United Kingdom and the European Union have agreed on a ban of newly registered cars powered by an internal combustion engine (ICE) after 2035 [1].

The replacement of the ICE in the transport sector poses a great technical challenge because fossil fuels can be simply stored and refilled, and 1 litre of gasoline has a high energy of ∼10 kW h [2]. Most concepts to replace the ICE are based on an electric motor that is powered by a battery or a combination of a fuel cell and a hydrogen tank, both of which do not emit any greenhouse gas, but have a lower energy density than the ICE [3]. Therefore EVs often have a much shorter range capability compared with ICE-powered cars and there is a worldwide demand for electrochemical energy generation and/or storage with higher energy density [4].

Lithium-ion batteries (LIBs) have been extensively used for energy storage since they were first commercialized by Sony in 1991 [5]. LIBs are based on the

Table 1.1: Growing demand of energy storage with high level of safety and high energy density. Reproduced from [8–12].

Portable devices	Electric vehicles	Electric aircraft
		
10 W h 1 charge/day $>10^{12}$/year	10^5 W h 1 charge/500 km 7×10^6/year	3.2×10^5 W h 1 charge/250 km Individual prototypes

development of a cathode material discovered by Goodenough in Oxford in 1980 [6], and have been steadily improved in the intervening decades, which has enabled applications such as smartphones or tablets, produced in the billions per year. EVs have been possible through the connection of several thousand individual Li-ion cells that provide a high energy of 10^5 W h. Sales figures for EVs are steadily increasing globally and reached ~7 million in 2021 [7]. LIBs have also caused optimism to develop futuristic means of transportation such as electrically powered aeroplanes. Applications that require a high energy density storage are summarized in Table 1.1.

As a result of intensive development, conventional LIBs consisting of a transition metal oxide as the cathode and graphite as the anode have nearly reached their feasible limits in terms of maximum energy densities (e.g. ~264 W h kg^{-1} for a Li-Ni-Co-Al oxide (NCA)/graphite 18650-type cell) as shown in Fig. 1.1 [13, 14]. Further improvements can only be achieved incrementally and at increased cost, by a parameter adaption so more significant changes are required.

New cell chemistries have been developed, mostly at laboratory scale, that outperform LIBs in certain aspects [15–17]. How the theoretical gravimetric and

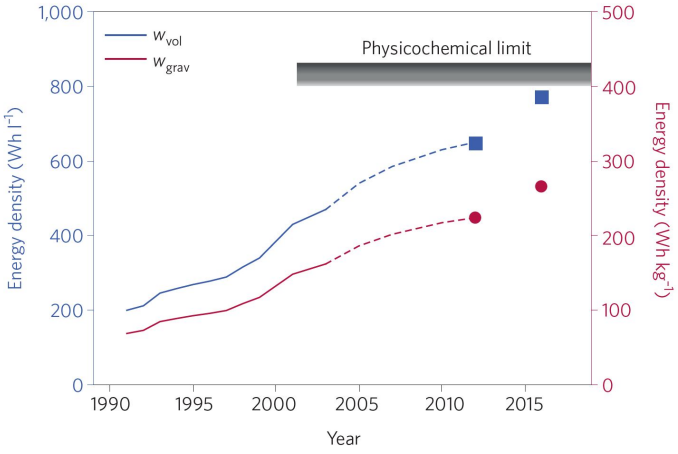


Fig. 1.1: Development of the gravimetric and volumetric energy density of the LIB from first introduction towards the physicochemical limit. Reproduced from [13].

volumetric energy density is translated to practical values in various applications has been investigated by Betz et al. [14]. Fig. 1.2 compares the volumetric and gravimetric energy density for different cell chemistries from theory (indexed with 1) towards progressively more technologically relevant formats (indexed

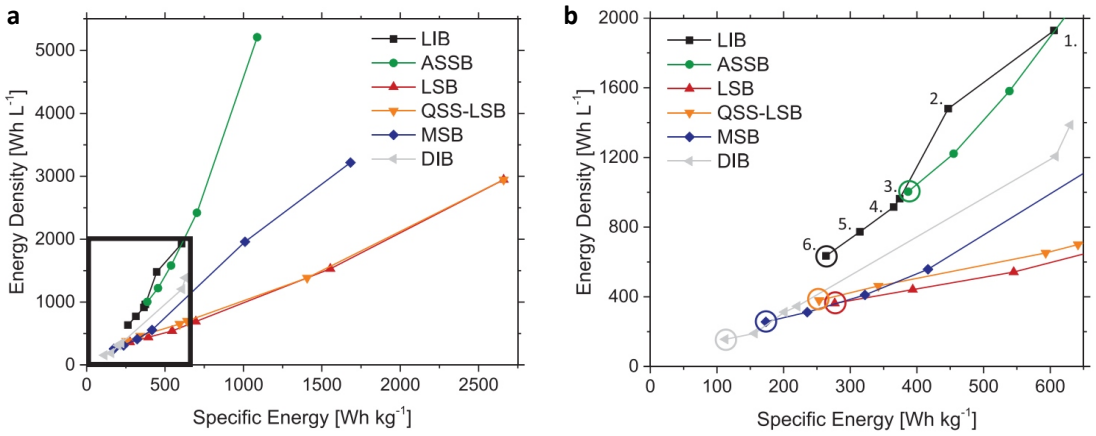


Fig. 1.2: (a) Energy density versus specific energy for six battery technologies from theoretical values (step 1) to cell level (step 6). (b) A magnified inset. Lithium/sulfur battery (LSB), quasi-solid-state lithium/sulfur battery (QSS-LSB), magnesium/sulfur battery (MSB), dual-ion battery (DIB). Reproduced from [14].

with 6). The study reveals (i) theoretical performance is reduced by at least a factor of 3 in real applications and (ii) only all-solid-state batteries (SSBs) have the potential to outperform LIBs in terms of both energy per unit mass and per unit volume.

Beside their promising energy density, another crucial advantage of SSBs is their potential for a higher level of safety [18, 19]. Unlike conventional LIBs, SSBs do not require a flammable organic solvent that improves their intrinsic fire resistance, and also may allow operation at higher temperature. While elevated temperatures for LIBs may result in a thermal runaway, SSBs can show improved performance under this condition because of increased ion mobility. Kato et al. [20] investigated high-power SSBs at 100 °C, which were charged/discharged for hundreds of cycles in an exceptionally short time of only 3 min. Despite encouraging results, many challenges remain in the design, fabrication and materials selection for SSBs before they can become broadly available in the commercial market [21].

The thesis investigates and develops processing routes that provide a more flexible platform to explore experimentally and understand the influence of different electrode architectures on SSB performance, for example, energy and power density, charge/discharge time and cyclability. The following objectives are pursued: (i) to design and develop a versatile test set-up that allows for cycling SSBs at a variable stack pressure that provides simple cell exchange to then investigate the processability and cycling performance of various different cathode composites, (ii) to investigate whether best-performing cathodes can be used for fast charging at room temperature and how this affects capacity fading, and (iii) to explore a new layer-by-layer spray process in an inert atmosphere applied to moisture sensitive solid electrolyte materials and to investigate how this process might improve solid-state cell fabrication.

Chapter 2 describes the main components of a SSB and reviews different manufacturing strategies with examples from the literature. Chapter 3 explains the experimental techniques used in subsequent chapters 4–6. Chapter 4 demonstrates that single crystal Li-Ni-Mn-Co oxide (NMC) based cathodes can provide excellent discharge capacity and are less prone to particle cracking during processing and cycling compared with polycrystalline materials. Chapter 5 employs a three-electrode design to examine the cathode rate performance and analyses the evolution of pore formation in the composite cathode microstructure at high charging rates over 1000 cycles. Chapter 6 explores how the use of different solvents affects the ionic conductivity and microstructure of sprayed sulfide solid electrolytes and showcases the benefits of the layer-by-layer spray process for sulfide-based SSBs components, such as the electrolyte separator, cathode, and anode. Lastly, chapter 7 summarizes the work and suggests future prospects for the field with potential applications.

Literature Review

2.1 The bulk-type all-solid-state battery

The two main advantages of a SSB over a LIB are a higher level of safety and a higher energy stored per unit mass or volume. A SSB schematic design that may be suitable for high energy density storage is shown in Fig. 2.1 [13]. The key difference to achieve a higher energy density compared with a LIB is the use of a Li metal anode instead of a graphite anode. The capacity of Li (3700 mA h g^{-1}) is about ten times higher than that of graphite (372 mA h g^{-1}) which leads to an estimated increase in cell energy density of 40–70% as shown in Fig. 2.1 [13].

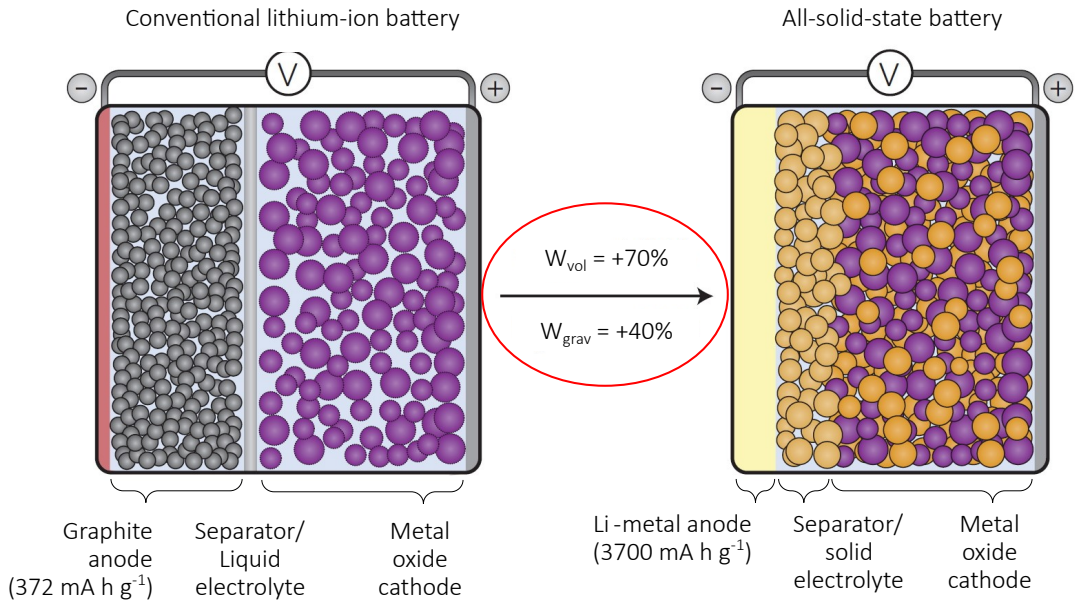


Fig. 2.1: Schematic diagram of a LIB and a bulk-type SSB with the predicted increase of the volumetric W_{vol} and gravimetric energy density W_{grav}. Reproduced from [13].

A higher level of safety is provided by the use of an intrinsically non-flammable inorganic solid electrolyte (SE) that replaces the mixture of Li-ion-containing organic solvents used in a LIB. There is a SE layer between the electrodes that acts both as a physical separator and a Li-ion conductor. Similar to a LIB that contains a liquid electrolyte, bulk-type SSBs also use a composite cathode, but generally without pores. Instead, SE material is distributed within dense electrodes to enable Li-ions to reach the cathode active material (CAM) through solid-state ion conductive pathways. A three-dimensional percolating network of SE and CAM in the electrode must maintain sufficient contact at the solid/solid interfaces during cycling to compete with the long-term cyclability of LIBs. This review focuses on the design and manufacturing approaches for bulk-type batteries using sulfide SE, which is one of the most promising families of solid-state electrolyte materials due to its high intrinsic ionic conductivity.

2.1.1 Anode

The principle difference of a SSB Li anode compared to a conventional LIB is the absence of a host or intercalation material such as graphite for Li-ions. This results in a much higher volume change in the anode that can theoretically be infinite if the entire Li is electrochemically plated and stripped during charge and discharge. Practically, most SSBs use excess Li which is provided in form of a thin (10–50 µm) Li foil attached to the planar SE separator before cycling. In this case, the overall volume change in the anode is reduced and depends on the original thickness of the Li foil and the amount of Li that is plated/stripped during one cycle.

Nonetheless, stripping can still cause a substantial local volume change if the Li from adjacent regions cannot accommodate any voids from stripping e.g. by diffusion or creep. This can lead to void formation at the Li/SE interface and cause further damage such as acting as a nucleation site for the growth of a Li dendrite

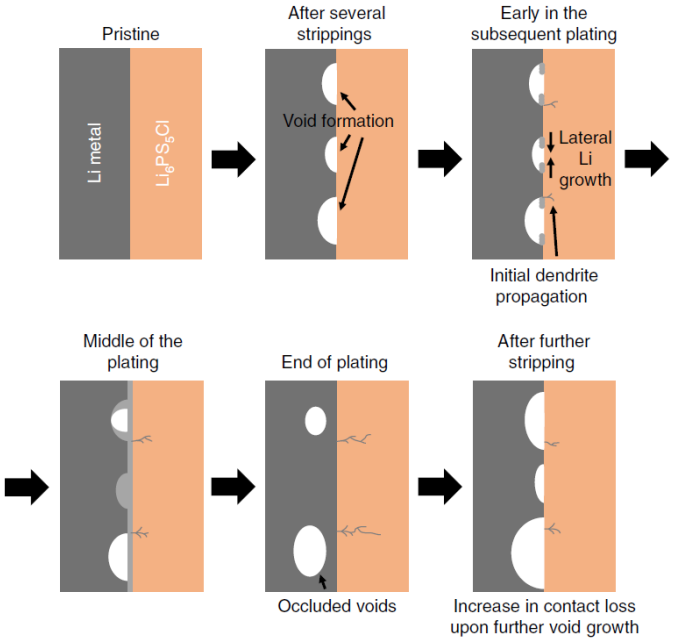


Fig. 2.2: Schematic of the void formation during Li stripping that leads to a higher local current density upon plating and the initiation of dendrite formation. Reproduced from [22].

that can cause an internal cell short circuit. The effect is shown schematically in Fig. 2.2 [22]. To increase the Li mobility in the anode and to maintain intimate contact at the Li/SE interface a stack pressure of several MPa (or considerably more) is often applied. A higher temperature or stack pressure can increase the so-called critical current density before cell failure occurs but there is so far no breakthrough solution to suppress Li dendrites with Li metal anodes, and internal Li penetration remains a major challenge for SSBs [23].

Due to the relatively low critical current density (<1 mA cm^{-2} at RT and ~2 MPa) of Li metal with most SEs, other options such as Li alloy materials have also been explored [24]. Many Li alloys (e.g. Li-In) have enabled a higher critical current density (>3 mA cm^{-2}) but are often non-practical because of their much lower energy density [25]. Besides, Li alloys usually also have a large volume change and can be significantly harder than Li and so require substantial stack pressures to

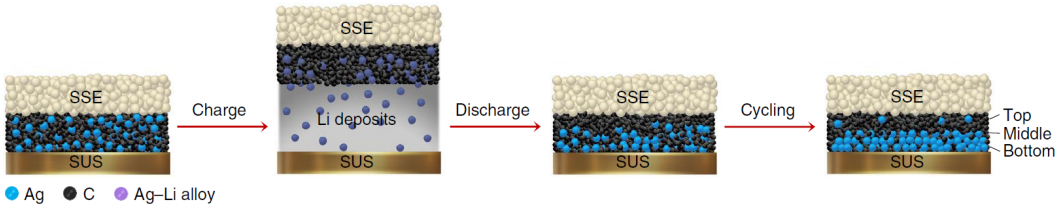


Fig. 2.3: Schematic of an anode-free SSB enabled by a particulate Ag-C layer. Reproduced from [26]. Solid-state electrolyte (SSE), stainless steel (SUS).

maintain intimate anode/SE contact. Amongst the most frequently used materials that form an alloy with Li are In, Si, and Ag.

A thin (5-10 µm) particulate Ag-C layer shown in Fig. 2.3 has been investigated in a so-called anode-free SSB in which Li was entirely provided from the CAM and plated on a stainless steel current collector during charging to form the anode [26]. The Ag-C layer enabled a more uniform growth of Li compared to plating directly on stainless steel presumably by the nucleation of metallic Li on the high surface area Ag-C particulates. The Ag nanoparticles in the Ag-C layer became alloyed with Li in the early stages of charging, with the C also absorbing some Li before metallic Li formed on the current collector [26]. Anode-free concepts are still in an early research stage and a better understanding of the underlying mechanism of Li plating when nano-particulate layers are used is necessary to reach practical critical current densities of >5 mA cm^{-2}.

2.1.2 Solid electrolyte

One of the most important characteristics of the SE is its ionic conductivity. It is generally assumed that SE materials require an ionic conductivity of at least 10^{-4} S cm^{-1} over the temperature range of their operation to allow realistic charge/discharge times [27, 28]. For comparison, organic liquid electrolytes have ionic conductivities $>10^{-2}$ S cm^{-1} [29]. Other critical specifications include low electrical conductivity ($<10^{-10}$ S cm^{-1}), large electrochemical window (ideally

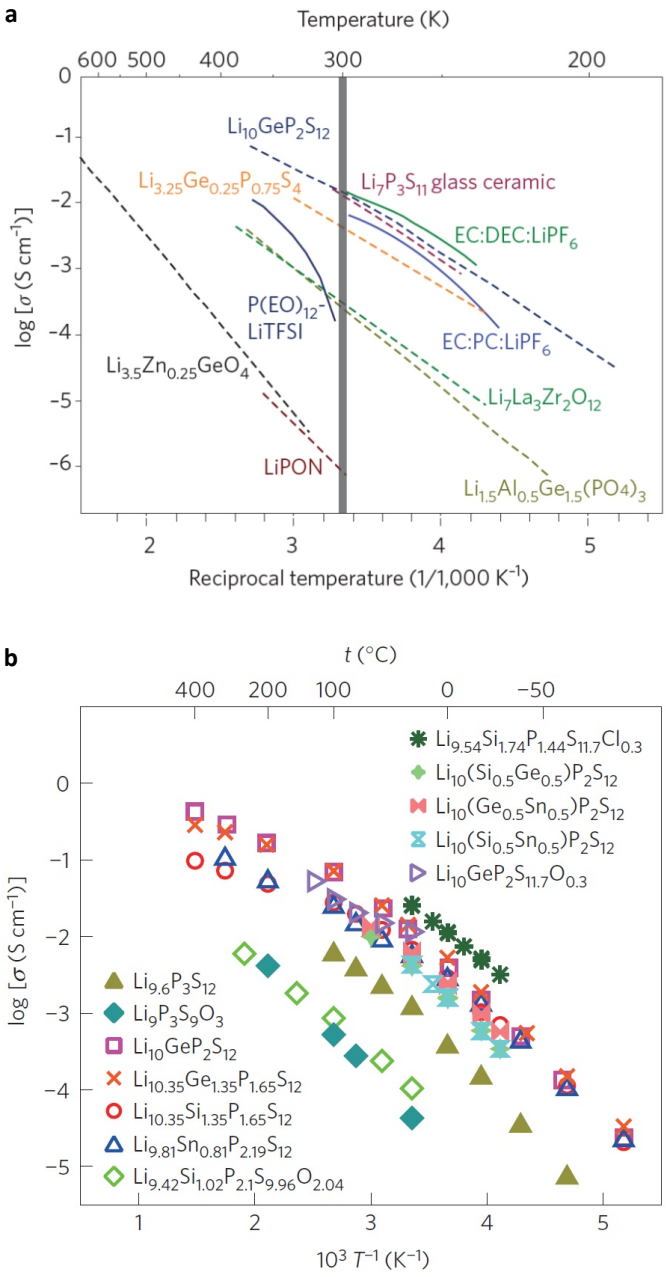


Fig. 2.4: (a) Ionic conductivities of SEs in comparison to those of liquid electrolytes and polymers. Reproduced from [13]. (b) Arrhenius conductivity plots for the LGPS family, $Li_{9.6}P_3S_{12}$, and $Li_{9.54}Si_{1.74}P_{1.44}S_{11.7}Cl_{0.3}$. Reproduced from [20].

<0 V to >5 V for high-voltage type Li metal batteries), and good chemical stability with other electrode materials [27].

SEs are often broadly classified into two groups of polymer-based and inorganic materials while the latter can be further subdivided into two principal groups of oxides and sulfides [28]. The ionic conductivity of various SEs is shown in Fig. 2.4 [13, 20]. Even though polymer-based SEs are advantageous because of their formability and rather simple synthesis they suffer from a narrow temperature window and poor chemical and mechanical stability at the SE/electrode interface [28]. Among inorganic SEs, sulfide materials have the highest ionic conductivity of up to 25 $\times$ 10^{-2} S cm^{-1}, which may even exceed that for some organic liquid electrolytes [20]. Moreover, sulfides may allow for simpler processing (at least compared with oxides) due to their relatively low flow stress which is an advantage if cell manufacturing requires pressing or other consolidation steps [29]. Oxide SEs generally tend to have lower ionic conductivities than sulfides, reaching approximately 1 $\times$ 10^{-3} S cm^{-1}, but have better electrochemical stability.

Two promising and most widely studied inorganic materials are Li_6PS_5Cl (LPSCl) and $Li_7La_3Zr_2O_{12}$ (LLZO). LPSCl was first reported by Deiseroth et al. in 2008 and belongs to a group of argyrodites with the general formula Li_6PS_5X (X = Cl, Br, I) [30]. The ionic conductivity depends on the synthesis method but usually lies in the range 1–5 $\times$ 10^{-3} S cm^{-1} at room temperature (RT) [31–35], with a low electronic conductivity of less than 2 $\times$ 10^{-9} S cm^{-1} [36, 37].

The intrinsic electrochemical stability of LPSCl was investigated by first principle calculations at 2 to 2.4 V [38]. In contrast, frequently reported cyclic voltammetry measurements of semi-blocking cells imply a much wider stability window in practice, with an interval possibly as wide as 0 to 5 V. It is believed that a passivation layer consisting of Li_2S, Li_3P and LiCl is formed at the electrode/electrolyte interface that prevents further decomposition, and widens the practical voltage window of use [37–40]. Han et al. argued that the wide electrochemical windows from measurements in semi-blocking cells may not be transferable to bulk-type

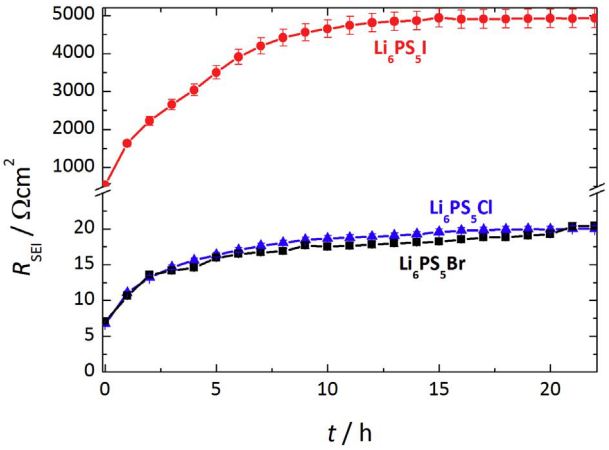


Fig. 2.5: Interfacial resistance increase over time of different sulfide SEs in contact with Li metal determined by electrochemical impedance spectroscopy (EIS). Reproduced from [40].

batteries because of the slower oxidation and reduction kinetics as a result of the relatively small contact area between electrolyte and electrode in a semi-blocking cell. They proposed that a small stability window may be one of the reasons for the disappointing performance of bulk-type batteries [41]. Nonetheless, LPSCl is one of the more stable sulfide SEs with Li as shown in Fig. 2.5, which compares the interfacial resistance changes over operation time. The levelling out of resistance suggested a slow-down of undesired interfacial reactions and reasonably good practical usability.

LLZO is a garnet-type oxide electrolyte with an ionic conductivity between 0.1 and 1 mS cm^{-1} at RT [42]. To stabilize the more conductive cubic phase rather than the tetragonal, LLZO is often doped with other elements such as Al or Ta [43, 44]. The electronic conductivity of either pure or doped LLZO is of the order of 10^{-9} S cm^{-1}, and considered negligibly small [45].

The electrochemical stability window for LLZO is 0.05 to 2.91 V according to first principle calculations [39, 41]. This is, however, significantly narrower than measurements by cyclic voltammetry that have suggested a stability window as large as 0 to 6 V [46]. The improved stability in practice again arises due to

formation of a passivation layer as a result of electrolyte decomposition into Li_2O, La_2O_3 and other oxides in the very early stages of cycling [41]. It is also open to debate on what constitutes "stable" as practically all materials might be judged to be "unstable" during cycling to some extent [47].

2.1.3 Composite cathode

The design of a composite cathode involves trade-offs in the complex interplay of SE particles, CAM particles, and other possible additives such as a polymer binder and an electron conductive aid. A typical CAM for a SSB is a transition metal such as used in a LIB e.g. $LiCoO_2$ (LCO) or a Ni-rich oxide of the $LiNi_xMn_yCo_zO_2$ (NMC, sometimes NCM) family with a more refined focus on low volume change materials. The particle size and distribution of each constituent in the composite cathode microstructure is of particular importance when it comes to high current density operation where high resistances between solid particle contacts cause a high overpotential. The typical effect of the particle size of both the CAM and the SE is shown in Fig. 2.6 and Fig. 2.7, respectively [48, 49].

A composite cathode with small (S) CAM particles (d_{50} = 4 µm) achieved a discharge capacity that was 65 mA h g^{-1} higher compared with a cathode with

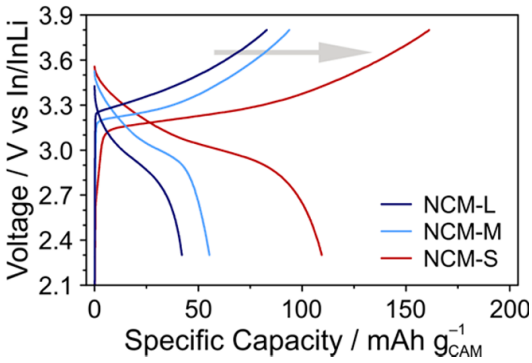


Fig. 2.6: Effect of the CAM particle size on the capacity in a composite cathode. Reproduced from [48]. Large (L, d_{50} = 15.6 µm), medium (M, d_{50} = 8.3 µm), small (S, d_{50} = 4 µm).

large (L) CAM particles (d_{50} = 15.6 µm). The study was conducted on composites comprising only SE and CAM particles, and the increase in capacity was ascribed to improved electronic conductivity in the cathode. To increase the electron percolation in the cathode an electron conductive aid is often added, mostly in the form of carbon black (CB) or carbon nanofibers (CNFs).

The particle size of the SE also strongly influenced the capacity in a composite cathode as shown in Fig. 2.7 [49]. Whereas a decrease from 8 µm to 3 µm resulted in a substantial capacity increase of 75 mA h g^{-1} an even smaller size of 1.5 µm did not lead to any significant changes. A computational study confirmed that a larger ratio of CAM to SE particle size enabled a higher cathode loading. This might be expected as smaller SE particles can cover more CAM surface and therefore serve a function somewhat alike to the wettability of a liquid electrolyte in a LIB.

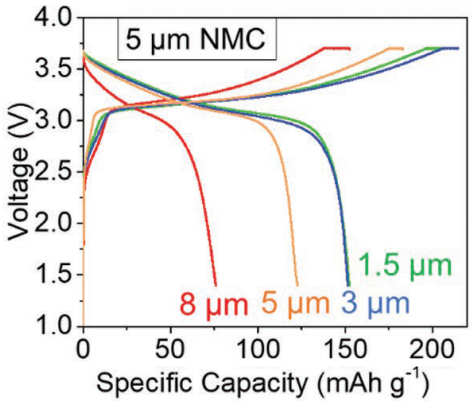


Fig. 2.7: Effect of the SE particle size on the capacity in a composite cathode. Reproduced from [49].

A microstructural model of a composite cathode suggested that the SE will need an ionic conductivity of at least 10^{-3} S cm^{-1} to use a similar volume fraction of electrolyte as in a LIB electrode (e.g. 30%) and to operate at a current density beyond 1 mA cm^{-2} [50]. Processing-rooted requirements such as the incorporation of binder and the persistence of pores can strongly hinder Li-ion transportation

and realization of the CAM capacity and should be decreased as much as possible from an electrochemical point of view.

Due to the different constituents present in the composite, there are usually many potential side reactions during cycling, which are mitigated in practice by solid oxide coatings on the CAM that allow for improved capacity and cycle life. $LiNbO_3$ and $Li_3BO_3{-}Li_2CO_3$ coatings, for example, have been shown to slow down capacity fading [51, 52].

2.2 Manufacturing challenges of all-solid-state batteries

Aside from the generic problem of Li dendrite formation during stripping/plating at the anode during charge/discharge cycling, which can lead to internal short circuits that is common to all Li metal-based SSBs, there are other significant challenges. Informative reviews discussing general [42, 53, 54] and also more specific [47, 55, 56] issues of sulfide and oxide SSBs have been published in the last few years. However, this section summarizes the most significant difficulties of bulk-type SSBs from a manufacturing point of view, and relates to the principal experimental work of this thesis.

As shown in Fig. 2.1, bulk-type SSBs have a particularly large contact area between the electrolyte, conductive additives, and active materials. This means that, unlike thin film SSBs, bulk-type batteries cannot be made by simply stacking thin, (e.g. a few micrometers) planar layers of dense active material and dense electrolyte. Instead, percolating, conductive ionic, and electronic pathways need to be formed at all points within a composite electrode, ideally to connect each active particulate to both percolating ionic and electronic pathways, to facilitate ion transport back and forth across the SE separator and electron transport to and from the current collector [54]. Moreover, it is of importance that the materials that form these electronic and ionic networks are incorporated with as little mass and volume

as possible because they themselves are electrochemically inactive (sometimes called "parasitic") materials that will lower the gravimetric and volumetric energy density of the resulting battery. Thus, manufacturing methods that enable a high mass fraction of the CAM while preserving efficient percolating ionic (electrolyte) and electronic (carbon) pathways are required.

In order to maintain a low resistance at the many solid/solid interfaces within a SSB, it is crucial that the particles in the electrode remain in contact, even during cycling during which there may be volume changes in the active material. The fabrication of low resistive contacts is especially challenging if both the active material and the SE consist of "hard" materials e.g. oxides. In this case, simple mechanical pressing will likely not be effective, with only point contacts rather than a conformal interface of maximum contact area between the particulate active material and the SE [57]. The need for maximal inter-particle contact also applies to the dense SE separator layer of a bulk-type SSB design.

Cold-pressing alone of oxide SE particles leads to relatively high residual porosity and inter-particle/grain boundary resistance, which then lowers the overall ionic conductivity [58]. A dense (e.g. >90% for LLZO [58]) and thin (<30 µm for high energy cells [59]) SE layer between the electrodes is optimal, although thinner separators are more vulnerable to Li dendrite short circuits, and manufacturing defects. In order to produce dense SE oxide layers >90%, sintering at elevated temperatures above 1000 °C is normally required [58, 60, 61]. Such temperatures are suitable, although energy-intensive, to produce phase pure and dense electrolyte pellets. However, the presence of other less thermally stable materials e.g. fine-scale carbon for electron percolation can lead to inter-diffusion, side reactions with the electrolyte or active material, or even complete volatilization [62]. Thus, a high-temperature sintering approach for the fabrication of composite cathodes remains problematical [63, 64].

Whereas a high density may be favoured for the SE separator for Li-ion mobility, an entirely pore-free composite electrode may have relatively high modulus and low compliance to mechanical load. One source of mechanical load may be the volume change of the active material during lithiation and delithiation. The relative volume changes of cathode (LCO: ∼2 vol%, NMC (811): ∼6 vol%, LFP: ∼7 vol%) and anode ($Li_4Ti_5O_{12}$, LTO: ∼0.2 vol%, graphite: ∼13 vol%, Si: ∼400 vol%) materials can lead to stress and strain in the electrode, especially in low compliance arrangements, and contact losses between the CAM and the SE [65, 66]. Consequently, Li-ion mobility to/from the active material is restricted and capacity fades. An external pressure (for example 10 MPa) or "clamping" force during cycling is generally applied to maintain the solid/solid contact over many cycles – an effective but inelegant engineering solution.

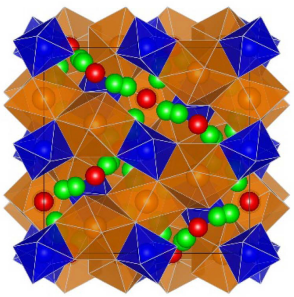
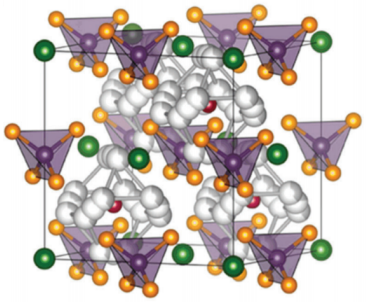
Additionally, mechanically compliant "buffer" layers, for example, materials of low modulus, coated around the active material, can be used to compensate for volume changes (in effect to increase compliance). Due to their low Young's modulus (18–25 GPa), sulfide SEs may be well-suited as a compliant buffer layer [57, 67, 68]. This aids simplicity as no additional, discrete coating layers are required. As previously mentioned, sulfide formability may also be helpful for enduring particle-particle contacts simply by sulfide powder pressing (and powder flow and deformation) at RT. These aspects suggest promise for sulfide-based SSBs, but must be balanced by some significant disadvantages.

The principal disadvantage of sulfides, particularly with respect to their integration into manufacturing processes, is their instability in the presence of water vapour [69, 70]. The by-product of sulfide water vapour reactions is hydrogen sulfide (H_2S) which is extremely toxic. As a result, the entire process chain of sulfide SSBs from material synthesis to a final packaging step must be performed in a dry room or under an inert atmosphere [71]. In general, the ionic conductivity of sulfides

and oxides such as LLZO is better preserved when sintering was performed in Ar instead of moist air [72]. Providing an inert gas atmosphere leads to significantly increased machine and production costs.

On the anode side, the production of a Li metal foil, ideally with thickness as low as 10–20 µm, is non-trivial due to high reactivity with oxygen and nitrogen that significantly increases manufacturing challenge and complexity. As previously described, an anode-free architecture using a thin particulate interlayer e.g. Ag-C, that could be fabricated by a printing or spraying process, would be more highly favourable as it would enable cell assembly without the involvement of large areas of thin, highly reactive Li metal.

Table 2.1: Comparison between oxide and sulfide SEs. Reproduced from [73, 74]. Positive, neutral, and negative qualities are highlighted in green, yellow, and red, respectively. Ionic conductivity (σ), temperature (T), Young's modulus (E).

Solid electrolyte	Garnet $Li_7La_3Zr_2O_{12}$	Argyrodite Li_6PS_5Cl
Oxides vs. Sulfides		
	a = 12.985 Å	a = 9.986 Å
σ (S cm^{-1})	$>10^4$	$>10^3$
Stability vs. Li	High	Unstable
Stability in moist air	Moisture-sensitive	Hydrolysis
Processing T	High	Low
E (GPa)	150	20

The advantages and disadvantages of sulfide and oxide SEs discussed herein are summarized exemplary for most common materials, namely LLZO and LPSCl in Table 2.1.

2.3 Fabrication of particulate composites for SSBs

A schematic overview of deposition methods that may find application in the manufacturing of LIB electrodes is shown in Fig. 2.8 [75]. For conventional LIBs with a liquid electrolyte, the electrode is porous (typically 30 vol%) and the prevailing industrial technology is slurry casting, which has variants known as slot casting or slot die coating [76]. A variant using a "doctor blade" method is often used in laboratories because of its simplicity but achieves a less uniform electrode thickness and porosity distribution [77]. All approaches use a slurry that contains the active material (∼90 wt%), conductivity enhancer (∼5 wt%), and a binder (∼5 wt%) dispersed with a fugitive carrier such as NMP, acetone or other organic solvents [78, 79]. When the coated electrode is dried through a sequence of steps, the electrode is ∼100 µm thick with a tortuous interconnected porosity of 25–35 vol%. The active particulate diameter is usually 5 to 15 µm [48]. Alternative processes such as spray coating [80–82], different printing approaches [83, 84]

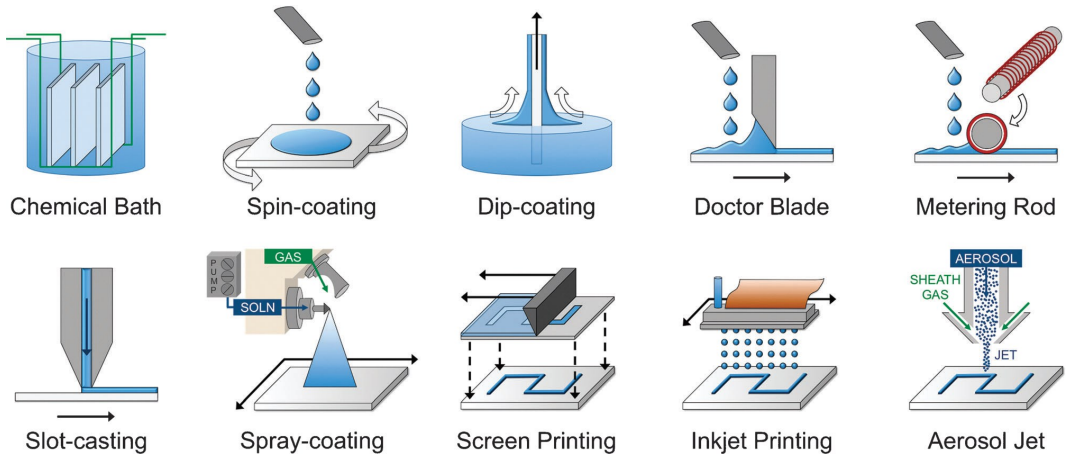


Fig. 2.8: Depiction of various solution deposition methods. Reproduced from [75].

and aerosol jet [85–87] have also been explored to enable greater design freedom over the microstructure e.g. the spatial distribution of conductivity enhancer and binder [88].

Some of the methods in Fig. 2.8 have been considered for SSBs. One major difference is that the porosity that is required in LIBs must be replaced by a SE, with almost no residual porosity i.e. SSBs must have both a solid electronic percolating network and a solid ionic percolating network. Sakuda et al. suggested a simple classification of SSBs according to Fig. 2.9 [89] whereby bulk-type batteries can be grouped in pelletized cells that are mostly pressed in a plastic mould between two metal rods, and free-standing sheet-type batteries suitable for pouch cells and industrial application.

Thin film batteries such as those that are based on lithium phosphorus oxynitride (LiPON) are not considered in detail here as the research focus is on bulk-type SSBs. Nonetheless, it is worth mentioning that they are fabricated mostly by physical/chemical vapour deposition techniques (e.g. radio frequency magnetron sputtering in a N_2 atmosphere) [90]. The resulting thin film batteries are used to power, for example, microelectromechanical systems or implantable medical

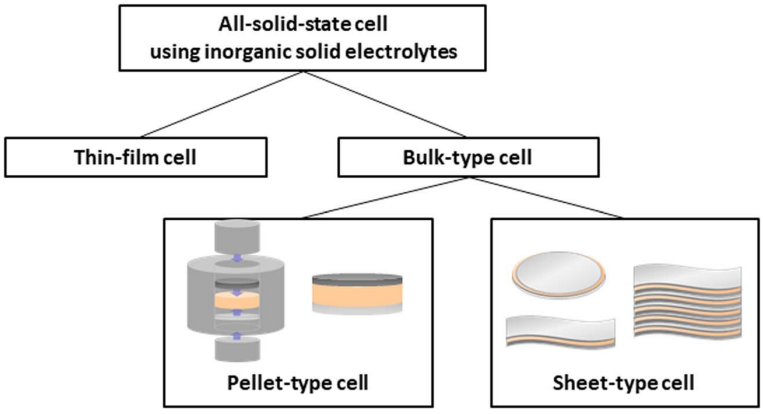


Fig. 2.9: Classification of all-solid-state batteries using inorganic SEs. Reproduced from [89].

devices, but they are not suitable for applications where high energy capacity storage is required [91].

Powder-pressed, pellet-type SSBs exhibit a lower energy density than sheet-type solid-state pouch cells because of the relatively thick (300–1500 µm) SE layer provided by the pellet, and are mostly used in laboratories to study fundamental properties such as wetting, ionic conductivity, interfacial reactions etc. Possible process chains for more industrially relevant sheet-type SSBs (e.g. for pouch cells) have been discussed by Schnell et al. [21]. The following sections describe in detail the most promising strategies for the fabrication of both pellet and sheet-type SSBs containing sulfide and oxide SEs, focusing on composite cathodes.

2.3.1 Wet-chemical methods

As previously described, production of LIB electrodes starts with the preparation of a slurry where active material, additives, and binder are mixed in a liquid solvent suspension. While the binder is normally dissolved in the solvent, conductive additives and the active material remain as particulate and form a suspended dispersion. This approach may be adapted for electrodes used in SSBs with the addition of a dispersed or dissolved electrolyte into the conventional slurry, increasing its complexity. The intention is that as the fugitive carrier evaporates, the electrolyte either precipitates onto the active fraction or the electrolyte particles are intimately mixed with active material. SE only particles can also be used to cast the SE separator, but the resulting porosity makes the separator (or composite cathode) useless unless it can be substantially densified.

Dissolution methods

Unlike oxide electrolytes, sulfides may be dissolved and subsequently reprecipitated during solvent evaporation. This method offers the possibility of coating a SE layer around active particulate, assuming good wetting can be contrived. Then,

the coated particles can be cold pressed (recognizing the low flow stress of sulfides) to form an ionically conductive matrix with incorporated active material. For a composite cathode, electrical conductivity enhancer (e.g. carbon) must also be incorporated. Polar solvents, for example ethanol, can be used to dissolve selected sulfide SEs [92]. Sulfide ionic conductivity after reprecipitation depends on the drying temperature (and the resulting crystallinity), for example, unless temperatures >200 °C were used, the ionic conductivity of LPSCl was significantly lower (1–2 orders of magnitude) than before dissolution/reprecipitation [93].

Yubuchi et al. investigated the performance of composite cathodes made of particulate LCO with an LPSCl coating [94]. They dissolved ball-milled (BM) LPSCl in anhydrous ethanol and added $LiNbO_3$-coated LCO to form a suspension that was first stirred and subsequently dried at 80 °C under vacuum. The resulting LPSCl-coated particles were pressed with a sulfide SE and a Li-In foil then attached to act as an anode. The measured cell capacity was <50 mA h g^{-1} ($\sim \frac{1}{3}$ of theory), which may be explained by a low ionic conductivity of the reprecipitated LPSCl (1.4×10^{-5} S cm^{-1}) and the low electronic conductivity due to the absence of conductivity enhancer.

In a newer report, Yubuchi et al. [93] then increased the capacity by optimization of the drying temperature, as shown in Fig. 2.10a. In/Li_3PS_4/LCO cells dried at 150 °C showed the best capacity, and also outperformed a cathode prepared by dry blending of the same CAM and sulfide powder. The better performance fabricated by dissolution/reprecipitation can be explained by examination of the micrographs shown in Fig. 2.10b. Whereas there were many pores and some direct contact of CAM for the dry-blended mixture, the coating method provided a denser structure where sulfide pathways were distributed contiguously around the particles.

Rosero-Navaro et al. improved the electrochemical performance further by increasing both the electronic and ionic conductivity [95]. They first dissolved BM-LPSCl in an ethanol and acetonitrile mixture. A small amount of vapour-grown carbon fibres (VGCFs) was added to enhance electronic conductivity, together with a dispersant (Triton X100). $LiNbO_3$-coated NMC particles were dispersed in the different mixtures and heated up to 180 °C. Powders were then pressed into a pellet with a sulfide SE and Li-In as an anode. A small amount of dispersant in the liquid mixture improved the ionic conductivity of LPSCl to 0.6×10^{-3} S cm^{-1} due to a reduction in agglomeration and a more uniform dispersion and gave a

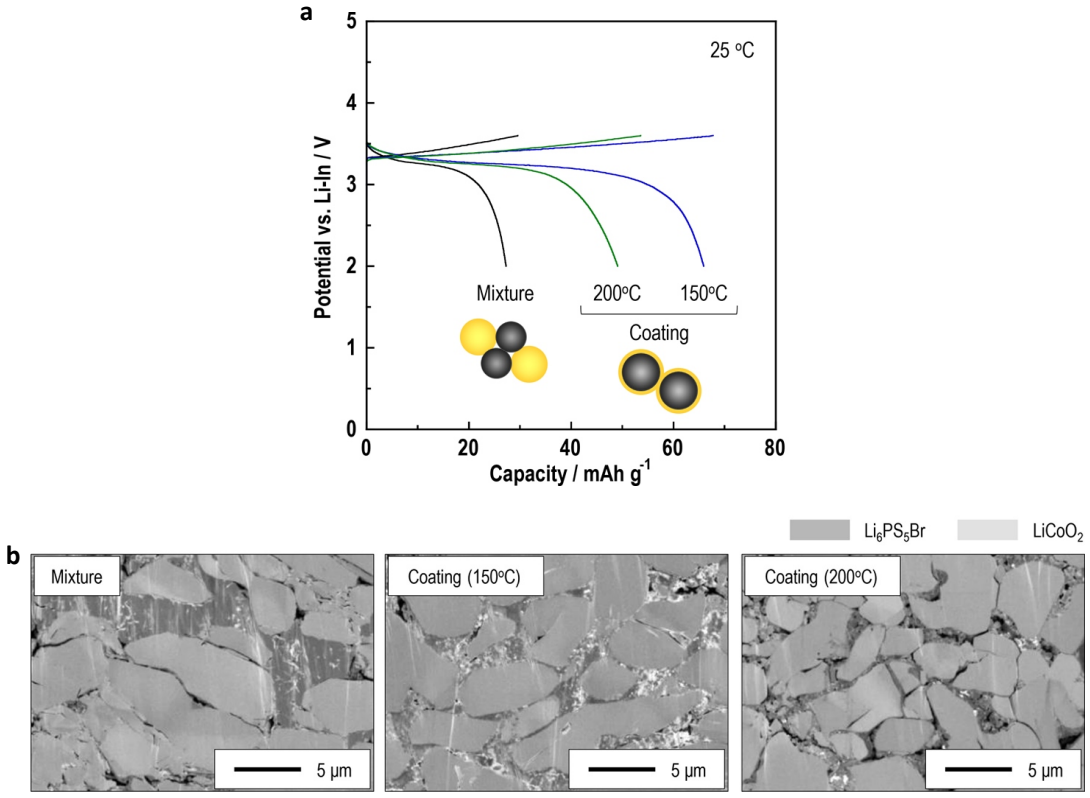


Fig. 2.10: (a) Charge/discharge curves, (b) and cross-sectional SEM images of a In/Li_3PS_4/LCO cell with a conventional dry-blended electrode prepared by hand-mixing of LCO and SE particles using a mortar, and the composite electrodes with the SE-coated LCO particles dried at 150 and 200 °C prepared via a liquid phase dissolution/reprecipitation technique. Reproduced from [93].

cell capacity of 110 mA h g^{-1} at 0.1 C (where 1 C represents a charge/discharge cycle of 1 h).

The same group investigated the influence of binder in a composite cathode [96] by dissolving BM-LPSCl in ethanol and subsequently adding VGCF and $LiNbO_3$-coated NMC along with ethyl cellulose dissolved separately in ethanol. The ionic conductivity without and with a small amount of binder was 1.8 × 10^{-5} S cm^{-1} and 2.5 × 10^{-5} S cm^{-1}, respectively. The superior conductivity for LPSCl with binder was ascribed to a higher pellet densification and greater mechanical integrity. However, the ionic conductivity with binder was much lower than in other reports and gave only a moderate capacity of <50 mA h g^{-1}. Moreover, cycle life was improved by the presence of 0.5 wt% binder. Thus, the performance of SSBs, similarly to LIBs, requires trade-offs between different performance aspects such as energy density, power density, lifetime, charge/discharge time, cost, etc.

Another approach was implemented by Han et al. who not only dissolved the electrolyte but also the active material and electronic conductive additive to fabricate a sulfur nanocomposite electrode [97]. LPSCl, Li_2S, and PVP were first dissolved separately in anhydrous ethanol and then mixed as shown in Fig. 2.11a. The mixture was then dried at 100 °C under vacuum for coprecipitation followed by further heating to 550 °C under Ar for carbonization of the PVP. The resulting powder comprised nanoscale Li_2S and LPSCl in a C matrix, as shown in Fig. 2.11b. To form a multiscale network in the composite cathode the powder was then further mixed with CB and a sulfide electrolyte and pressed at RT. The resulting cell with the composite cathode and a Li-In anode showed a relatively stable cycling performance at low current densities (capacity retention of >100% after 60 cycles at ∼0.1 C).

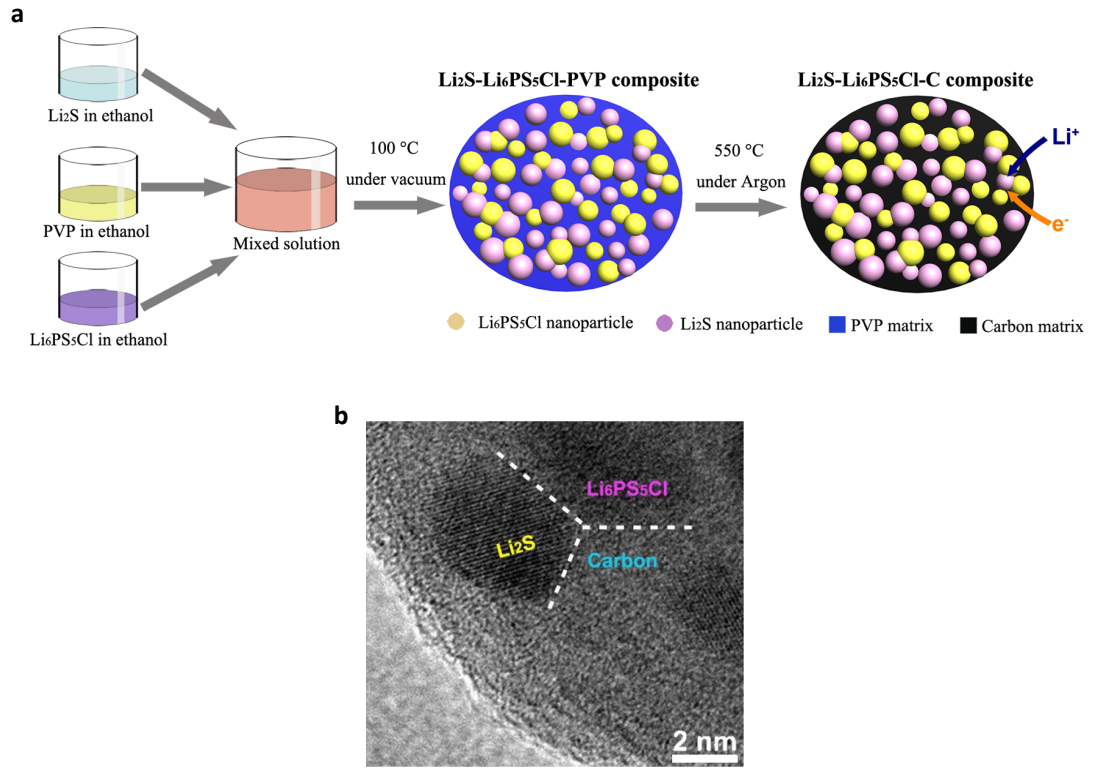


Fig. 2.11: (a) Schematic illustration of the bottom-up synthesis of the mixed conducting Li_2S nanocomposite. (b) High resolution TEM image of the as obtained Li_2S/LPSCl/C nanocomposite. Reproduced from [97].

Non-dissolution methods

This section covers approaches where the SE is not dissolved. Analogous to the CB, the SE can be seen as an additive in the cathode mixture to ensure an ionically conductive network throughout the electrode. As just described, the dissolution/precipitation methods suggested a reduction in sulfide ionic conductivity. Therefore, efforts have been made to develop wet-chemical methods where the relatively high intrinsic ionic conductivity of LPSCl can be better maintained. A smaller reduction in ionic conductivity (<1 order of magnitude) is generally reported on exposure to non-polar (non-dissolving) solvents. Xylene, toluene, heptane, n-decane and anisole are all considered suitable liquids to disperse sulfide electrolytes [21, 56, 98]. Fig. 2.12 shows the colour change of a series of differ-

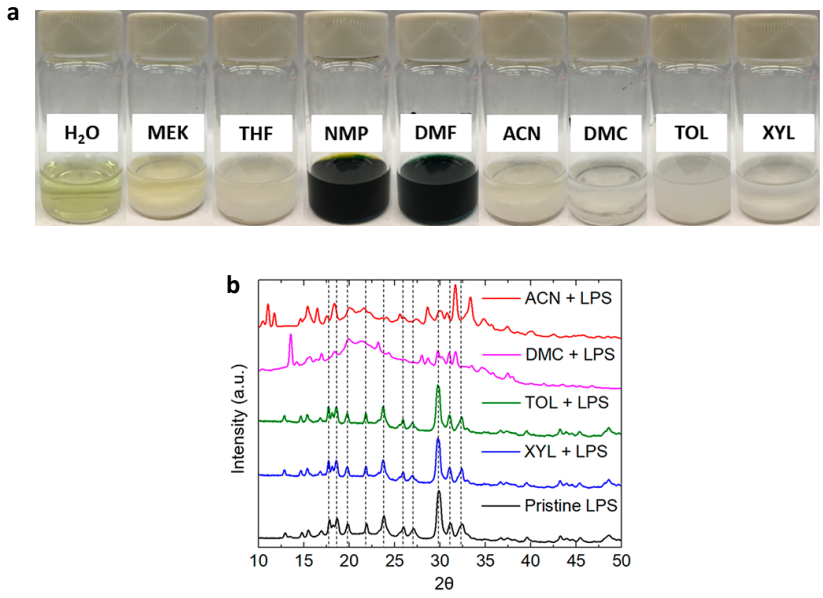


Fig. 2.12: (a) Changes of the solvent colour after the addition of $Li_7P_3S_{11}$ and (b) corresponding XRD spectra after solvent evaporation. Reproduced from [99]

ent solvents after the addition of a sulfide SE and corresponding XRD spectra after solvent evaporation. A dispersion of particulate electrolyte, active material, and CB can be used in combination with a dissolved binder to fabricate a SSB composite cathode.

Before blending methods of active material with sulfides are introduced, it is worth mentioning that wet slurry approaches have also been used to fabricate thin electrolyte layers between anode and cathode i.e. to act as both separator and ion conductor. Thin and reinforced sulfide electrolyte sheets were fabricated and compared with thicker pellets by Nam et al. [100]. Li_3PS_4 (LPS) and $Li_{10}GeP_2S_{12}$ (LGPS) were used as the electrolyte and dispersed in anhydrous toluene, without binder. The slurries were then coated onto a Ni foil using the doctor blade method. Once dried, the films were cold pressed onto a poly(paraphenylene terephthalamide) (PPTA) non-woven scaffold (NWS). After this pressing step, the Ni foil was peeled off while the sulfides adhered to the NWS, forming a

free-standing thin sheet. This process is shown in Fig. 2.13a with two different stacking orders of the sulfide electrolyte and the NWS. The films were 70 µm thick and were "bendable". This highlights a key subsidiary potential benefit of SSBs – the possibility for structural flexibility and new types of flexible packaging. The film ionic conductivity was $<1 \times 10^{-3}$ S cm^{-1} and lower than the directly pelletized powder, primarily due to the required exposure to toluene and the presence of the non-conductive NWS. On the other hand, the integration of the

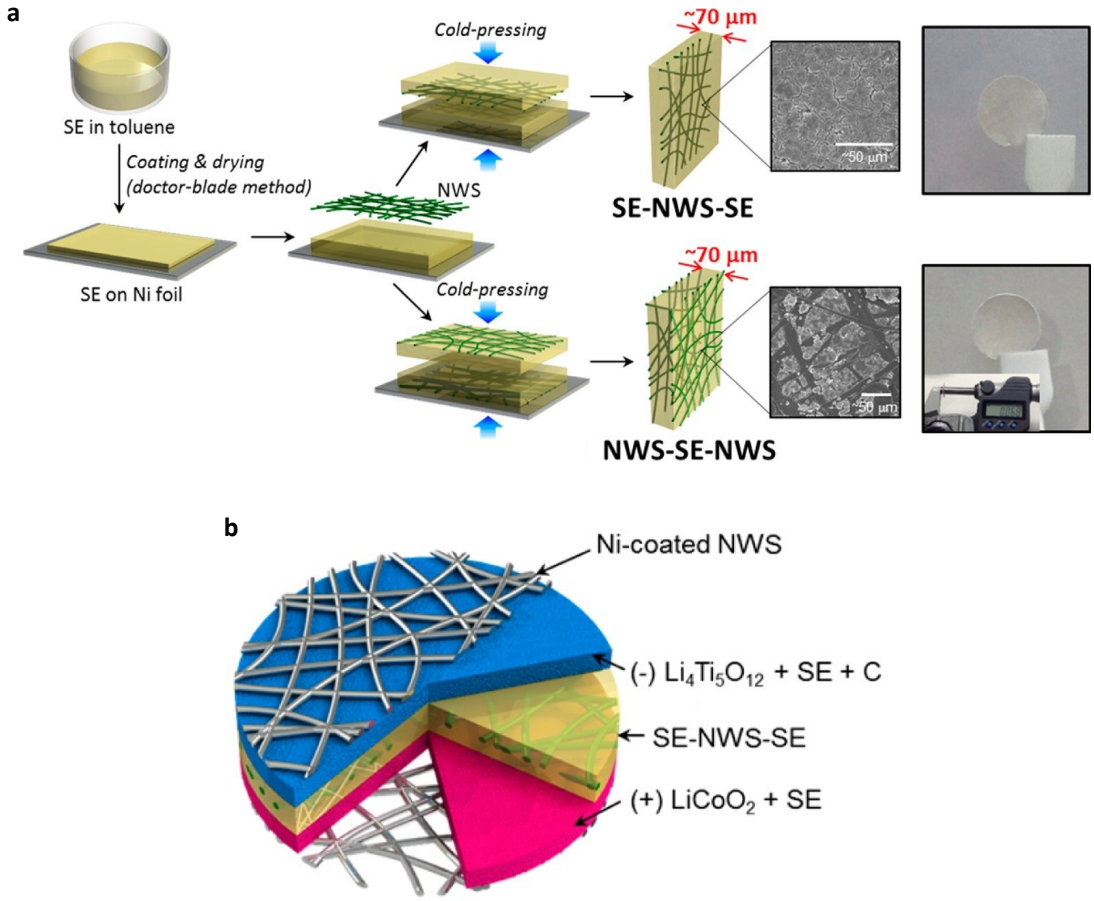


Fig. 2.13: (a) Schematic diagram showing the fabrication of bendable sulfide NWS-SE films with two different structures (SE-NWS-SE and NWS-SE-NWS). SEM and photo images are also provided. (b) Schematic diagram of the free-standing LCO/(SE-NWS-SE)/LTO all-solid-state cell. Reproduced from [100].

NWS in the sulfide electrolyte provided a mechanically compliant framework of higher flexibility and toughness.

The electrochemical performance of the film was investigated by assembling a full cell compressed between two Ti rods as follows. A powder mixture of $LiTiS_2$ (LTS), LPS and CB to form the cathode was spread onto the sulfide NWS film followed by cold pressing. The process was repeated using (LTO), LPS and CB to form an anode. The cell showed better capacity rate performance at higher current densities than a cell using the thicker pellet, which was attributed to the improved absolute conductance (from 14 to 37 mS) of the thin film. For example, at 29 C (4.4 mA cm^{-2}) the capacity of the thin sheet-type cell was roughly 4 times that of the conventional pellet cell.

The free-standing design shown in Fig. 2.13b was realized using the reinforced sulfide films. Electrode slurries were prepared using toluene as solvent: an anode based on LTO, sulfide SE and CB, and a cathode based on LCO, sulfide electrolyte and CB. Both slurries were coated onto Ni foils and transferred onto a Ni-coated NWS that served as current collector. Full cells were obtained by a final pressing of the electrodes together to sandwich a thin SE film. It should be noted that these types of free-standing cells can be suitable for stacking into multi-layer cells.

Several studies have focused on the fabrication of thin electrode coatings (40–100 µm) to be subsequently attached to electrolyte pellets and then pressurized between two metal rods [101–103]. For example, Choi et al. fabricated SSBs using LPSCl powder synthesized by a wet-chemical method and high-energy ball milling [101]. A slurry of LPSCl particles, $LiNbO_3$-coated NMC, CB, nitrile butadiene rubber (NBR), and xylene was cast onto Al foil to form a 90 µm thick cathode that was pelletized with LPSCl electrolyte powder using a uniaxial press. A matching anode was formed by pelletizing $Li_{0.5}In$ powder. Electrochemical

testing revealed better capacity retention for cells containing LPSCl made by liquid phase synthesis, which was attributed to a rod-like particle shape of the sulfide SE resulting in a more effective surface coverage of the active material. After the first 5 cycles at 0.1 C, capacity retention was 93% and 71% for the cell containing LPSCl synthesized by a wet-chemical approach and high-energy ball milling, respectively.

Yamamoto et al. chose a similar fabrication process for NMC/LPS/In SSBs with a high fraction of CAM and investigated the influence of pressure [102]. Micrometre-sized LPS, $LiNbO_3$-coated NMC, and acetylene black were dispersed in a solution of n-decane and styrene-ethylene-butylene-styrene (SEBS) binder by planetary mixing. The slurry was then sonicated, coated onto an Al foil, and dried at RT. Subsequent cell manufacturing was analogous Choi et al. but with an In foil anode and a pre-densification process [101]. The study gives an idea of suitable pressures of >100 MPa during cell fabrication but also that excessive pressure (e.g. 333 MPa) can result in undesired particle fracture.

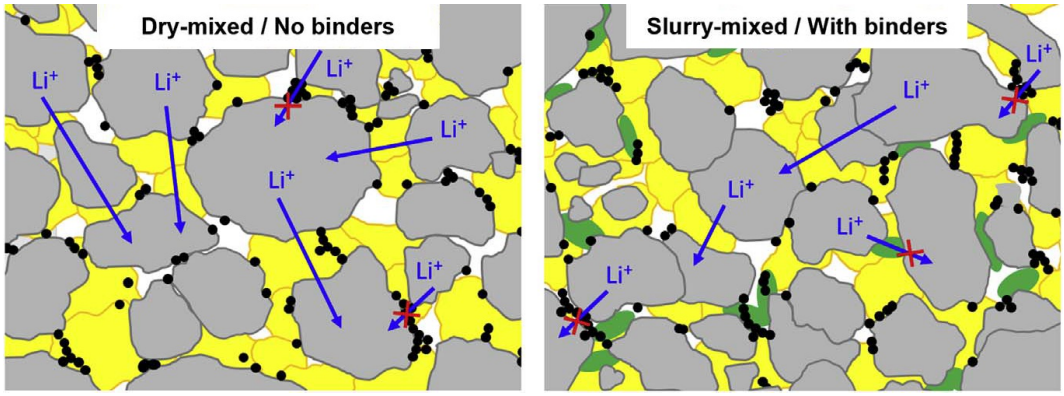


Fig. 2.14: Comparison of SSB electrodes fabricated by dry-mixing and wet-slurry processes. Active materials, SE, CB and polymeric binders (NBR) are shown in gray, yellow, black and green, respectively. Reproduced from [71].

A simple and scalable process for electrode manufacturing of bulk-type batteries was proposed by Oh et al. [103]. In a one-pot method, they directly dispersed the precursors of LPS, CB, $LiNbO_3$-coated NMC or graphite in tetrahydrofuran (THF) and added polyvinyl chloride (PVC) or NBR as binder. Slurry casting was used to form thin films that were dried and then pressed onto both sides of an LPSCl pellet. The results showed that NBR was more suitable as binder where high temperature drying was preferred because of the thermochemical instability of PVC. Furthermore, a reduction of precursor SE particle size from 10 µm to 1 µm, implemented by ball milling, led to a capacity increase from 45 mA h g^{-1} to 80 mA h g^{-1} at 1 C.

One of only few reports regarding sulfide-based SSB pouch cells was provided by Nam et al. [71]. A transition metal oxide/LPSCl/graphite battery with a high energy density was manufactured by slurry casting of both the electrodes and the electrolyte. First, electrode slurries of LPSCl, NBR, and xylene were prepared. $LiNbO_3$-coated NMC and CB were constituents in the cathode slurry while graphite was used in the anode slurry. The cathode and anode slurries were coated onto Al and Ni foils, respectively. After subsequent drying at 120 °C, an electrolyte layer was cast directly onto the surface of the anode using a xylene/NBR-based slurry. The cathode and the anode with the attached electrolyte were then compressed at 492 MPa to obtain an 80 × 60 mm^2 SSB. The presence of a binder in the pressed electrodes unsurprisingly lowered the capacity by ∼7% (at 0.025 C), because binder inevitably obscured some part of the active surface, as shown in Fig. 2.14.

Yamamoto et al. [98] confirmed that a non-conducting binder in the cathode undermines electrochemical performance. Therefore they developed an approach where the binder can be removed after cell stacking, by vacuum heating at 225 °C, as shown in Fig. 2.15a. Graphite/LPS/NMC full cells were fabricated using this

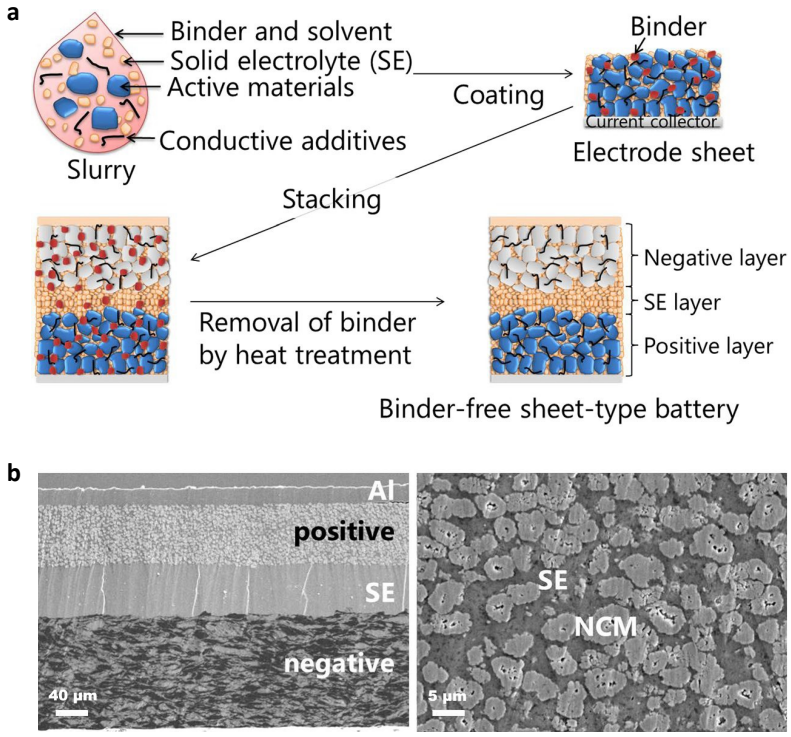


Fig. 2.15: (a) Schematic strategy for the fabrication of binder-free sheet-type SSBs. (b) SEM images of the intimate contact of the SE and positive/negative layer maintained over 350 cycles. Reproduced from [98].

method with anisole as a solvent in which polypropylene carbonate (PPC) was dissolved as volatile binder. Electrode slurries containing particulate $LiNbO_3$-coated NMC or graphite, LPS and acetylene black were coated onto Al and Cu foils representing cathode and anode, respectively. A similar electrolyte layer was then coated onto one of the electrodes and then pressed together with the other electrode to form a three-layered stack. Fig. 2.15b shows the stacked layers in cross-sectional images. Heat treatment was performed after initial pressing to remove the binder. This resulted in a conductivity increase from 1.1×10^{-4} S cm^{-1} to 4.3×10^{-4} S cm^{-1} in the electrolyte layer and a higher capacity of 122 mA h g^{-1} compared with 103 mA h g^{-1} (at 0.064 mA cm^{-2}).

A slightly different manufacturing approach was investigated by Sakuda et al. [89], again for sheet-type graphite/LPS/NMC full cells. Instead of casting onto the electrode, they prepared a separate electrolyte coating onto a release sheet or "carrier". The slurry for the SE layer was obtained by dissolving styrene copolymer (SBS) binder in anisole and then dispersing LPS powder. After drying and pressing, the carrier sheet was exfoliated to form a self-standing electrolyte. Fabricated sheet-type electrodes were then stacked together with the electrolyte under pressure (330–410 MPa) at RT. This resulted in a relatively thick SE layer (80 µm) and suggested that coating directly onto electrodes may be an option to reduce thickness.

To demonstrate that sulfide SEs are applicable for the fabrication of practical-sized cells, parallel stacking of NCA/$80Li_2S{\cdot}20P_2S_5$/graphite single cells was investigated [104]. Again, single layers were fabricated by slurry casting. For the cathode, $Li_2O{-}ZrO_2$ (LZO)-coated $LiNi_{0.8}Co_{0.15}Al_{0.05}O_2$ (NCA), sulfide electrolyte and carbon nanotubes (CNTs) were dispersed in anhydrous xylene in which a small amount of NBR based hydrocarbon polymer binder was dissolved. The cathode slurry was coated onto a carbon-coated Al foil and dried at 80 °C. The anode slurry comprised dispersed artificial graphite and dissolved polyvinylidene fluoride (PVDF) binder in N-Methyl-2-pyrrolidone (NMP). There was no incorporated sulfide electrolyte in the anode. The slurry was coated onto a Ni foil and fully dried, and a sulfide, NBR, and xylene slurry was cast onto the anode. Xylene was chosen as a solvent because it did not dissolve the PVDF binder of the anode layer underneath. The cathode and the anode with the attached electrolyte were compressed together to obtain a solid-state full cell. The anode, electrolyte, and cathode thicknesses were 100, 200, and 250 µm, respectively. A SSB was made by parallel stacking of 3 of these cells with an encouraging 80% capacity retention after 100 cycles at 0.1 C, without applying an external pressure. Electrode charge transfer resistance after initial charging and 100 cycles was obtained from

electrochemical impedance spectroscopy (EIS) and equivalent circuit analysis. The anode and cathode transfer resistances increased from 66 to 167 Ω cm^2 and 117 to 308 Ω cm^2, respectively.

2.3.2 Dry powder mixing

As an alternative to wet-chemical methods to produce bulk-type SSBs, simple dry powder mixing and subsequent pressing has been explored [105–108]. The common way of blending the individual phases is either pestle and mortar or a ball mill. If an electrode mixture does not contain any binder a cell is most frequently formed within an insulating plastic mould in which stacked powders are pressed by two metal rods, made of for example Ti or stainless steel. This approach is practical for small-scale laboratory applications because SSBs can be assembled rather quickly and without much equipment. However layer thicknesses, especially of the electrolyte, are significantly greater (typically in the range 300 µm to 1.5 mm) than those achieved by wet-chemical methods (30–300 µm) which results in a lower energy density. More recently the addition of a polymer binder into the powder mixture namely PTFE that shows fibrillation through shearing, a characteristic rarely found in other common binders, allowed the fabrication of larger sheet-type cells by rolling with thicknesses as low as 30 µm.

Boulineau et al. [109] published one of the earliest works on the fabrication of LPSCl full cells by simple powder mixing and pressing. The cathode mixture was obtained by grinding non-coated LCO, VGCF, and LPSCl in an agate mortar. The same route was used for an anode with LTO instead of LCO as active material. A cell was obtained by cold pressing the electrodes with a separating layer of LPSCl between two stainless steel rods, which also served as current collectors. Different ratios of active material and sulfide in the cathode were investigated while the percentage of electronically conductive additive was constant at 10 wt%. A low fraction of 40 wt% active material, 50 wt% LPSCl, and 10 wt% VGCF

resulted in higher capacities, but only reached 27 mA h g^{-1} compared with a practical capacity for LCO of ∼150 mA h g^{-1}. A comparatively high fraction of SE was required, but even at 50 wt%, not all the active material was effectively utilized due to inhomogeneity in the percolation of ionic and electronic currents to all parts of the electrodes. Consequently, cells tended to have much higher charge transfer resistances than their liquid electrolyte equivalents.

Different methods to mix the cathode components were investigated by Choi et al. [110]. Mortar mixing was compared with planetary ball milling in relation to the microstructure and electrochemical performance of subsequently created electrodes: the cathode comprised sulfur, acetylene black, and $70Li_2S{\cdot}30P_2S_5$, where the latter was also used for the electrolyte layer. Anodes were made of pulverized $Li_{4.4}Si$. Cells were fabricated by successive die pressing between two stainless steel rods using different mixing routes for the cathode. Cross-sectional SEM images of the cathodes fabricated by mortar mixing showed that the components were agglomerated and poorly dispersed. Ball milling at moderate revolution speeds resulted in a more homogeneous distribution. Increasing the milling time and revolution speed promoted smaller particles and thus resulted

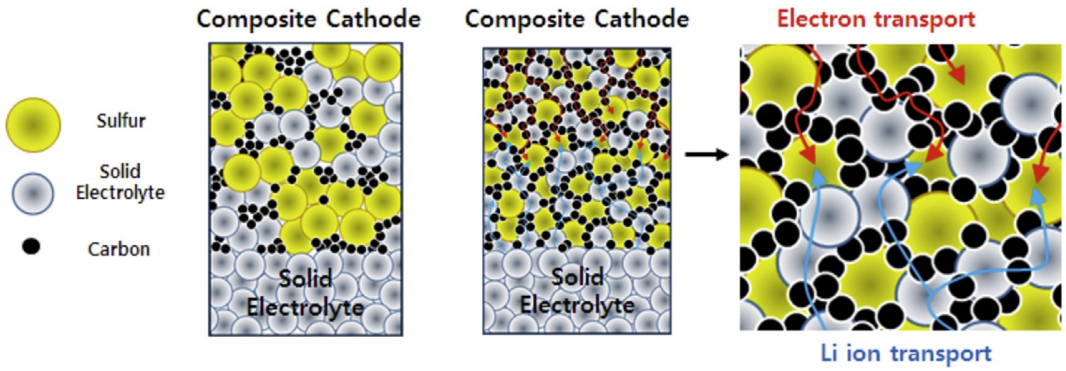


Fig. 2.16: Schematic diagrams of Li-ion and electron transport in a sulfur-based composite cathode consisting of large particles with non-homogeneous distribution, and small particles with homogeneous distribution. Reproduced from [110].

in a nearly tenfold increase in active surface area, which led to superior cell performance. Fig. 2.16 schematically shows the importance of a uniform particle distribution in a composite cathode – ensuring percolation of both ionic and electronic currents to all parts of the cathode.

To scale up small cells made by dry powder mixing with encouraging performance a process shown in Fig. 2.17 was developed whereby PTFE was added to act as an adhesive binder among the composite constituents [111]. A small amount of PTFE corresponding to 0.1–1 wt% of the entire composite was enough to hold individual cathode particles together because initially added PTFE particles (300–700 µm) turned into a much more effective shape of intertwined thin fibrils during processing. PTFE fibrillation occurred due to shear forces imposed by mixing with a heated pestle and mortar. A subsequent rolling step was carried out to make composite sheets that had a thickness of 50–200 µm and a porosity of ∼50%. It was pointed out that these films were foldable several times without breaking which might be a crucial factor for process scalability. A 30 × 30 mm^2 pouch cell was made by stacking an NMC-based cathode, a sulfide SE separator, and a graphite-based anode and subsequent pressing at ∼220 MPa that reduced porosity but likely caused PTFE fibrils to break. Although the PTFE might not have contributed to the integrity of the final cell it was nonetheless decisive for

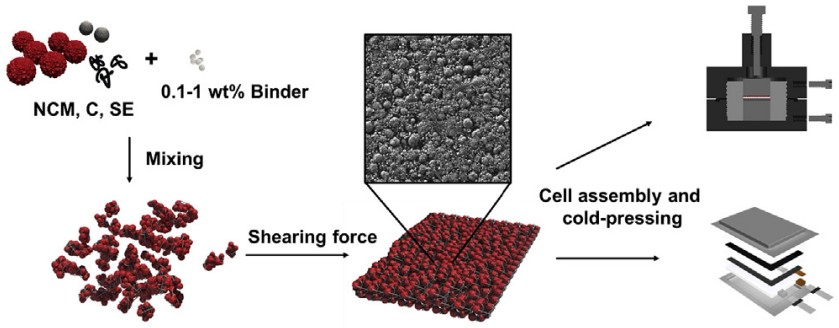


Fig. 2.17: Schematic of a large area dry cathode fabrication based on dry mixing NCM, C, SE, and PTFE followed by a shear force induced film formation. Reproduced from [111].

initial sheet preparation. The pouch cell achieved 115 mA h g^{-1} after 100 cycles at 0.7 mA cm^{-2} and RT.

The dry film process was also used by Samsung to make an NMC-based cathode for a 67 × 112 mm^2 pouch cell with a novel anode-free Ag-C layer that was made with a screen printer [26]. The SE separator sheet was fabricated by slurry casting and had a thickness of 30 µm after densification which was conducted after cell assembly on the pouch by warm isostatic pressing (WIP) at 490 MPa. Their approach again confirmed that the addition of PTFE is crucial for making thin films with relatively high porosity that requires further densification to increase the relative density which results in a lower interfacial resistance. The pouch cell had a high energy density of 900 W h L^{-1} and showed 89% capacity retention after 1000 cycles at 60 °C which is one of the best-performing sheet-type SSBs at the time of writing.

A low thickness of 30 µm was achieved by Zhang et al. who used the dry process shown in Fig. 2.17 to make sulfide SE separator sheets [112]. They used a planetary ball mill instead of the pestle and mortar for homogeneous PTFE fibrillation. Fabricated SE films had a high ionic conductivity of 8.4 mS cm^{-1} at RT.

2.3.3 Infiltration methods

Infiltration methods are an alternative to direct blending of the components of composite electrodes. They can be helpful in avoiding side reactions at high sintering temperatures. Generally, an inter-connected porous network within one or more of the components has to be created to which another phase can be infiltrated, in the liquid or gaseous state. For liquids, good wetting is required to ensure spontaneous infiltration. For gates, excessive tortuosity may lead to incomplete infiltration.

Active material infiltration

Wachsman and co-workers [38, 61, 113–115] have conducted the most numerous investigations of the fabrication of garnet-type SSBs. For example, they infiltrated active materials such as S and Li metal into a porous structure of $Li_{6.75}La_{2.75}Ca_{0.25}Zr_{1.5}Nb_{0.5}O_{12}$, as shown in Fig. 2.18. The garnet structure was first created by tape casting of two different types of slurries. Both slurries were obtained by grinding doped LLZO, isopropanol, toluene, a small amount of fish oil, benzyl butyl phthalate (BBP), and polyvinyl butyral (PVB). 10 µm cross-linked poly(methyl methacrylate) (PMMA) spheres were added to the slurry to act as sacrificial templates for pores. The slurries were degassed and cast separately onto a mylar substrate. Subsequently, LLZO layers were stacked at low pressure and small punch-outs were sintered at 1050 °C in a tube furnace. After an Al_2O_3

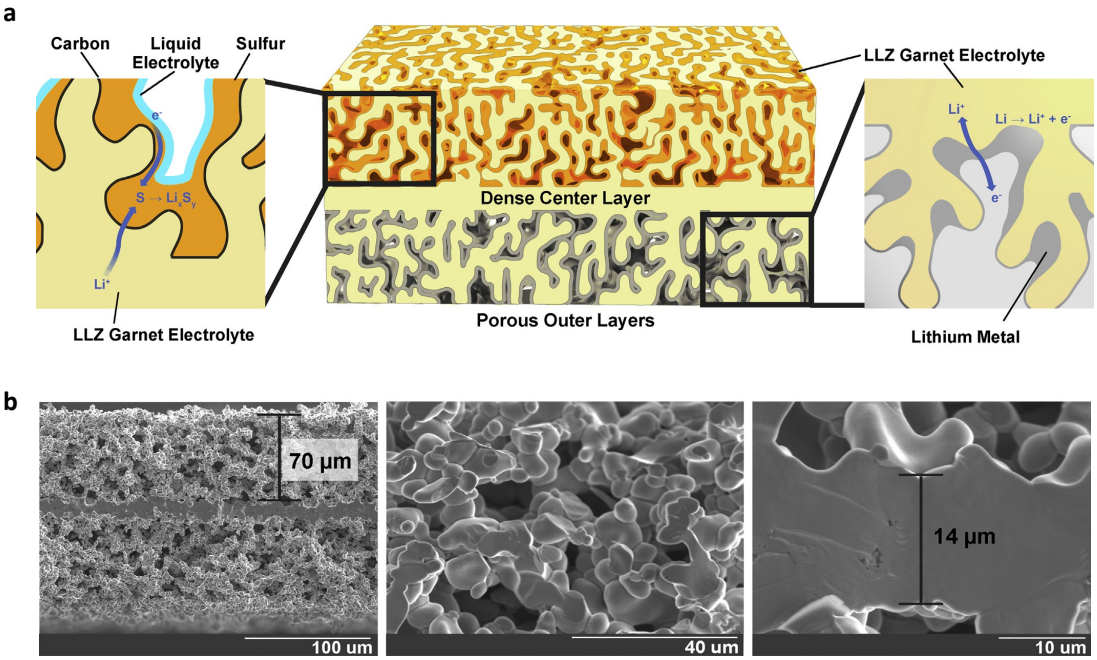


Fig. 2.18: (a) Diagram of a trilayer lithium garnet cell with high interfacial surface area, short Li-ion conduction pathways, and minimized use of electrolyte material. (b) SEM cross-section of the porous-dense-porous trilayer after binder burnout and sintering. Reproduced from [61].

coating was deposited by atomic layer deposition on the porous structure for better wettability, metallic Li was infiltrated on a hot plate at 350 °C under an Ar atmosphere. On the cathode side, electronically conductive CNT coatings were realized followed by infiltration of molten S, similarly to the approach by Wang et al. [116] who infiltrated a Li_2S/ethanol solution into a reduced graphene oxide cathode paper. The authors claim that this design may achieve energy densities beyond 400 Wh/kg, high current densities (10 mA cm^{-2}), and low contact resistances (∼7 Ω cm^2) due to a large area between active material and oxide electrolyte.

Electrolyte infiltration

Mixtures of sulfide SEs, for example, LPSCl in ethanol or $Li_7P_3S_{11}$ in acetonitrile have been used to infiltrate different electrodes made of either graphite, LCO, Si, or cobalt sulfide nanosheets [117–119]. Kim et al. [117] used conventional LCO/CB/PVDF electrodes to which they infiltrated LPSCl by simple dip-coating into LPSCl/ethanol solution. Subsequently, solvent evaporation led to reprecipitation of LPSCl, and a heat treatment was performed to improve ionic conductivity. Due to the limited thermal stability of the PVDF binder, the temperature was kept to a maximum of 180 °C. The initial porosity of the electrode changed from approximately 50% to roughly 35% after dip-coating and was further reduced to slightly under 10% by a vigorous cold-pressing at 770 MPa. The process is illustrated in Fig. 2.19a and cross-sectional images of the electrodes are shown in Fig. 2.19b. Although only a relatively small fraction of less than 20 wt% of sulfide electrolyte was infiltrated into the electrode, galvanostatic intermittent titration technique (GITT) measurements revealed a high surface coverage of the electrolyte onto the active material of ∼60%, which resulted in a high capacity of 140 mA h g^{-1} for a LCO/LPSCl/Li-In cell.

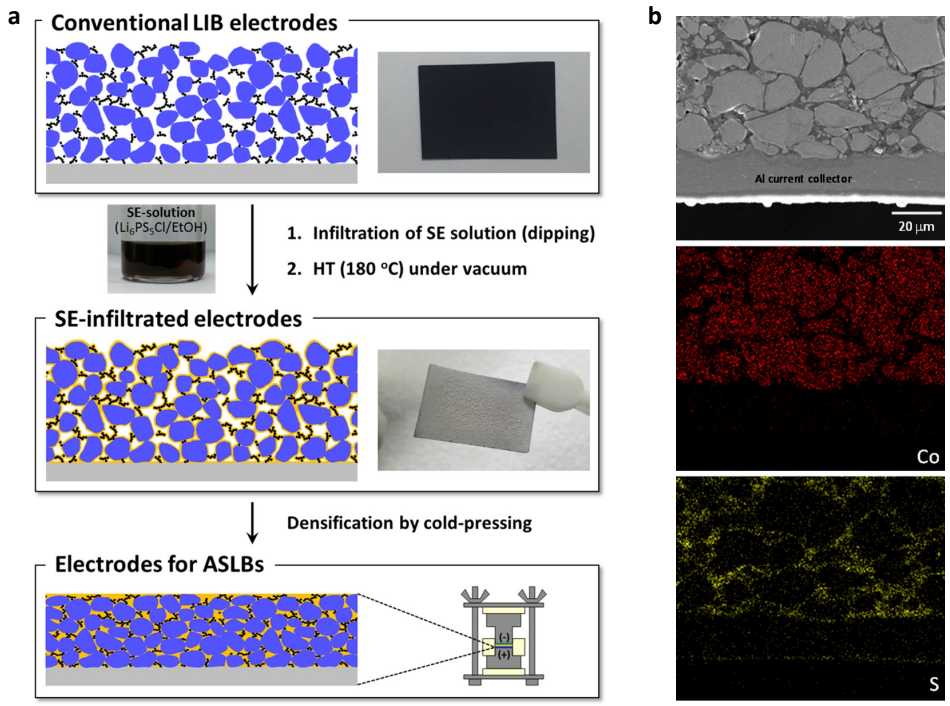


Fig. 2.19: (a) Infiltration of solution-processable SEs into conventional LIB electrodes to form SSBs. (b) Cross-sectional SEM image of the LPSCl-infiltrated LCO electrode and its corresponding EDX elemental maps. Reproduced from [117].

2.4 Conclusions and new science

This review has presented promising manufacturing strategies for bulk-type SSBs with a focus on sulfide-based architectures. Despite their high environmental sensitivity, and potential for reaction, the high intrinsic ionic conductivity and low flow stress of sulfides resulted in a higher processability compared with oxides, which was also reflected in better cell performance. Solid oxides require more sophisticated methods such as active material infiltration into a porous scaffold to create intimate contacts, especially with a focus on all-solid-state cells where no liquid electrolyte is added.

Although many approaches have been reported to create an intimate solid/solid contact in sulfide-based composite cathodes, many improvements such as increased

contact area between electrolyte and active material, higher mass fraction of active material, higher mass loadings, and current densities need to be realized in order for SSBs to prevail against conventional LIBs. Table 2.2 summarizes and compares electrode composition and the electrochemical performance of sulfide bulk-type batteries that have been prepared by dry mixing, wet-chemical blending, or an infiltration approach.

Low cell performance and fast degradation was generally observed when (i) materials were not compatible and reacted electrochemically, (ii) the active material volume change was large and caused mechanical decoupling, and (iii) the cathode microstructure was non-optimized and had, for example, a high porosity. The review has shown that manufacturing approaches to SSBs are immature and suggests that wet-chemical methods with dispersed sulfide SE and dry processing routes achieve best performance.

Within the wet-chemical approaches, the solution/dissolution method significantly decreased the SE ionic conductivity which as a consequence limited rate performance. The benefit of intimate sulfide active particle contact implemented by solution/dissolution is outweighed by the low flow stress of the sulfide SE that allows contacts of similar quality through a high fabrication pressure while still maintaining high ionic conductivity in the dispersion approach. On the other hand, SE solution/dissolution might find use where a high fabrication pressure cannot be used whilst still having good contact and might contribute to reducing the SE amount in the cathode for high energy density applications.

Wet-chemical approaches mainly rely on derivatives of slurry casting that is used ubiquitously for the billions/year conventional LIB market. While slurry casting is productive, it may not be optimum for SSBs where the permeation of liquid electrolyte throughout the pores of the electrode and separator is no longer possible. SSBs probably require new, near-full density electrolyte/separator layers

and electrodes with many particle/particle interfaces across which Li-ions and electrons must move with minimal resistance, even during contraction/expansion during charge/discharge.

While for wet-chemical methods some of the existing processes used for LIB production might be adapted, the upscaling of dry-processed SSBs might pose a stronger challenge. This is because process engineering for the dry film approach is still at an early stage and so far mixing is often conducted manually in a pestle and mortar or a ball mill and the first dry film coaters are still in development. The principle advantages of the dry film method are the absence of any liquid that entirely preserves the ionic conductivity of the sulfide SE and the compatibility with fibrillated PTFE binder that can be added at a low weight fraction that enables large cell formats with high performance.

Independent of the fabrication route, most reports suggested that a non-conductive binder is generally disadvantageous and from an electrochemical point of view should be kept at a minimum. However, it is likely that some binder is required during manufacturing even if it might lose the adhesive function later on as shown above exemplary through removal of the polymer by a heat treatment or breakage of fibrils through a subsequent compression step. Most fabrication routes rely on a high pressure of ∼500 MPa to densify the cell stack. While such pressure may be required to achieve acceptable densities some materials might be damaged by a high corresponding stress. This requires a careful selection of materials that can withstand harsh mechanical process conditions. Reports also suggest that best-performing cells, so far, rely on the application of a high stack pressure during cycling, in part to ensure microscopic interfacial contacts are maintained. Li dendrite formation on re-plating at the anode will also need to be suppressed e.g. as shown by a particulate Ag-C layer.

Manufacturing routes developed in this thesis will take essential process requirements into account from the time of material preparation to cell assembly and give recommendations for ideal materials. For instance, this work compares materials with different integrity which might also be beneficial for cycling. There is a particular need to select materials that are compatible with the high fabrication pressure required for sulfide-based cells. Compatibility must also be ensured among different materials to decrease the risk of possible side reactions.

Moreover, the different cycling performance among cells with similar materials in Table 2.2 shows that the cell microstructure has a great impact but was often neglected and non-optimized. This work investigates microstructural changes due to cycling that occur in carefully designed cell architectures. In this regard, this work helps to better understand to what extent the stack pressure can be lowered while maintaining acceptable cycling performance and what charging times can be expected if limitations such as dendritic Li growth can be overcome.

Lastly, the research focuses on a novel fabrication of sulfide-based cell components in a layer-by-layer manner, distinctly different to published research. Layer-by-layer confines drying to thin layers so that binder or precipitated SE migration is restricted to the single particle length scale. Layer-by-layer also allows deliberate, heterogeneous electrode architectures to be formed, which proved to be effective in enhancing electrode dynamics in LIBs [88]. With the development of a spray process for sulfide SEs there is the possibility to apply these ideas to solid-state electrodes where arguably improvements in electrode dynamics are even more valuable.

Table 2.2: Performance summary of sulfide-based SSBs. Anode active material (AAM), loading (l), mass fraction (f), capacity of the first discharge (C_1), capacity retention ($C_{\%,N}$) after number of cycles (N), current density (i), temperature (T), not available (NA).

Method	Electrode composition							Cell performance						Ref.
	Cathode						Anode	Capacity retention						
	CAM	Carbon	SE	Binder	l^{CAM}	f^{CAM}	AAM	C_1	$C_{\%,N}$	N	i_A	C-rate	T	
	-	-	-	-	$\frac{mg}{cm^2}$	%	-	$\frac{mAh}{g}$	%	-	$\frac{mA}{cm^2}$	-	°C	
Wet-C.	LTO	VGCF	LPSCl	-	2.5	50	Li-metal	158	94	250	0.01	0.05	80	[120]
Wet-C.	Li_2S	PVP+CB	LPSCl	-	3.6	40	Li-In	648	128	60	0.18	0.08	RT	[97]
Wet-C.	NMC	VGCF	LPSCl	-	11.3	89	Li-In	110	95	15	0.13	0.1	25	[95]
Wet-C.	NMC	VGCF	LPSCl	-	10.7	84	Li-In	140	80	25	0.13	0.09	25	[95]
Wet-C.	NMC	CB	LPSCl	NBR	∼14	68	$Li_{0.5}In$ p.	146	80	35	∼0.2	0.1	RT	[101]
Wet-C.	NMC	CB	LPSCl	NBR	14.3	68	Graphite	112	92	13	0.04	0.025	30	[71]
Wet-C.	NCA	CNT	$80Li_2S{\cdot}20P_2S_5$	NBR	20.6	59	Graphite	110	85	100	0.23	0.1	25	[104]
Dry M.	NMC	CB	LPSCl	-	29.3	79	Graphite	121	101	19	0.09	0.025	30	[71]
Dry M.	LCO	VGCF	LPSCl	-	NA	36	Li-In foil	108	84	4	NA	0.05	NA	[32]
Dry M.	c-LTO	-	LPSBr	-	13.3	70	Li-Al	150	63	30	0.2	0.1	75	[36]
Dry M.	S	CB	LPSCl	-	1.5	20	Li-In foil	1400	28	20	0.064	0.02	NA	[106]
Dry M.	S	MWCNT	LPSCl	-	1.2	24	Li-In foil	1850	75	50	0.176	0.09	RT	[107]
Dry M.	S	CB	LPSCl	-	3.4	33	Li-In foil	600	133	50	0.568	0.2	NA	[108]
Dry M.	Li_2S	CNF+CB	LPSCl	-	3.8	50	Li-In foil	419	24	21	0.13	0.08	RT	[33]
Dry M.	$Li_2S{\cdot}LiI$	CNF+CB	LPSCl	-	4.8	50	Li-In foil	663	48	40	0.13	0.05	RT	[33]
Dry M.	NMC	CNF	LPSCl	PTFE	29.8	85	Graphite	125	94	100	0.7	0.1	25	[111]
Dry M.	NMC	CNF	LPSCl	PTFE	30.7	81	Ag-C	145	89	1000	3.4	0.5	60	[26]
Infiltra.	LCO	CB	LPSCl	PVDF	10	86	Li-In	140	30	>86	0.14	0.1	30	[117]
Infiltra.	LCO	CB	LPSCl	PVDF	10	86	Graphite	75	96	79	0.7	0.5	30	[117]
Infiltra.	LCO	CB	LPSCl	PVDF	10	86	Si	∼90	73	45	0.28	0.2	30	[118]

Experimental techniques

This chapter describes the experimental techniques used to manufacture and characterize SSB components and materials. The experimental procedures and materials described are mainly used throughout the thesis with more specific details given at the end of each result chapter. All sample preparation and characterization that involved sulfide SE or other air-sensitive materials was carried out in an Ar-filled glovebox (O_2 and H_2O levels <1 ppm).

3.1 Cell manufacturing

3.1.1 Material preparation

Active particle coating

A cathode particle coating of $LiNbO_3$ based on a wet-chemical approach was used to reduce possible side reactions between the CAM and the sulfide SE in the composite cathode. 1 g of active powder was stirred in 400 µL lithium niobium ethoxide solution (Alfa Aesar, 5% w/v in ethanol) and 800 µL anhydrous ethanol for 1 h. The solvent was then evaporated under vacuum at 50 °C before heating under air to 350 °C (heating/cooling rate: 10 °C min^{-1}, holding temperature: 30 min) to calcine the cathode particles.

Sulfide solid electrolyte synthesis

In-house Li_6PS_5Cl of relatively small particle diameter (LPSCl small particle (SP), $d_{50} \leq 5$ µm) was made by mixing a stoichiometric ratio of 1 g of Li_2S, P_2S_5 and

LiCl in a 40 ml zirconia grinding bowl containing 16 × 10 mm zirconia balls in a planetary mill (Fritsch Pulverisette 7) at 600 rpm for 14 h.

3.1.2 Dry composite SSB electrodes

The manufacture of dry composite electrodes involved two main processes of first powder mixing and then powder consolidation. The cathode mixture was made by mixing sulfide SE, active material, and a carbon-conductive aid in a 40 ml zirconia grinding bowl containing 55 g of 5 mm diameter zirconia balls in a planetary mill (Fritsch Pulverisette 7) at 140 rpm for 30 min. Powder consolidation was implemented by a manual hydraulic press (Specac GS15011) and the use of a WC die-set (Maassen 54KB500M-H) which is described in further detail in the following subsections.

Binder-free electrodes

Binder-free electrodes were made by pressing typically 4–12 mg of the cathode mixture onto a sulfide SE pellet in a 5 mm plastic mould at 500 MPa.

Free-standing electrodes

1 wt% of polytetrafluoroethylene (PTFE, Sigma-Aldrich, particle size >350 µm) binder was mixed into the electrode mixture for 15 min using an agate pestle and mortar. Typically 4–12 mg of the PTFE cathode powder mixture was then consolidated in a 5 mm WC die-set at 250 MPa and subsequently expelled to obtain a free-standing electrode.

3.1.3 Metal anodes

Lithium indium alloy anodes

A lithium indium alloy anode was made by stacking and pressing a circular 5 mm diameter indium foil (Sigma-Aldrich, 100 µm thick) and a lithium foil (30 µm thick) onto a sulfide SE pellet at 500 MPa for 5 min using a WC die-set. The

thickness of the indium foil was varied and matched to the thickness of the lithium foil to explore different lithium concentrations in the lithium indium alloy using a laboratory calender (Sumet CA3/150-SP-GB).

Lithium anodes

Lithium anodes were prepared by rolling 1 mm thick Li foil from Sigma-Aldrich in a pouch to ∼50 µm using a laboratory calender (Sumet CA3/150-SP-GB). Circular anodes of 5 mm diameter were punched out with a hand-held stainless steel cutting tool (EMS core sampling tool).

3.1.4 Layer-by-layer spray printing

A spray deposition system (M-Solv, MSV-700G) placed inside an Ar-filled glovebox with four individual spray nozzles shown in Fig. 3.1 was used to spray-print thin (5–100 µm) particulate coatings in a layer by layer manner that acted as a SE separator, a composite cathode or were used to enable an anode-free SSB design. The spray process was supplemented by an integrated inspection vision system and a non-contact laser displacement height sensor that allowed for in-process quality control and dimensional monitoring.

The experimental set-up of one individual spray head is depicted in Fig. 3.2 and explained in more detail below. Typical spray mixtures were prepared by dissolving a polymer binder in an organic solvent using a magnetic stirrer. Subsequently, the particulate spraying material (∼500 mg) was added and stirred for at least 30 min. All suspensions were sonicated for 5 min (3 s on and 7 s off, 50% amplitude) inside the glovebox using an ultrasonic horn sonicator (Qsonica 500) prior to spraying. A reagent bottle containing the spray mixture was connected to the spray deposition system where the mixture was continually stirred during spraying to avoid particle sedimentation. The spray mixture was atomized by Ar gas in the spray nozzle and small droplets carrying the spray material were deposited

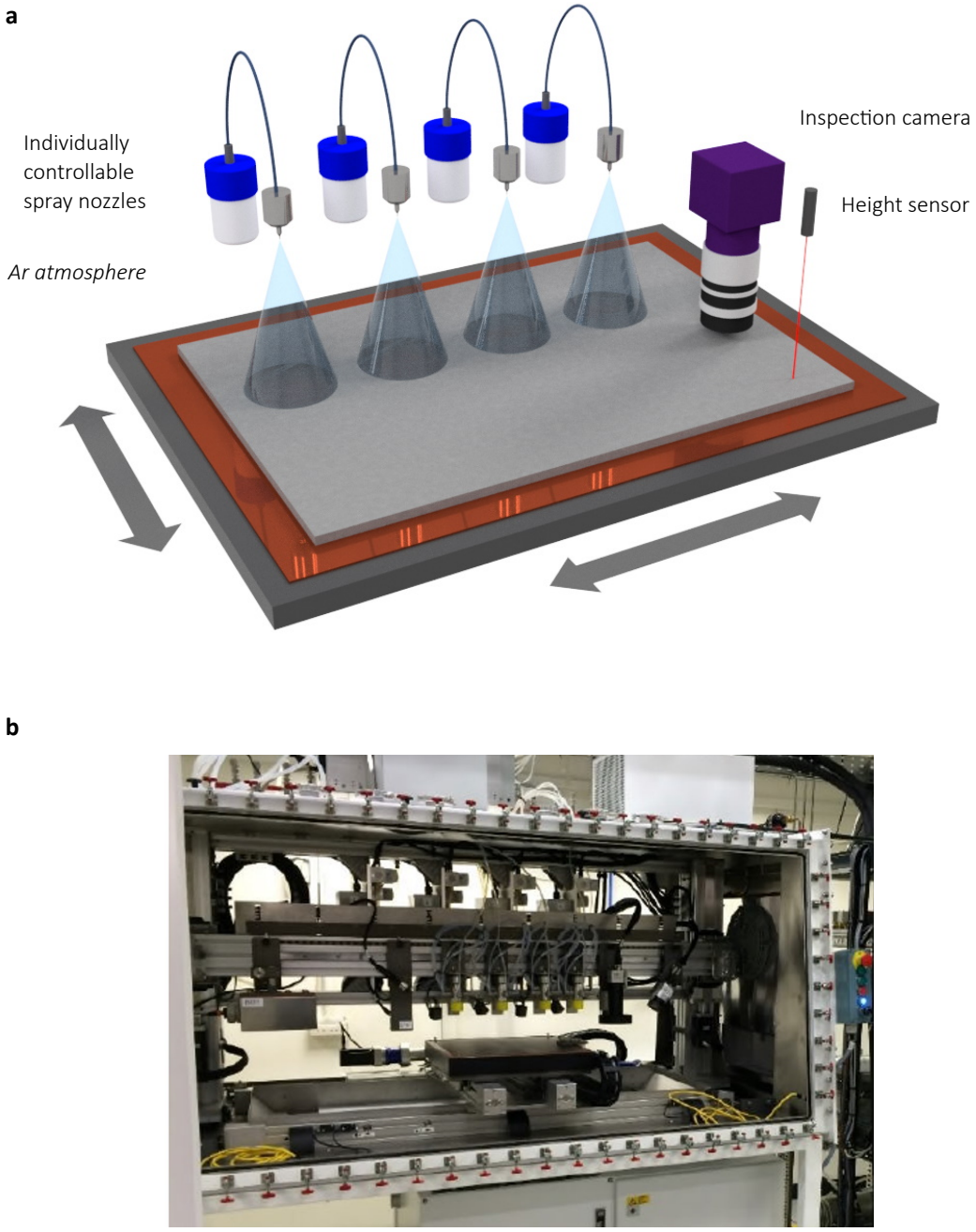


Fig. 3.1: (a) Schematic set-up of multi-head spray printing and (b) photograph of the spray deposition system used to spray print particulate layers in an Ar atmosphere.

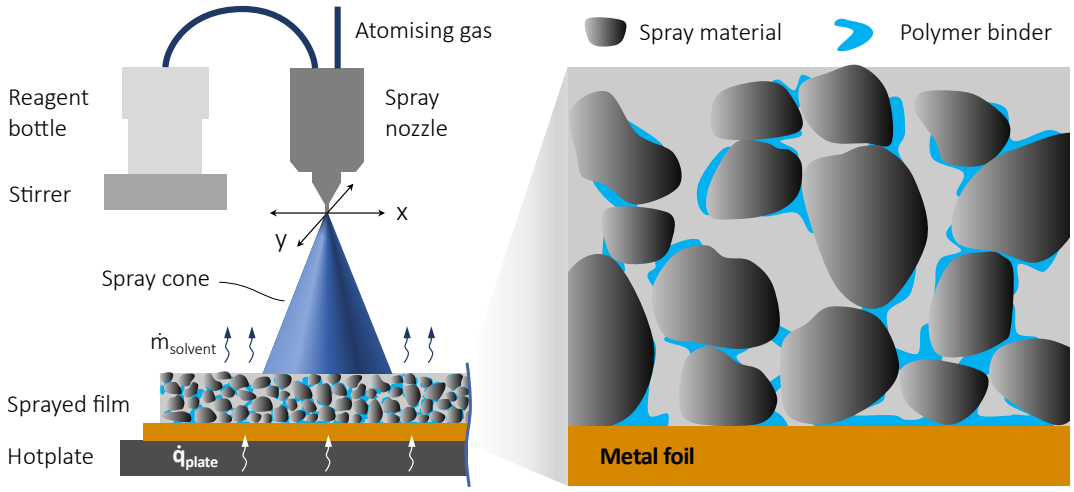


Fig. 3.2: Schematic of the layer-by-layer spray printing process used to deposit particulate coatings.

onto a heated metal foil (heat flow $\dot{q}$) where the solvent was evaporated (mass flow $\dot{m}$) and the polymer binder reprecipitated to adhere the spray material to the substrate. The metal foil was fixed by a vacuum chuck integrated in an Al hotplate which was kept at a constant temperature (in the range 110–150 °C). One layer was formed through a zigzag motion of the spray nozzle in the x and y direction (5 mm pitch) in relation to the substrate at a constant distance in the z direction (190 mm). Typical spray areas were 10 × 10 cm^2. One coating consisted of 5–20 sprayed layers depending on the concentration of the suspension and the targeted thickness. The magnified view in Fig. 3.2 shows schematically an example of a sprayed coating with a typical binder distribution and a high porosity (40–60%). Circular samples of 5 mm diameter were punched out and assembled in a PEEK cell set-up described in further detail in 3.1.5.

3.1.5 SSB assembly

SSBs were assembled in a set-up shown schematically in Fig. 3.3 that was developed and optimized within this project to enable cycling at a wide range of a defined stack pressure. A sulfide SE pellet made of typically 30 mg powder was pressed

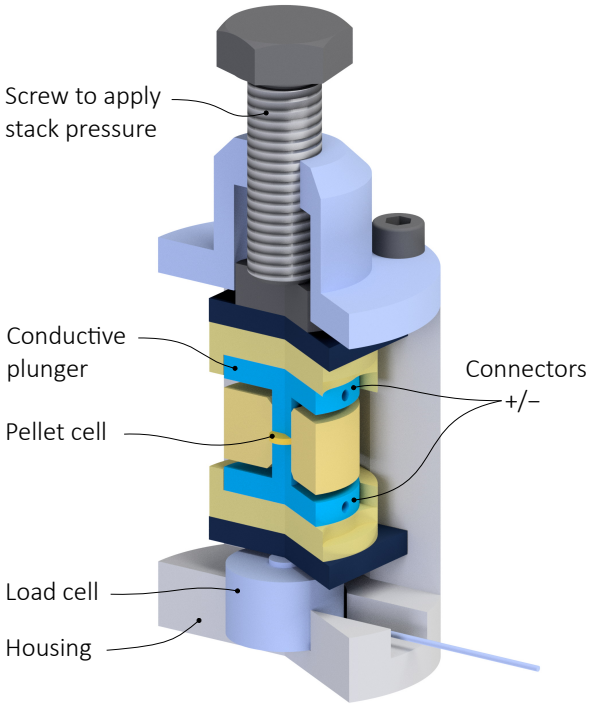


Fig. 3.3: Set-up and design used to assemble a SSB and to apply a symmetric stack pressure at the beginning of cycling.

in a PEEK mould (5 mm diameter) using a WC die-set (Maassen 54KB500M-H) at 250 MPa. Subsequently, depending on the cell stack a composite cathode and anode was added as mentioned in sections 3.1.2–3.1.3. A 30 µm thick Cu foil and a 15 µm thick Al foil were added as current collector for the anode and cathode, respectively.

Two conductive plungers made of stainless steel were placed on the electrodes of the pellet cell as shown in Fig. 3.3 and were used to connect the cell to a battery cycler and moreover provided a certain stack pressure by tightening the screw on top. A torque wrench (Bahco 1/4 in Square Drive, 0–9 Nm) was used to set a defined starting pressure before cycling which could be monitored by a load cell (Omega) placed at the bottom of the set-up. The relation between stack pressure and torque is shown in Fig. 3.4.

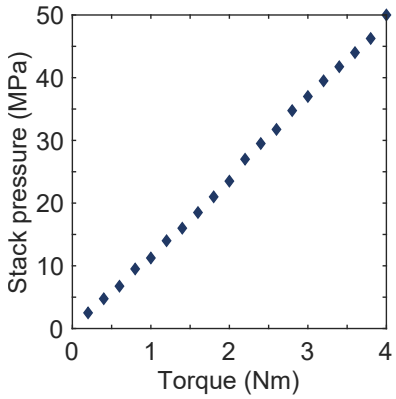


Fig. 3.4: Stack pressure as a function of torque determined by a load cell for a pellet with a diameter of 5 mm measured in the sell set-up shown in Fig. 3.3.

To study a low cathode stack pressure while maintaining a higher pressure at the anode an asymmetric set-up shown schematically in Fig. 3.5a was used. This was possible because of the high friction between the PEEK mould and the sulfide SE pellet which ensured that the pellet kept its position even though it was

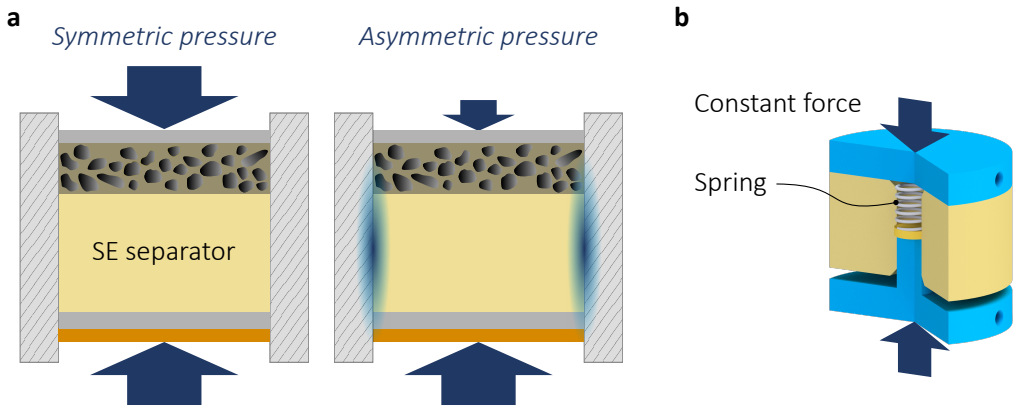


Fig. 3.5: Asymmetric stack pressure used (a) conceptually and (b) experimentally realized by a compression spring to lower the cathode stack pressure while maintaining anode pressure. The force from the spring measured by a load cell was 4 N which results in a cathode load of 0.2 MPa and compares well to the calculated values in Table 3.1.

Table 3.1: Details of the compression spring used in an asymmetric pressure set-up and resulting load on the cathode.

Shear modulus (MPa)	81500
Wire thickness (mm)	0.4
Mean diameter (mm)	4.15
Active coils	5
Spring constant (N/mm)	0.73
Spring deflection (mm)	5
Force (N)	3.65
Cell area (mm^2)	19.63
Cathode load (MPa)	0.19

loaded unequally. An asymmetric stack pressure was practically realized with a compression spring as shown in Fig. 3.5b. In this set-up the stack pressure applied by the top screw was mainly transmitted to the anode whereas the stack pressure on the cathode depended on the spring characteristics which are listed in Tab. 3.1. Calculations of the spring force are based on the analytical equations summarized in [121].

3-electrode measurements were prepared with a custom-made set-up shown schematically in Fig. 3.6a where a Li foil was attached on a 0.5 mm thick stainless

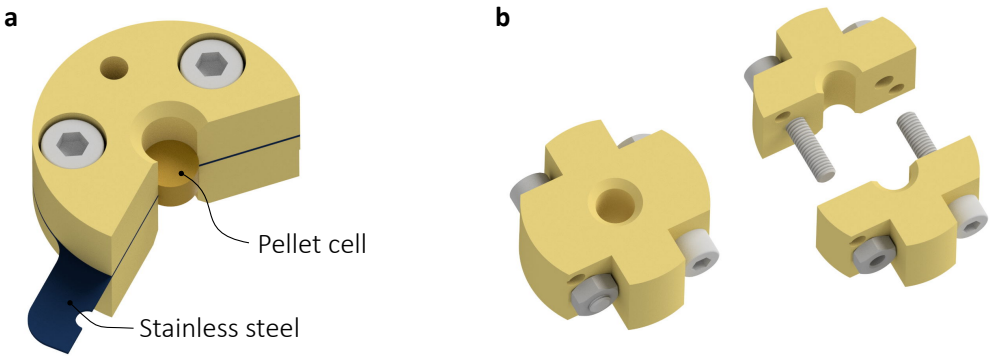


Fig. 3.6: (a) Set-up for the 3-electrode SSB cell assembly. (b) Dismountable PEEK mould used for the assembly and recovery of SSB cells for subsequent microstructural and pore volume analysis.

steel sheet that was adjacent to two PEEK insulating moulds to electrically separate the electrodes from one another. Subsequently, the pellet cell was formed in the mould as described above with the difference of using 100 mg of sulfide SE to avoid electrical contact between the reference electrode and the cathode or the anode. For the analysis of the microstructure of a cycled composite cathode a custom-made design shown schematically in Fig. 3.6b was used which consisted of a dismountable PEEK mould which simplified cell disassembly and ensured a lower risk of sample preparation induced cracks.

3.2 Physical characterization

3.2.1 Sample cross-sectioning

Analysed samples such as composite electrodes, pelletized and sprayed sulfide SE were attached on a Ti blade (Gatan) using Ag paste (Silver Dag - Electrodag 1415M). Cross-sections were prepared by an automated Ar ion polishing system (PECS 2, Gatan) at 8 keV and an etching time of typically 4 h.

3.2.2 Scanning electron microscopy (SEM)

Air and moisture-sensitive samples were transferred under vacuum or an Ar atmosphere into a Zeiss Merlin scanning electron microscope using an airtight transfer device. Images were taken by the Everhart Thornley and in-lens secondary electron detectors at an accelerating voltage of 3–10 keV.

3.2.3 Energy-dispersive X-ray spectroscopy (EDX)

EDX was carried out by an Oxford Instruments X-Max 150 silicon drift detector at an accelerating voltage of 10–15 keV and analysis was conducted in AZtec software.

3.2.4 X-ray diffraction (XRD)

XRD measurements were carried out in a Rigaku MiniFlex with Cu Kα_1 radiation inside an Ar filled glovebox. Patterns were typically collected from 10° to 90° in $\theta/2\theta$ using a step size of 0.01° at RT. Rietveld refinements were implemented in Profex software.

Powders

Analysed powders were placed on a Si low background holder. Powders were practically fixed with vacuum grease to avoid powder spillage during the measurement.

Sprayed coatings

The substrate of spray-printed coatings was mounted on a lowered Al holder using a pressure-sensitive adhesive (Blu Tack). The analysed surface was subsequently levelled with the holder using a glass plate.

3.3 Electrochemical characterization

3.3.1 Galvanostatic cycling

All cycling experiments were carried out at a constant temperature (30 °C, 60 °C or 80 °C) in a climate chamber (Huber) in an Ar-filled glovebox. A battery cycler (Bio-Logic or Gamry) was connected to cycle up to 50 cells simultaneously over a feedthrough as shown in Fig. 3.7. The system was implemented to ensure efficient cycling with high throughput and simple cell exchange. This was enabled by a combination of the simple design shown in Fig. 3.3 and the use of an inert glovebox since there was no need for any complex gas sealings and the entire cell assembly could be executed inside the glovebox.

SSBs were cycled at a constant current either in a 2-electrode or 3-electrode set-up as shown schematically in Fig. 3.8 where C-El stands for counter electrode, R-El

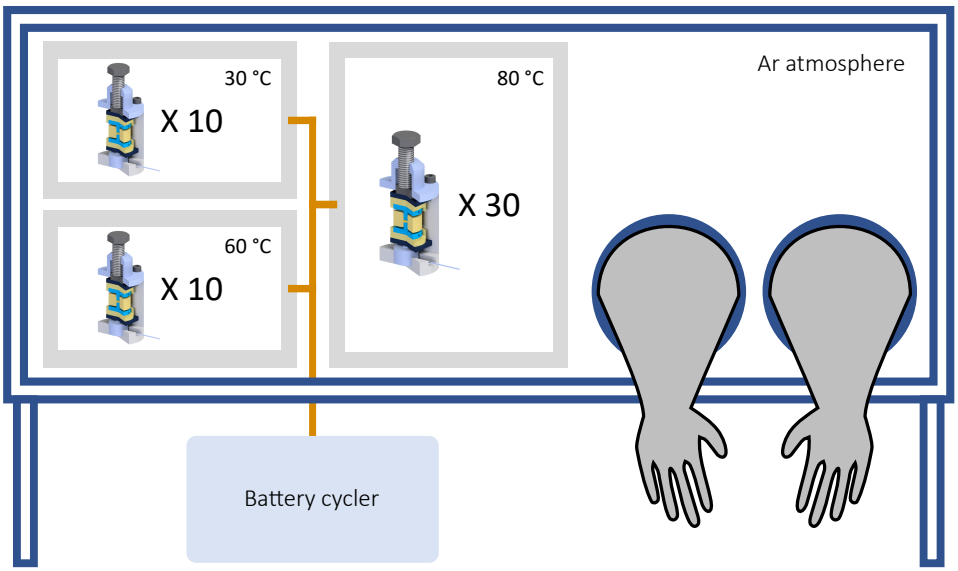


Fig. 3.7: Schematic diagram of the set-up used for SSB cycling in several temperature-controlled chambers in an Ar filled glovebox.

for reference electrode, W-El for working electrode and WS-El for working sense electrode.

2-electrode set-up

NMC-based composite cathodes were cycled galvanostatically between 4.3 V and 2.5 V vs. Li^+/Li using a Bio-Logic SAS Model BCS-805.

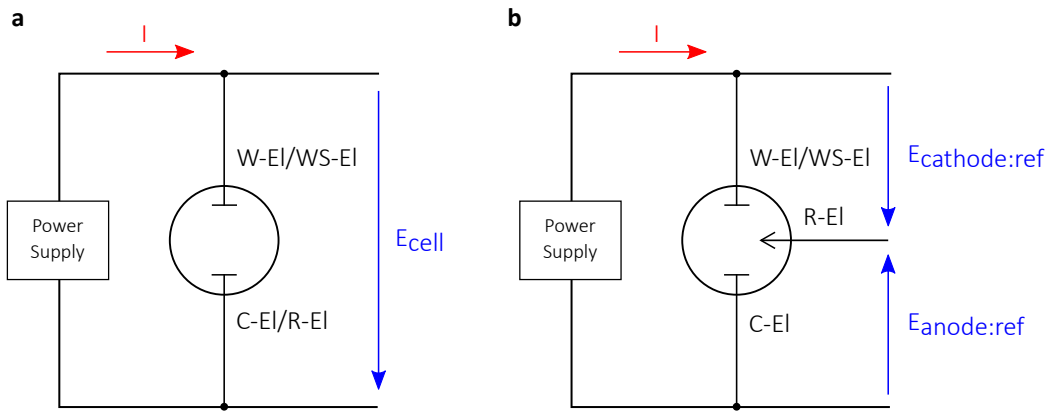


Fig. 3.8: Schematic representation of a (a) 2-electrode and a (b) 3-electrode set-up for cycling SSBs (adapted from [122]).

3-electrode set-up

In a 3-electrode cell configuration the reference electrode and the counter electrode are physically different electrodes as shown in Fig. 3.8b. This allows a separate analysis of the polarization at the anode and the cathode since the current flow is between the working and counter electrode and therefore not affecting the reference electrode which remains non-polarized [123]. The cell voltage measured in a 3-electrode set-up can be written as

$$E_{cell} = E_{cathode:ref} - E_{anode:ref} \tag{3.1}$$

where $E_{cathode:ref}$ is the voltage between the cathode and the reference electrode and $E_{anode:ref}$ the voltage between the anode and the reference electrode. To study the electrochemical performance of SSBs cycled at a high current density where significant polarization of several 100 mV occurs a third electrode was attached on the curved surface of the sulfide SE as shown schematically in the experimental set-up in Fig. 3.9.

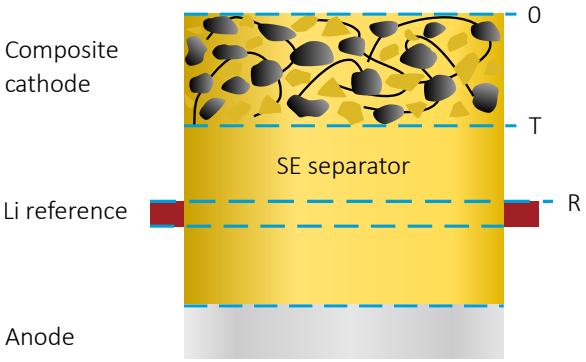


Fig. 3.9: Schematic set-up of a the 3-electrode SSB with a Li reference electrode, a composite cathode and a planar Li-In anode. 0: cathode surface, T: cathode thickness, R: position of the reference electrode from the surface.

3-electrode rate tests and 3-electrode EIS measurements (from 1 MHz to 0.1 Hz) were carried out using a Gamry 1000 potentiostat. To determine the voltage vs. Li^+/Li the position of the Li reference electrode had to be taken into account because the potential in the SE separator will vary with position. A transference number of 1 (no anionic movement) and therefore ohmic behaviour with a linear relation between voltage drop and thickness was assumed in the SE. The cathode voltage vs. Li^+/Li was calculated from

$$E_{cathode:Li^+/Li} = E_{cathode:ref} - I \cdot R_{SE} \tag{3.2}$$

with the resistance of the SE separator given by

$$R_{SE} = \frac{t_{T:R}}{\sigma \cdot A} \tag{3.3}$$

where $t_{T:R}$ is the distance between the cathode SE separator interface and the reference electrode as shown in Fig. 3.9, σ is the ionic conductivity, and A is the cross-sectional area of the pellet cell.

3.3.2 Electrochemical impedance spectroscopy (EIS)

EIS was used to determine the ionic conductivity of a sulfide SE pellet or a spray-printed coating and to study the interfacial resistances in a SSB.

Ionic conductivity

To determine the ionic conductivity of a SE powder or a spray-printed coating, a symmetric set-up was used in which the sample was stacked between two flat stainless steel electrodes as shown in Fig. 3.10a. Analysed powders and spray-printed coatings were placed into a PEEK mould where EIS was performed at different stack pressures (typically 500 MPa) using a manual hydraulic press inside an Ar-filled glovebox.

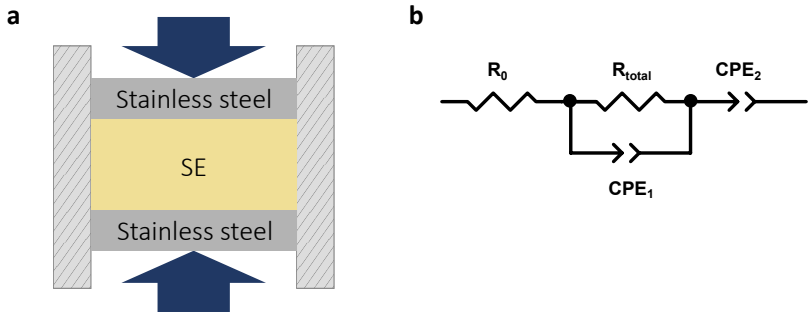


Fig. 3.10: (a) Schematic set-up for EIS to determine the impedance of sulfide SE powders and spray-printed coatings. (b) Equivalent circuit used to determine the ohmic resistance R_{total}.

EIS was performed in a Gamry Instruments Interface-1000 potentiostat using a voltage amplitude of 10 mV in the frequency range from 1 MHz to 0.1 Hz. The ionic conductivity was calculated with

$$\sigma = \frac{t}{R_{total} \cdot A} \tag{3.4}$$

where t is the thickness of the sulfide SE separator, A is the area of the electrode and R_{total} represents the total ohmic resistance in the SE originating from the grain/bulk and grain boundaries. Due to the high deformability of sulfide SE it is generally understood that the grain boundary resistance is much lower compared with other more brittle materials such as oxides. Nyquist plots therefore often only show one (compressed) semi-circle in which it is difficult to resolve grain and grain boundary contributions [124, 125]. R_{total} was determined in ZView version 3.5g using an equivalent circuit shown in Fig. 3.10b in which R_0 represents an offset resistance originating for example from the cables, CPE_1 represents a constant phase element which models the ionic conductivity together with the bulk and grain boundary resistance R_{total}, CPE_2 represents a constant phase element to describe the steep impedance increase after the compressed semi-circle at low

frequencies [124]. The SE separator thickness t was measured with a Mitutoyo 293-340-30 Digimatic micrometer.

SSBs

A combination of 2 and 3-electrode arrangements shown in Fig. 3.11 was used to analyse the impedance of (a) the entire cell, (b) the composite cathode, and (c) the anode.

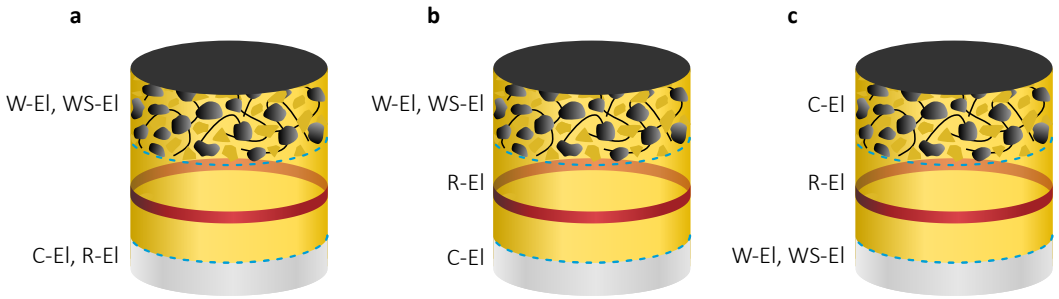


Fig. 3.11: Arrangements for electrochemical impedance spectroscopy analysing (a) the anode and the composite cathode, (b) the composite cathode, and (c) the anode. W-El: working electrode, WS-El: working sense electrode, C-El: counter electrode, R-El: reference electrode.

High energy density single crystal NMC/LPSCl cathodes for all-solid-state batteries

To match the high capacity of metallic anodes, all-solid-state batteries (SSBs) require high energy density, long-lasting composite cathodes such as Ni-Mn-Co (NMC)-based lithium oxides mixed with a solid-state electrolyte (SE). However in practice, cathode capacity typically fades due to cyclic volume changes of the active material and increasing NMC/SE interface debonding because of NMC pulverization, which is only partially mitigated by the application of a high cell pressure during cycling. A novel SSB cathode comprising single crystal particulate $LiNi_{0.83}Mn_{0.06}Co_{0.11}O_2$ and Li_6PS_5Cl achieved an outstanding discharge capacity of 210 mA h g^{-1} at 30 °C. A first cycle coulombic efficiency of >85%, and >99% thereafter, was achieved despite a 5.5% volume change during cycling. A near-practical discharge capacity at a high areal capacity of 8.7 mA h cm^{-2} was obtained using an asymmetric anode/cathode cycling pressure of only 2.5 MPa/0.2 MPa.

4.1 Introduction

An all-solid-state battery (SSB) offers a safer alternative to conventional Li-ion batteries (LIBs) by avoiding the use of flammable liquid electrolyte, and has the potential to increase cell energy densities by ∼70% because the graphite anode is replaced with Li metal [13]. To balance the capacity of this metallic Li anode, a thick (50–200 µm) composite cathode comprising a mixture of an electrochemically active material and an inorganic solid-state electrolyte (SE), such as a sulfide or oxide with high ionic conductivity (>1 mS cm^{-1}), is required [126]. A key

challenge to SSB performance is to achieve and maintain intimate interfacial contact and electrochemical stability between the particulate active material and the SE within this composite cathode [127]. Oxide-based SEs generally have a wide electrochemical stability window but are hard and resistant to deformation; in contrast, sulfides have a relatively low flow stress even at room temperature (RT) and can be manipulated into intimate contact with the active particles by applying an external load during processing and/or service [21]. As described earlier, among the sulfides, Li_6PS_5Cl (LPSCl) is considered a promising candidate material because of its comparatively high ionic conductivity and ability to form a relatively stable passivation layer at the interface with Li [40].

Lithium nickel manganese cobalt oxide (NMC) is a promising high energy density material for LIB cathodes with a discharge capacity >200 mA h g^{-1}. However, when used in a SSB, the NMC-based composite cathodes often show insufficient discharge capacity, and/or are cycled at impractical stack pressures ($\gg$5 MPa) [128, 129]. The cyclability of cathodes based on polycrystalline (PC) NMC in LIB and SSB formats was compared, and NMC cracking during charge/discharge due to particle swelling/contraction and pulverization was observed [130]. This led to the progressive creation of new active surface that could be wetted by a liquid electrolyte but not by a SE [130]. Pulverization and the progressive loss of contact between the active material and the SE results in rapid capacity reduction. Further, cracking may occur not only during cycling but during manufacture where pressures >100 MPa are frequently used in an effort to reduce or eliminate composite cathode porosity [102]. Thus, there is a complex interplay between the pressures and strains experienced by composite cathodes during manufacture and service, and the integrity and resilience of the active/SE interface, which in turn controls achievable capacity and cycle life.

In comparison with PC-NMC particles (an agglomeration of smaller crystalline particles), cathodes using single crystal (SC) NMC particles (discrete, non-agglomerated crystallites) have shown relatively good cyclability in LIBs, ascribed to their more isotropic volume expansion during charge/discharge [131, 132]. Recently, SC-NMC-based cathodes have been investigated for SSBs, albeit with relatively low Ni content to restrict cycling-induced volume changes (at the expense of reduced discharge capacity) [66, 133, 134]. Liu et al. investigated a SC $LiNi_{0.8}Mn_{0.1}Co_{0.1}O_2/Li_{10}SnP_2S_{12}/Li_4Ti_5O_{12}$ SSB that delivered a maximum discharge capacity of 187 mA h g^{-1} under a stack pressure of 25 MPa [135]. Although the cycling performance of the SC-NMC-based cathode was superior to a PC-NMC-based counterpart, the coulombic efficiency (CE) of the first cycle was only 74% and significantly lower than a conventional LIB equivalent (89%).

4.2 Results and discussion

4.2.1 Optimization of the cathode architecture

To achieve high energy SSB composite cathodes, and to better realize the theoretical performance of the constituent materials, smart processing, and cycling protocols are required that optimally engineer interaction between active particles, the SE, and electron conductive additives. The composite cathode fabrication route must provide percolating ionic and electronic networks and maximize the active/SE contact area while minimizing porosity and damage.

Commercially available SC $LiNi_{0.83}Mn_{0.06}Co_{0.11}O_2$ powders of small crystal size (1–2 µm) were chosen, as shown in the scanning electron microscopy (SEM) image in Fig. 4.1a. The particle size distribution is shown in Fig. 4.1b with $d_{50} = 3.4$ µm and was obtained by dynamic light scattering (DLS). Electron backscatter diffraction (EBSD) images of cross-sectioned SC-NMC particles shown in Fig. 4.2a confirmed that there was moderate particle agglomeration in the SC material. To understand any processing and cycling benefits of the SC-NMC morphology, additional cells

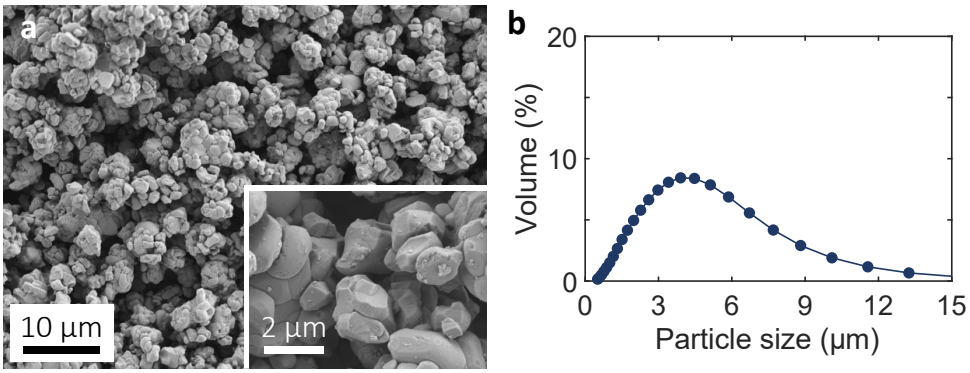


Fig. 4.1: (a) SEM micrograph of the as-supplied SC-NMC powder and (b) corresponding particle size distribution. DLS data was obtained by the help of Isaac Capone (Post-doc, University of Oxford).

were prepared using chemically similar $LiNi_{0.8}Mn_{0.1}Co_{0.1}O_2$ powder but with a PC-NMC morphology. An identical methodology was applied for fabricating SSBs

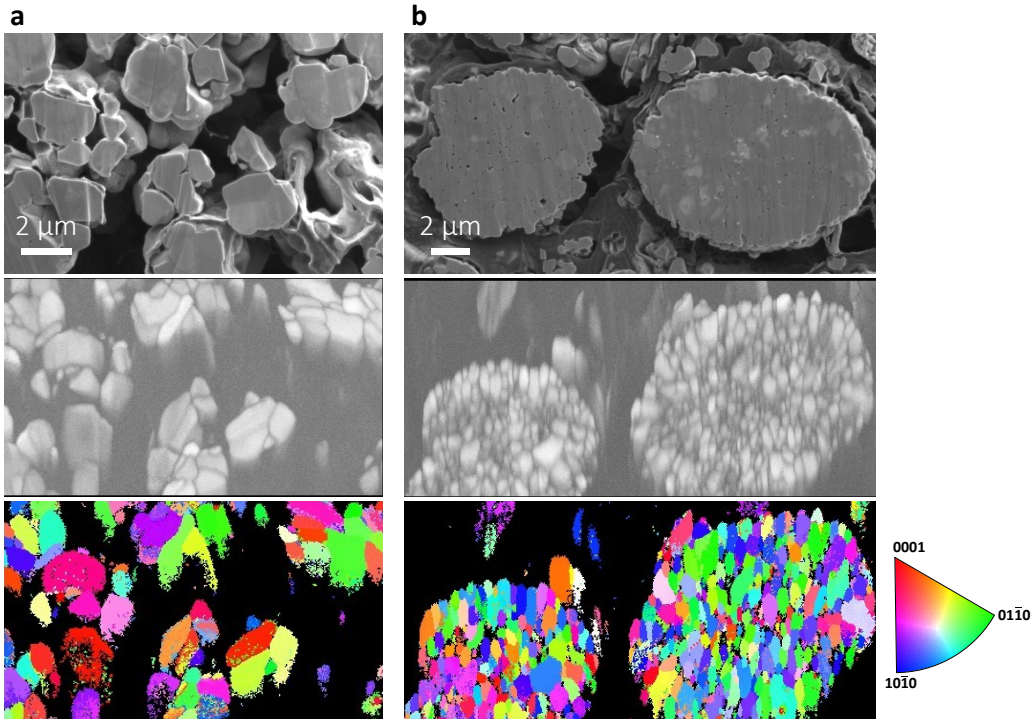


Fig. 4.2: SEM image (top), pattern quality map (middle) and inverse pole figure map (bottom) of (a) SC-NMC and (b) PC-NMC particles. EBSD data was obtained by the help of Junliang Liu (Post-doc, University of Oxford).

for both cathode active materials (CAMs). Fig. 4.2b shows an EBSD image from cross-sectioned PC-NMC particles, with significant agglomeration of secondary particles and d_{50} = 5.9 µm. This highlights the difference from the SC-NMC material, which had a lower agglomeration, smaller particle size, and slightly larger crystal size.

Since the SC material had only recently become commercially available, crystal structure and composition were investigated and this data was used as a baseline for the investigation of structural changes during cycling. The crystal structure of SC-NMC was revealed by X-ray diffraction (XRD) as shown in Fig. 4.3 and the lattice parameter obtained from the corresponding Rietveld refinement in Table 4.1 matched well with reported values from similar materials [136]. To verify the composition of the SC-NMC, EDX signals such as shown in Fig. 4.4 were evaluated. Results of the atomic composition are shown in Table 4.2 and confirm the supplier's stated ratio between Ni-Mn-Co.

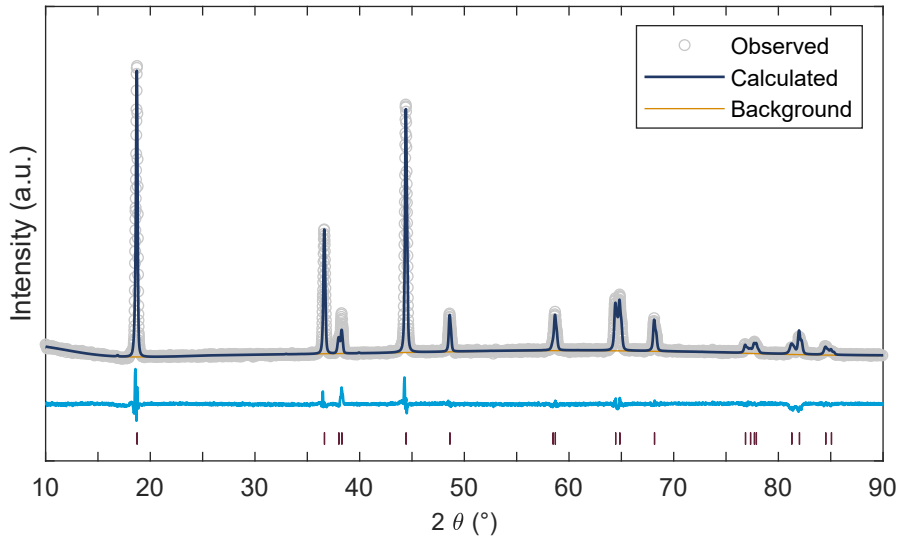


Fig. 4.3: XRD spectra of pristine SC-NMC and corresponding Rietveld refinement.

Table 4.1: Rietveld refinement of SC-NMC using R$\bar{3}$m space group before and after cycling.

	Pristine	Charged (4.3 V)	Discharged (2.5 V)
a (Å)	2.8727	2.81354	2.8686
c (Å)	14.1958	14.0151	14.2336
χ^2	2.04	3.96	1.08
R_{exp}	1.47	1.86	2.4
GoF	1.43	1.99	1.04

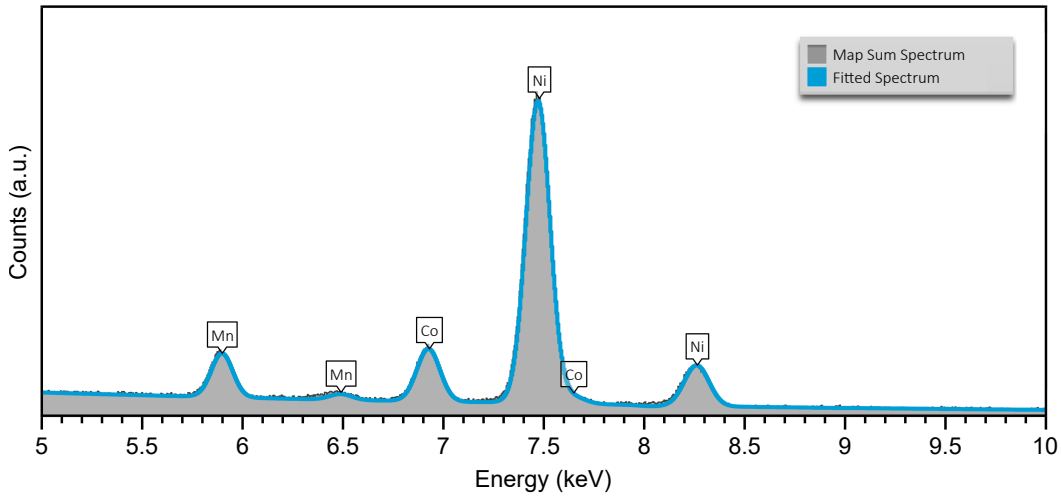


Fig. 4.4: EDX spectra of pristine SC-NMC particles.

Table 4.2: Composition of SC-NMC from the EDX analysis shown in Fig. 4.4.

Element	Nominal (%)	Measured (%)
Ni	83	82.8
Co	11	11.3
Mn	6	5.9

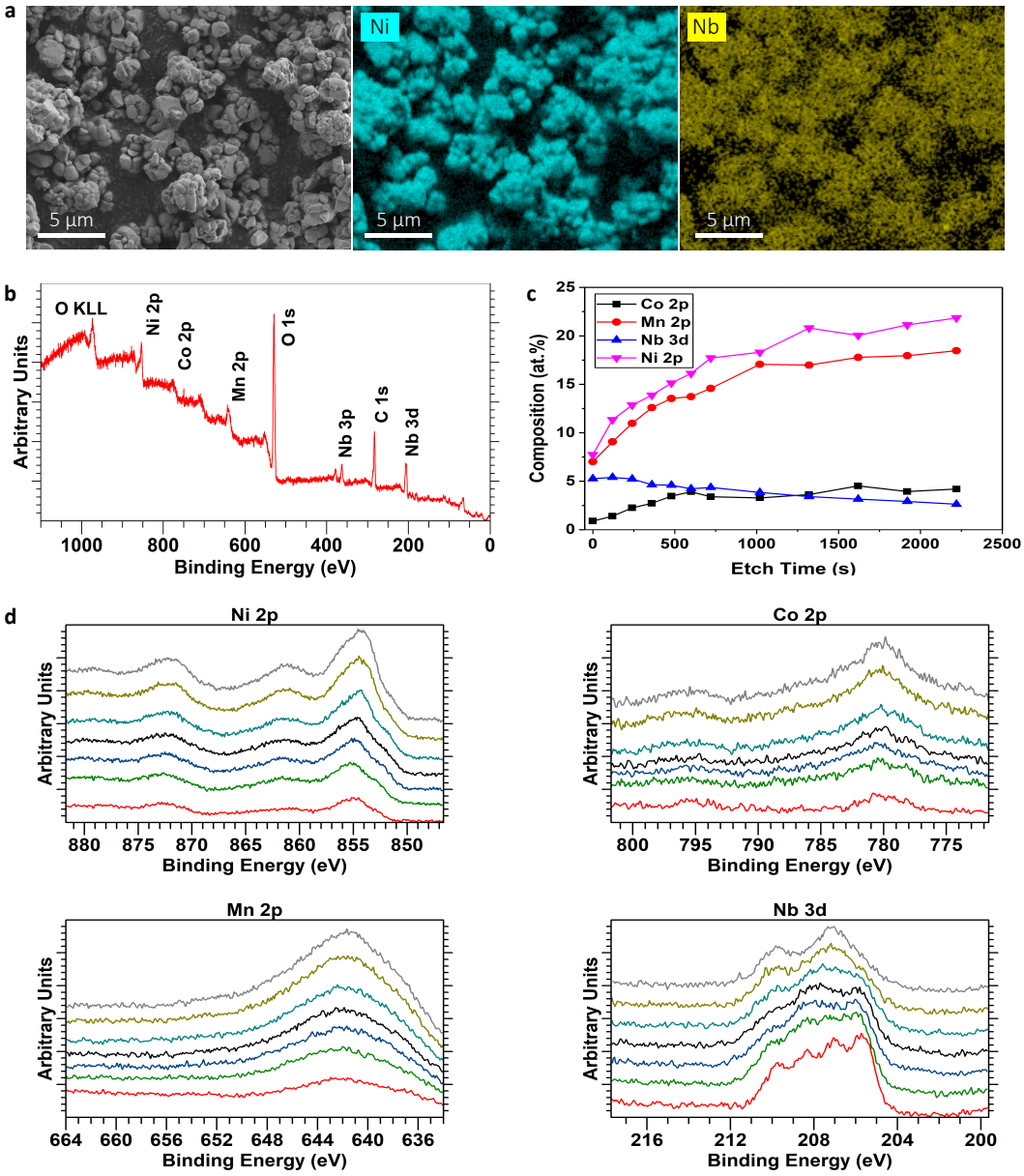


Fig. 4.5: Analysis of the $LiNbO_3$ coating. (a) SEM images of $LiNbO_3$-coated SC-NMC particles and corresponding EDX element maps for Ni and Nb. (b) XPS survey spectra with characteristic peaks for Ni, Mn, Co, Nb, and O; (c) estimated composition depth profile from XPS quantified high-resolution spectra as a function of etch time; and (d) corresponding XPS spectra stacked in order of increasing etch time. XPS data was obtained with the help of Sudarshan Narayanan (Post-doc, University of Oxford).

To restrict interfacial reaction with the LPSCl SE, NMC powders were coated first with $LiNbO_3$ using a wet-chemical approach [137, 138]. EDX and X-ray photoelectron spectroscopy (XPS) analyses of coated SC-NMC particles shown in Fig. 4.5 confirmed the presence of a Nb-rich surface oxide.

The particle diameter ratio between the active powder and SE powder has an influence on subsequent mixing and consolidation behaviour, and a ratio of ≥ 1 (SE powder diameter $\leq$ active powder diameter) has been suggested to promote efficient active material utilization i.e. each active particle is intimately surrounded by SE [49]. Therefore, bespoke LPSCl powder was prepared to match the SC-NMC diameter by ball milling a stoichiometric Li_2S, P_2S_5 and LiCl mixture to give a relatively small particle (SP) size of 1–5 µm as shown in Fig. 4.6a. However, for the SE separator and for convenience, commercial LPSCl was used, shown in Fig. 4.6b, with a relatively large particle (LP) size of 1–20 µm.

LPSCl ionic conductivity was measured by electrochemical impedance spectroscopy (EIS) with two stainless steel blocking electrodes at different stack pressures. There was a monotonic decrease in impedance up to a stack pressure of >500 MPa as shown in Fig. 4.7. Increased impedance at higher pressures might be due to

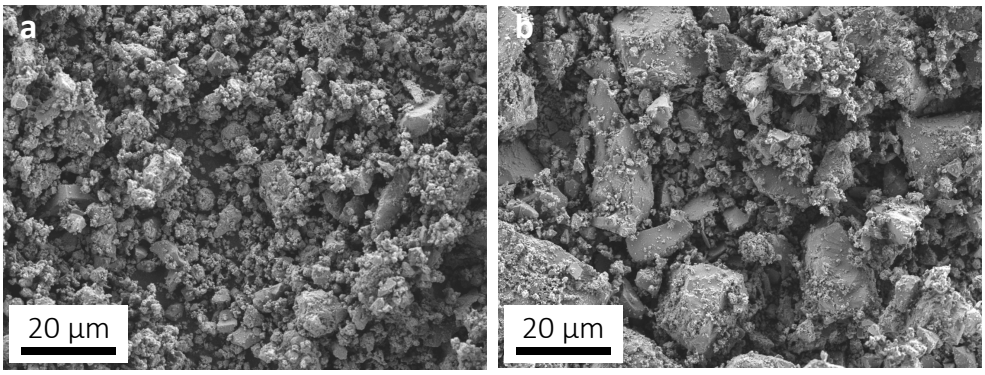


Fig. 4.6: SEM micrograph of the (a) in-house LPSCl-SP used in the composite cathode and (b) as-supplied LPSCl-LP used in the SE separator.

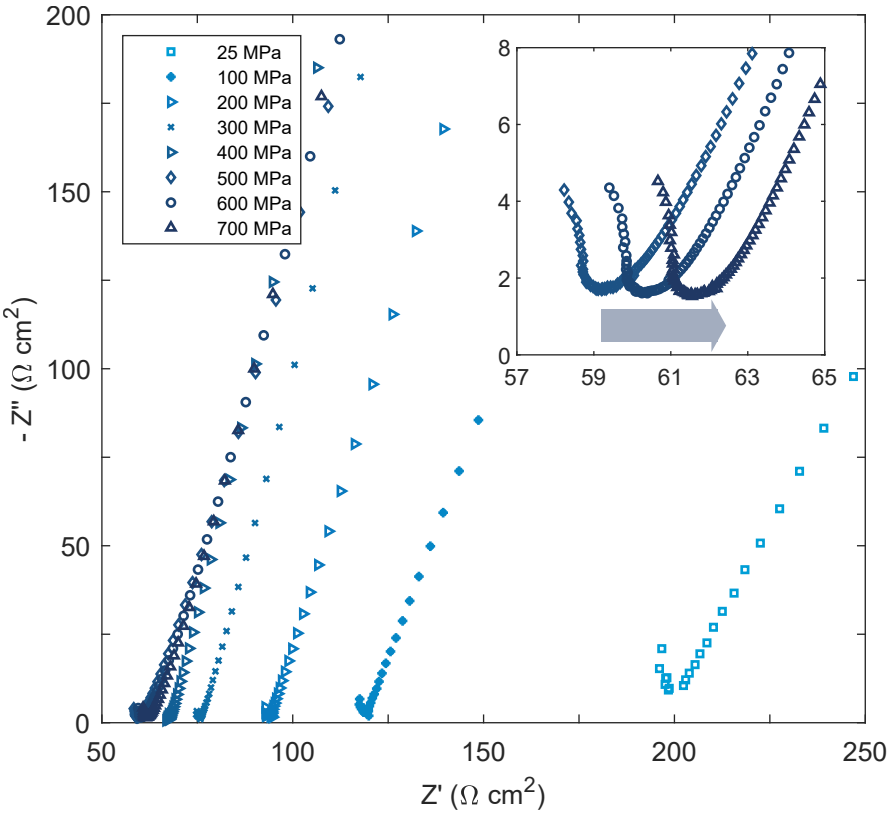


Fig. 4.7: Nyquist plots of LPSCl-SP at different pressures (all at RT) as a function of pressure up to 700 MPa. The arrow in the inset emphasizes that the resistance slightly increased after 500 MPa.

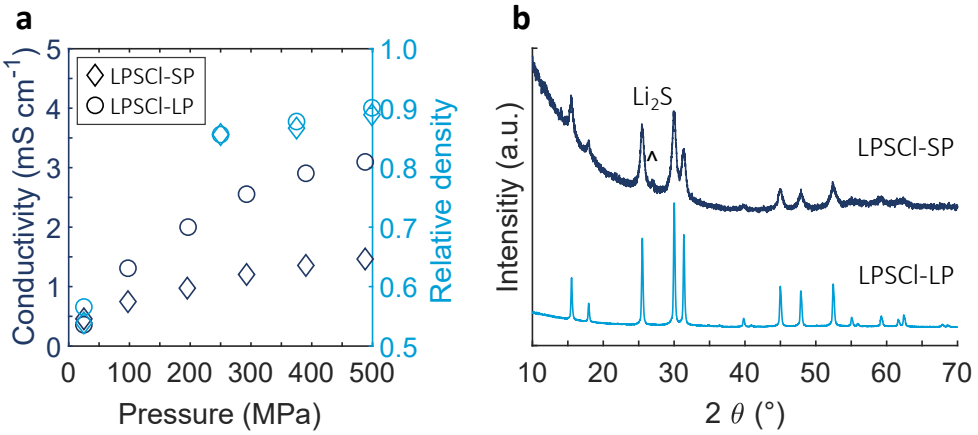


Fig. 4.8: (a) Ionic conductivity of LPSCl powders as a function of pressure, and (b) XRD spectra of the LPSCl powders.

excessive LPSCl particle cracking. Fig. 4.8a shows the ionic conductivity with relative density and stack pressure, for both SP and LP, up to 500 MPa, reaching 1.2 and 3 mS cm^{-1}, respectively. The lower conductivity of LPSCl-SP may be explained by some unreacted Li_2S suggested in the XRD spectra in Fig. 4.8b. Both powders predominantly comprised the argyrodite phase. Carbon black (Super C65, 2.5 wt%) was used in all the cathodes as an electron conductivity aid.

Cells were assembled according to the steps shown schematically in Fig. 4.9a. Active material, LPSCl-SP, and carbon black were mixed in a ball mill and subsequently pressed in a polymer mould at 500 MPa and RT with LPSCl-LP to form a pellet with further details provided in chapter 3.1. The SEM cross-section image in Fig. 4.9b shows that the composite cathode exhibited no signs of SC-NMC particle fracture, despite the high loads used during mixing and pressing. Moreover,

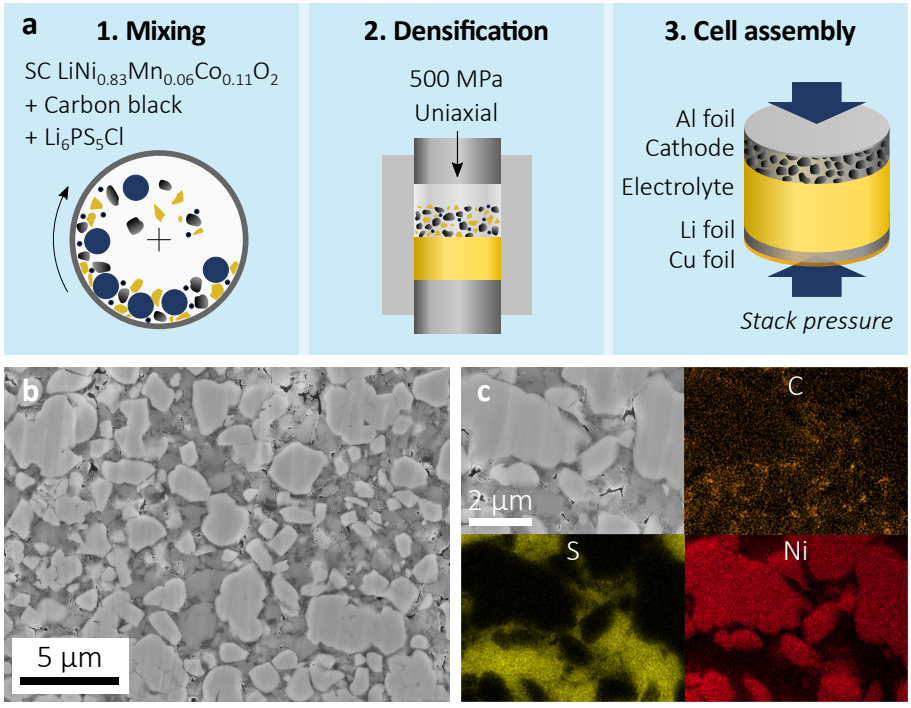


Fig. 4.9: (a) Schematic of the cell manufacturing steps, (b) cross-section of a SC-NMC/LPSCl composite cathode after cell assembly and before cycling, and (c) EDX element maps for C, S, and Ni.

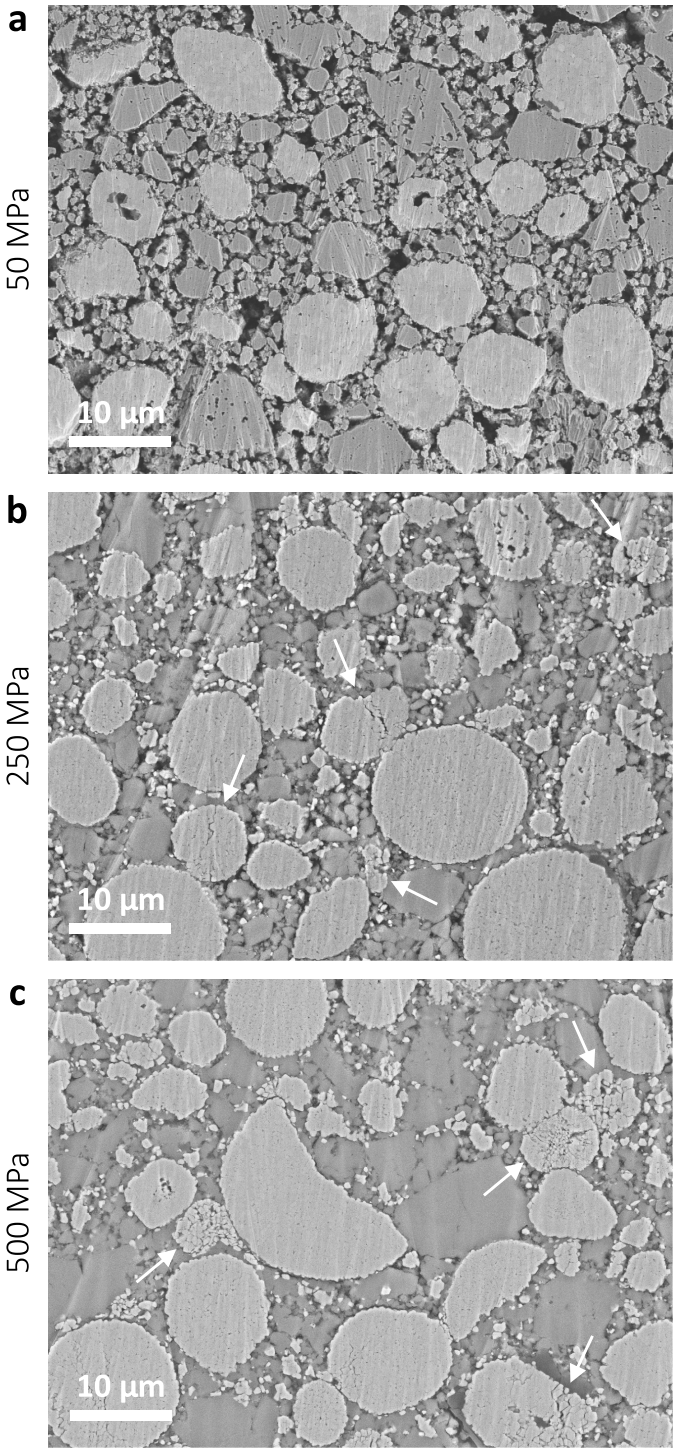


Fig. 4.10: PC-NMC/LPSCl cathodes densified at different fabrication pressures. Particle fracture is indicated by the white arrows. Fabrication pressures and estimated relative densities were: (a) 50 MPa, 78% (b) 250 MPa, 82% (c) 500 MPa, 86%.

there was continuous, intimate contact at the SC-NMC/LPSCl interfaces and an overall relative density of >90%. Corresponding EDX element maps (Fig. 4.9c) suggested an acceptable, typical distribution of carbon black to support electron percolation.

In contrast, densification of the similar PC-NMC/LPSCl mixture at the same pressure led to primary particle fracture along grain and/or agglomerate boundaries as shown in Fig. 4.10, with active fragments disconnected from one another and/or the LPSCl; the cracking persisted even when the fabrication pressure was lowered to 250 MPa, and only at 50 MPa was secondary particle integrity maintained. However, these lower pressures significantly increased porosity (from ∼14% to ∼22%, Fig. 4.10) and were markedly less effective in promoting NMC/LPSCl interfacial contact.

The different relative particle sizes of PC-NMC and SC-NMC affected the way they interacted with the LPSCl-SP during consolidation. As shown in Fig. 4.11 relatively small LPSCl particles will tend to sit in the interstices between larger PC-NMC particles. On application of pressure, there is movement of the hard PC-NMC particles and shear forces are transmitted to the more easily deformed LPSCl. The movement and shearing of the softer LPSCl over the harder NMC surface promotes the required intimate interfacial contact. However, once the PC-NMC particles contact one another, relative motion is inhibited and it is difficult to induce any further shearing of the LPSCl, and the PC agglomerates may start to crack. For the smaller SC-NMC, where the particle diameters are more similar to LPSCl, greater relative motion and shear deformation of the LPSCl is allowed before SC-NMC hard particle contact. Consequently, the extent and quality of interfacial coverage of LPSCl over the available SC-NMC surface is increased.

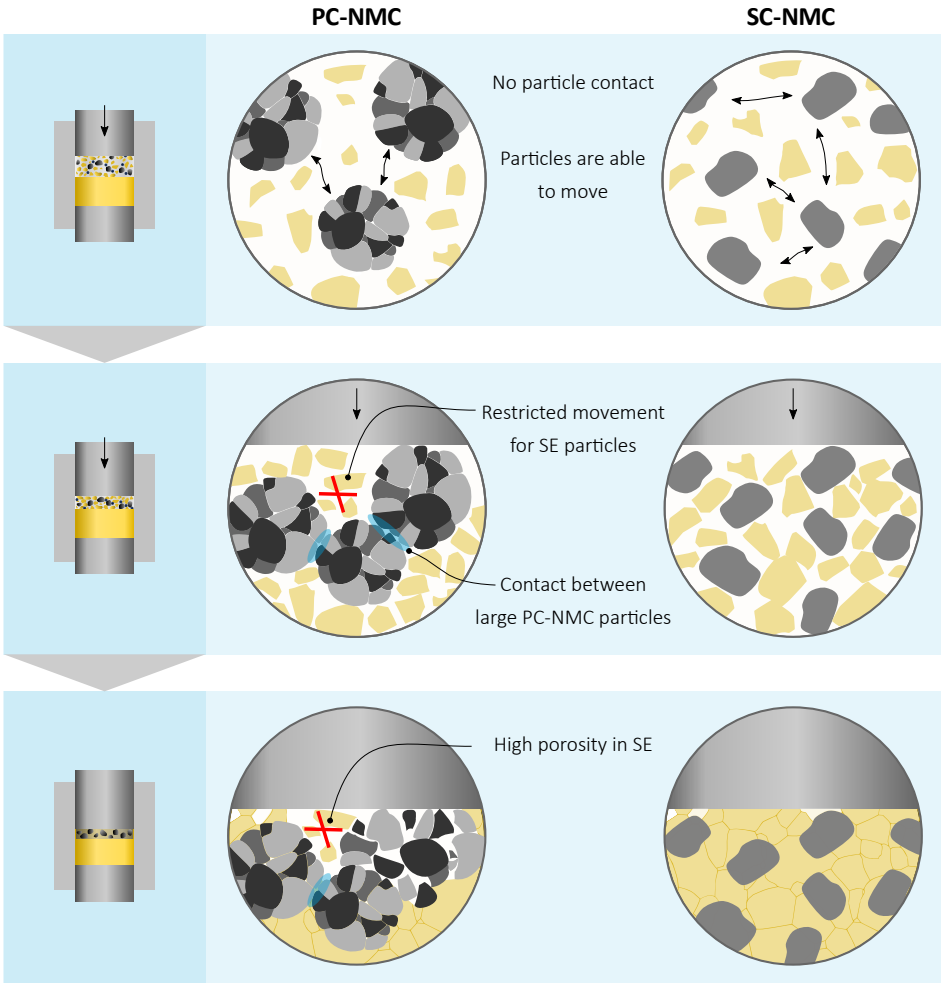


Fig. 4.11: Schematic comparison between polycrystalline (PC-NMC, grey/black agglomerates) and single-crystalline (SC-NMC, grey particles) cathode particles and solid-state electrolyte (SE, yellow) interactions during densification.

4.2.2 Microstructure after initial cycle

Cell assembly was completed by adding a Li foil and a Cu current collector on the anode side and an Al current collector on the cathode side.

A cell stack pressure during cycling is recommended to inhibit void formation at the anode/electrolyte interface during Li plating and stripping [22]. Therefore cells were cycled in the custom-made cell shown in Fig. 3.3 with a uniaxial pressure set by a torque wrench, calibrated to the stack pressure using a load cell (Fig. 3.4). A

low stack pressure of 2.5 MPa was chosen to study the electro-chemo-mechanical effects of the SC-NMC/LPSCl and PC-NMC/LPSCl cathodes during the first charge/discharge cycle. Very low stack pressures e.g. 1 MPa at the anode tend to favour Li void formation and a high overpotential (at reasonable current densities of 0.2 mA cm^{-2}); on the other hand, significantly higher pressures may promote particulate cracking and become impractical for larger scale cells or packs [139].

Fig. 4.12a shows the electrochemical performance of a SC-NMC/LPSCl composite cathode (14 mg cm^{-2}, 3 mA h cm^{-2} areal capacity) during the first charge and

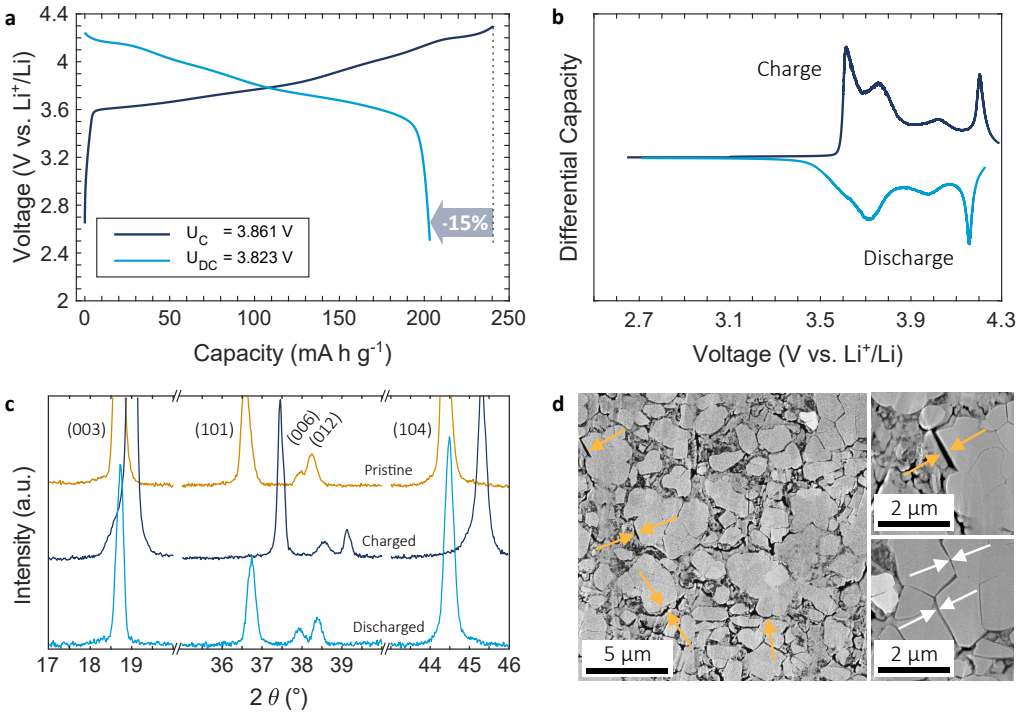


Fig. 4.12: (a) Initial charge/discharge curves (with average voltages U_C and U_{DC}) of a SC-NMC/LPSCl composite cathode (14 mg cm^{-2}, 3 mA h cm^{-2}) cycled at 2.5 MPa, 0.2 mA cm^{-2}, 30 °C and (b) the differential capacity. (c) Ex-situ XRD spectra before cycling, after charge and discharge. (d) Cathode cross-section after charging with some loss of contact at the SC-NMC/LPSCl interface and particle separation of previously agglomerated crystals.

discharge cycle at 2.5 MPa, 0.2 mA cm^{-2} and 30 °C. There was a high first cycle CE of 85% and a discharge capacity of 204 mA h g^{-1}. The slope at the beginning of the charge (<3.6 V) was attributed to carbon/LPSCl redox activity that undermined first cycle CE, forming thermodynamically more stable decomposition products such as P_2S_x, LiCl and S that then act as a passivation layer over subsequent cycles [140–143]; cells showed CE >99% on the second and subsequent cycle.

Corresponding differential capacity curves in Fig. 4.12b showed characteristic redox peaks previously observed for high-Ni NMC in LIBs, which indicated multiphase structural transitions [144]. A sharp peak at ∼4.2 V, rarely observed in lower Ni NMC materials, but typical at relatively high Ni contents, related to the appearance of the H3 phase and a more marked volume change [136]. From ex-situ XRD before cycling, after charge, and after discharge (Fig. 4.12c) the lattice volumes before and after charging were estimated at 101.62 $Å^3$ and 96.08 $Å^3$, respectively, corresponding to a nearly reversible volume shrinkage of 5.5% and consistent with the literature [136].

Corresponding cross-section SEM images after charging in Fig. 4.12d showed instances of contact loss at the SC-NMC/LPSCl interface (orange arrows) and particle separation of previously agglomerated crystals (white arrows) due to anisotropic volume change. There was no fracture of non-agglomerated SC-NMC particles.

For comparison, PC-NMC/LPSCl cathodes shown in Fig. 4.13a had a first discharge capacity of only 152 mA h g^{-1} and a first cycle CE of ∼70% under the same cycling conditions. The PC-NMC/LPSCl cathodes also had a higher overpotential due to their higher microstructural heterogeneity and defect density. As observed for SC-NMC, the PC-NMC/LPSCl cathodes in Fig. 4.13b after the first charge showed a similar interfacial contact loss and intergranular cracks. There was a notable tendency for larger diameter primary particles to undergo intergranular

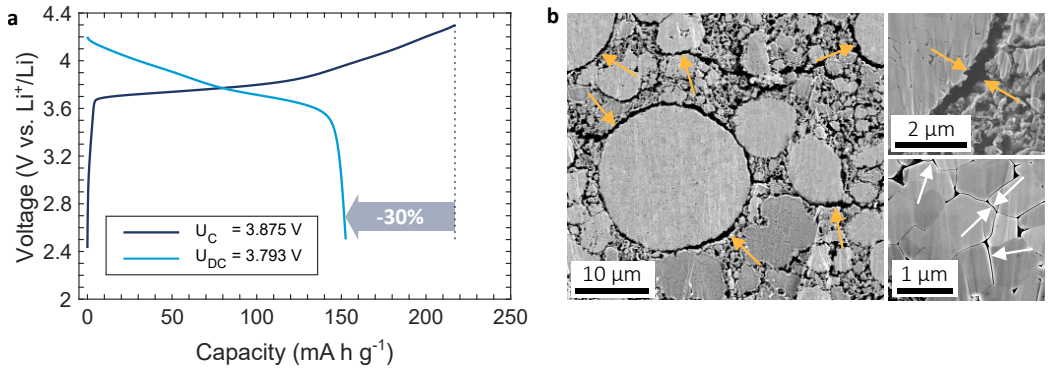


Fig. 4.13: (a) Initial charge/discharge curves of a PC-NMC/LPSCl cathode with a loading of 14 mg cm^{-2} (2.2 mA h cm^{-2}) and a Li anode cycled at 2.5 MPa, 0.2 mA cm^{-2}, 30 °C. (b) Cross-section of a PC-NMC/LPSCl composite cathode after charge.

cracking and dis-aggregation of secondary particles because of their more restricted ability to accommodate cycling strains without debonding [145].

Further, the interfacial impedance of the SC-NMC cell was compared with the PC-NMC cell in Fig. 4.14 using EIS. The interfacial impedance of the SC-NMC cell (∼40 Ω cm^2) was about half that of its PC-NMC counterpart, and was amongst

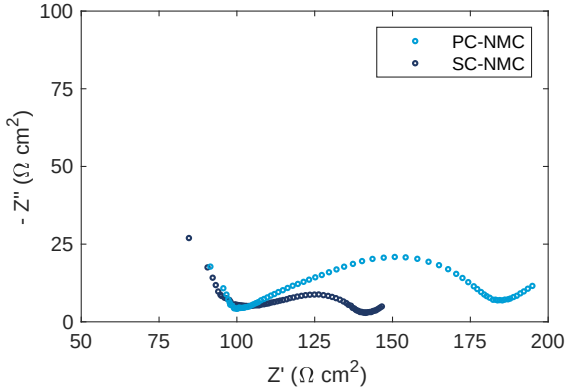


Fig. 4.14: Comparison of the interfacial resistance for composite cathodes based on PC-NMC/LPSCl and SC-NMC/LPSCl. Measurements were taken after the cells were charged to 4.3 V (10 MPa, 30 °C).

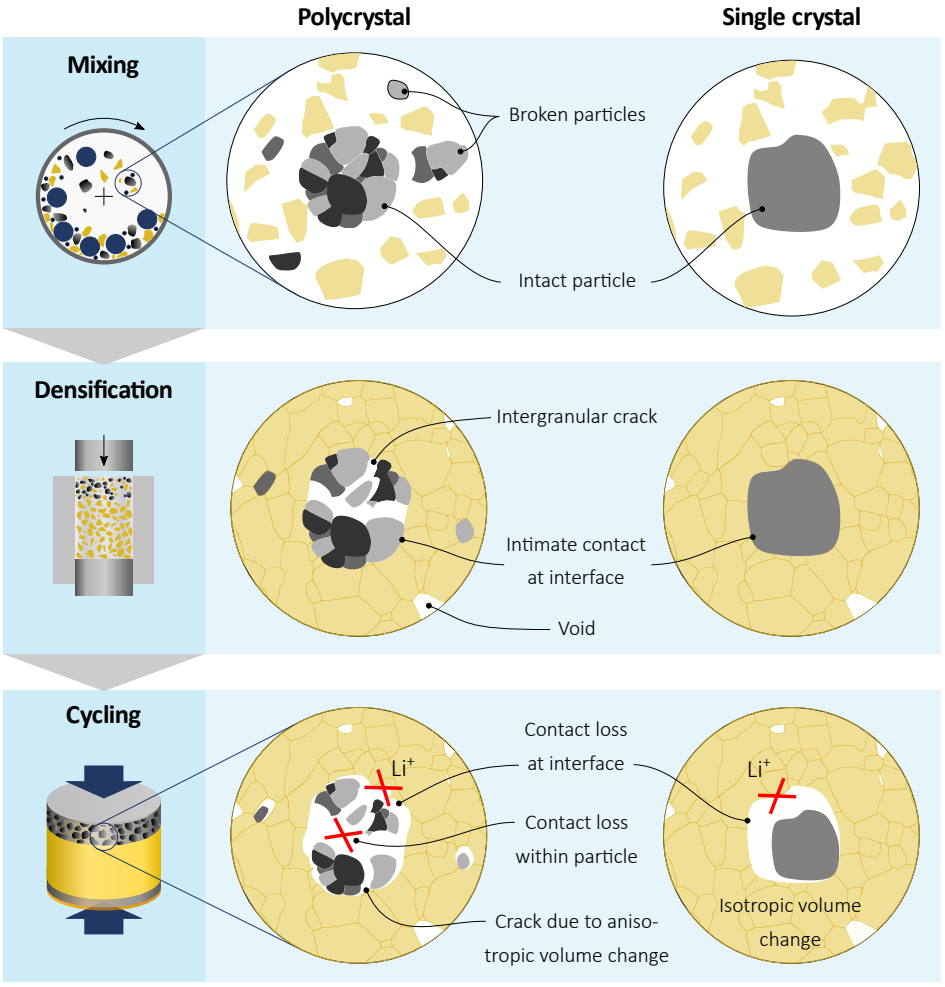


Fig. 4.15: Schematic comparison between polycrystalline (PC-NMC) and single-crystalline (SC-NMC) composite cathode particles during manufacturing and cycling.

the lowest reported for cells using a RT-pressed sulfide/NMC cathode and a Li anode. This might explain the lower overpotential of the SC-NMC cell.

Based on the qualitative insights described above, Fig. 4.15 shows a schematic depiction of the different changes in microstructure for SC-NMC- and PC-NMC-based composite cathodes during manufacturing and then cycling.

4.2.3 Impact of stack pressure during cycling

To study the effect of the intrinsic volume changes of the NMC and any interfacial contact loss with the SE during cycling, the cyclability of the SC-NMC/LPSCl

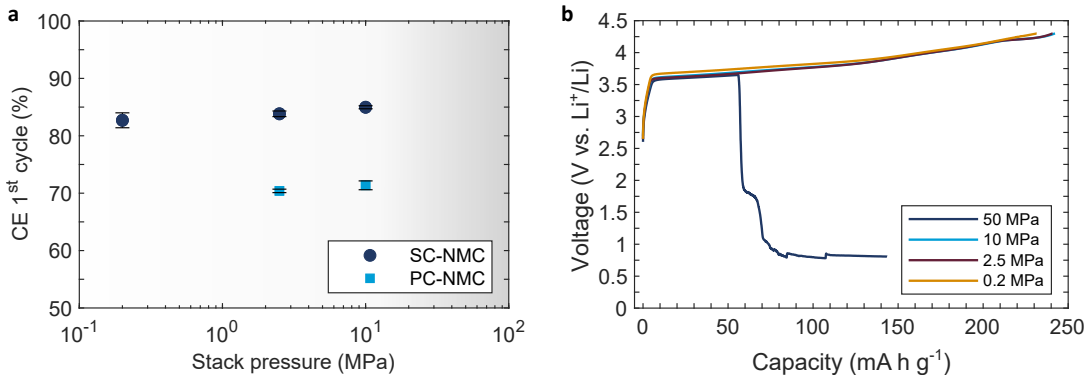


Fig. 4.16: (a) First cycle coulombic efficiency (CE) of a SC-NMC/LPSCl composite cathode obtained at different stack pressures. (b) Comparison of charge curves of SC-NMC/LPSCl composite cathodes cycled at different stack pressures. The cell at 0.2 MPa was cycled at an asymmetric pressure with 2.5 MPa at the anode.

cathodes was investigated at different stack pressures (50, 10, 2.5, and 0.2 MPa). Fig. 4.16a compares the first cycle CE at different stack pressures. At 50 MPa, there was cell failure on the first charge (Fig. 4.16b) with a qualitatively similar charging curve to that shown by Doux et al. at a stack pressure of 25 MPa, which was ascribed to accelerated Li penetration across the SE separator [146, 147]. Cells at lower pressures of 10 MPa and 2.5 MPa showed an almost identical first cycle CE of ∼85% and then failed at higher cycles (∼10) presumably via a similar mechanism.

Fig. 4.17a–b shows in detail the charge and discharge curves of the first 10 cycles of 14 mg cm^{-2} SC-NMC/LPSCl composite cathodes at 0.2 mA cm^{-2} and at stack pressures of 2.5 and 10 MPa, respectively. The initial discharge capacities were 204 and 205 mA h g^{-1} and, as shown in the inset graphs, the capacity retention after 10 cycles was 99.4% and 101.1% (>100% was possible because the current density was lowered to 0.1 mA cm^{-2} after 5 cycles) for 2.5 and 10 MPa, respectively. At the lower pressure of 2.5 MPa, progressive NMC/LPSCl contact losses were more likely to occur on each cycle. However, at 10 MPa, even after 10 cycles,

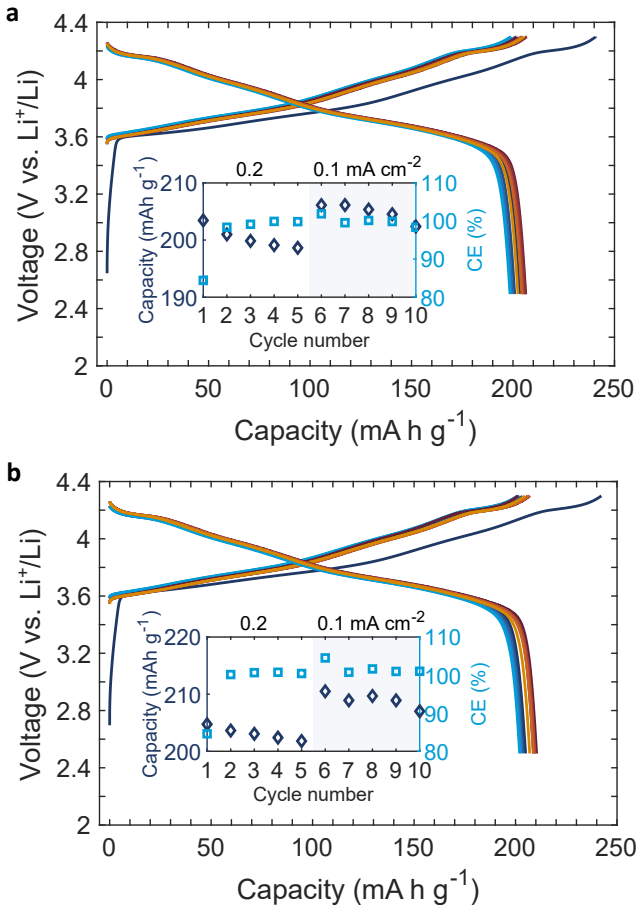


Fig. 4.17: Charge/discharge curves of a SC-NMC/LPSCl composite cathode (14 mg cm^{-2}, 3 mA h cm^{-2}) with a Li anode, and capacity fade (inset) at (a) 2.5 MPa and (b) 10 MPa.

cells had a high discharge capacity (∼210 mA h g^{-1}), which is amongst the highest reported for RT-pressed NMC/sulfide cathodes in SSBs. The sensitivity of capacity after 5 cycles to current density indicated that electrochemical processes were time dependent and that further optimization will be required to enable faster charging/discharging, for example, further optimization of the cathode microstructure or an electrolyte with higher intrinsic ionic conductivity [50].

To explore even higher cycle numbers for the SC-NMC/LPSCl cathode the Li anode was replaced with a $Li_4Ti_5O_{12}$ (LTO)/LPSCl composite anode to avoid the problem of Li penetration and premature failure; LTO also benefits from a relatively small

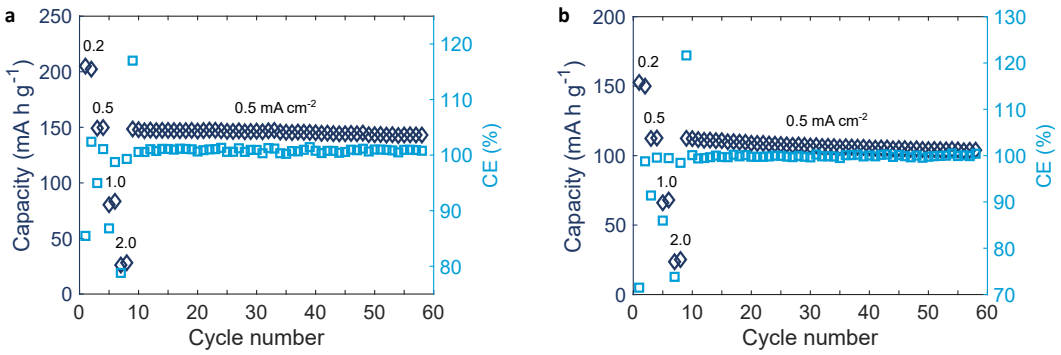


Fig. 4.18: Discharge capacity at different current densities and higher cycle numbers of a cathode (14 mg cm^{-2}, 3 mA h cm^{-2}) comprising (a) SC-NMC and (b) PC-NMC and a LTO/LPSCl composite anode cycled at 10 MPa.

volume change (0.2%) on charge/discharge [66]. In this arrangement, Fig. 4.18a shows that the same SC-NMC/LPSCl cathodes had a capacity retention of 96.3% after 50 cycles (between cycle number 9 and 58). Fig. 4.18b shows that the PC-NMC/LPSCl cathodes again had lower discharge capacities that decayed faster (92.4% after 50 cycles), due to their higher defect density and accelerated particle pulverization [135].

To explore further the effects of a low stack pressure at the cathode, a new asymmetric pressure design as shown schematically in Fig. 4.19a was implemented. Whereas a compression spring (Fig. 3.5b and Table 3.1) was used to apply 0.2 MPa at the cathode, the pressure on the anode was maintained at 2.5 MPa using a calibrated uniaxial load. Pressure asymmetry was possible because of the high friction coefficient and contact area between the SE pellet and the mould wall. Cathode and anode pressures were confirmed experimentally using a load cell and computationally by finite element method (FEM) calculations. The results shown in Fig. 4.20 suggest that under reasonable friction assumptions, when the anode was loaded to 2.5 MPa, there was negligible pressure transmission to the cathode. Fig. 4.16a shows that cells cycled at a cathode pressure as low as 0.2 MPa only had

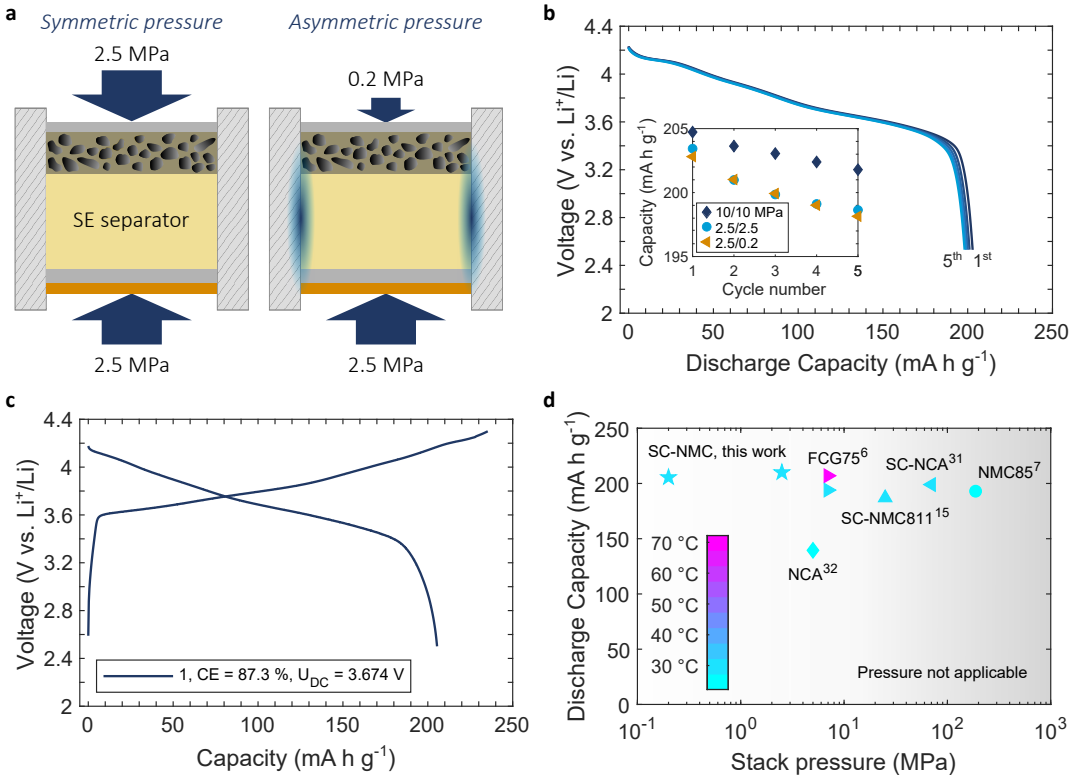


Fig. 4.19: (a) Asymmetric load cell set-up used to lower the cathode stack pressure while maintaining anode pressure. Corresponding voltage capacity curves for a cell cycled at 0.2 mA cm^{-2} and an anode/cathode pressure of 2.5 MPa/0.2 MPa for (b) a SC-NMC/LPSCl composite cathode of 14 mg cm^{-2} (3 mA h cm^{-2}), and capacity fade compared to different pressures and (c) a SC-NMC/LPSCl composite cathode of 43 mg cm^{-2} (8.7 mA h cm^{-2}). (d) Discharge capacity comparison for Ni-rich composite cathodes pressed at RT as a function of the stack pressure during cycling.

a slightly reduced first cycle CE of ∼83% compared with those at higher pressure. The first 5 discharge cycles at 2.5 MPa/0.2 MPa are shown in Fig. 4.19b for a 14 mg cm^{-2} cathode at 0.2 mA cm^{-2}. The inset compares the discharge capacity at different pressure combinations. While the slowest decay in capacity was for a 10 MPa/10 MPa arrangement as previously suggested in Fig. 4.17b, the discharge

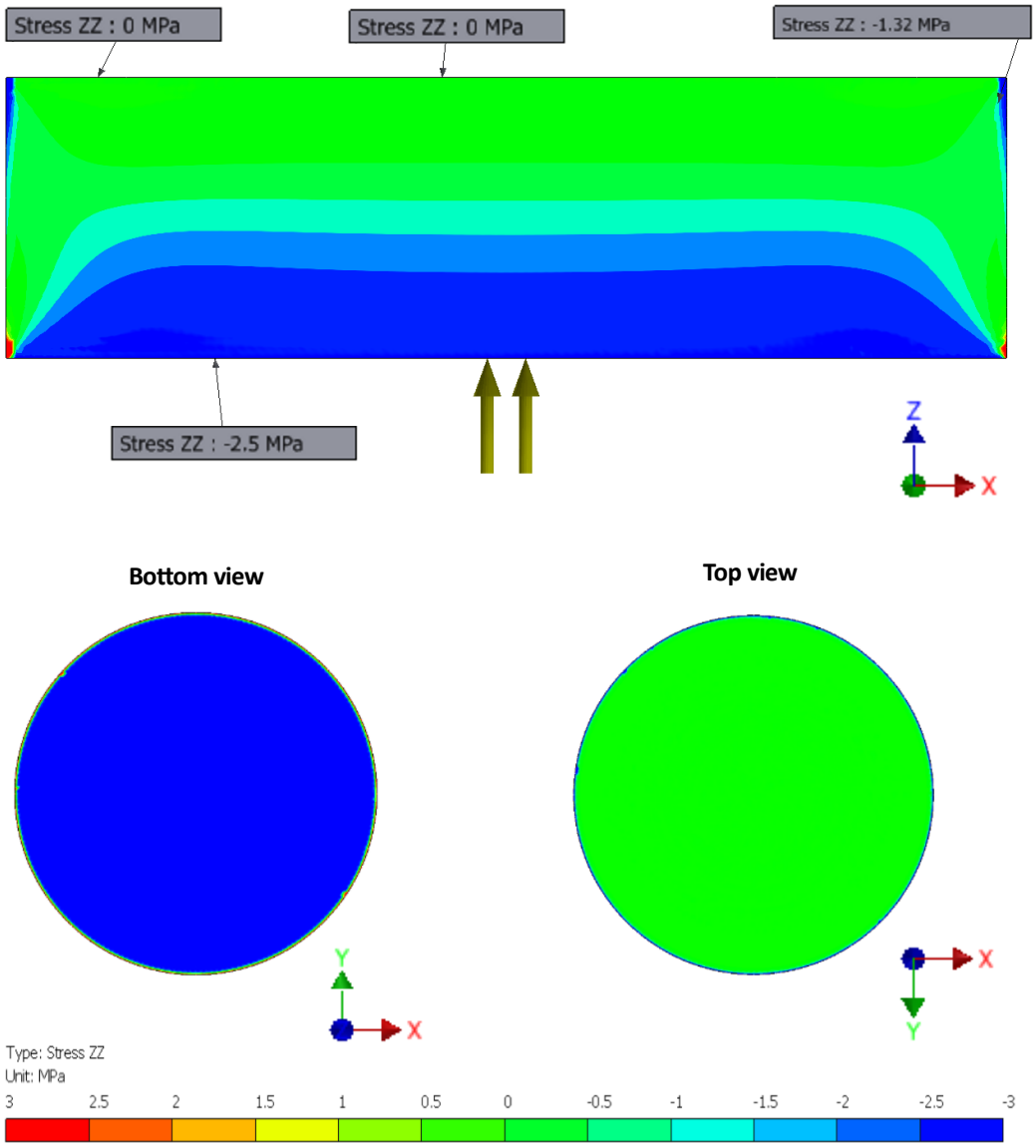


Fig. 4.20: Finite element analysis of the pellet with a one-sided (asymmetric) stack pressure applied showing negligible pressure (stress) transmitted from the anode to the cathode due to wall friction. The bottom represents the anode where a loading of 2.5 MPa was applied. The top view shows that there was negligible stress induced in the z direction in the cathode.

capacity of the first cycle and the capacity decay over the first five cycles was almost identical for 2.5 MPa/2.5 MPa and 2.5 MPa/0.2 MPa arrangements.

Cycling of a SC-NMC composite cathode with an increased, very high areal capacity of 8.7 mA h cm^{-2} (thickness ∼200 µm) was then demonstrated at a cathode pressure of 0.2 MPa in Fig. 4.19c, providing a discharge capacity of 205 mA h g^{-1} and a first cycle CE of 87%. To understand how this performance might scale towards a practical cell, a SE separator thickness reduced from 1.5 mm to 20 µm was assumed, including the mass/volume of the Li foil and current collectors, (see Table 4.3 for details) a cell based on this arrangement was estimated to provide a specific energy of 405 W h kg^{-1} and a volumetric energy density of 1069 W h L^{-1}.

Table 4.3: Parameters of the SC-NMC/LPSCl/Li cell with a high cathode loading used for energy density calculations. All values were those used/obtained experimentally except the separator thickness which was 1.5 mm in the actual experiment and assumed to be 20 µm in the calculations.

Cathode	NMC loading (mg cm^{-2})	42.42
	NMC ratio (wt%)	70
	LPSCl ratio (wt%)	27.5
	Carbon black ratio (wt%)	2.5
	Relative density	0.9
	Al current collector thickness (µm)	15
Anode	Li foil thickness (µm)	50
	Cu current collector thickness (µm)	10
Separator	Thickness (µm)	20
	Relative density	0.9
Cell	Discharge capacity (mA h g^{-1})	205.5
	Average discharge voltage (V)	3.674
	Cell diameter (mm)	5
Cycle conditions	Cathode stack pressure (MPa)	0.2
	Anode stack pressure (MPa)	2.5
	Current density (mA cm^{-2})	0.2

A comparison of discharge capacities obtained in this work with other RT-pressed cathodes as a function of applied stack pressures during cycling is shown in Fig. 4.19d [148, 149]. The results in this chapter suggest that by (i) choosing active and SE particle sizes and morphologies matched to their required function, (ii) the use of protective coatings, and (iii) optimizing mixing and consolidation parameters, high initial capacity and high efficiency can be achieved even at low stack pressures, including novel low-pressure asymmetric arrangements.

4.3 Conclusions

It was demonstrated that cold-pressed single crystal NMC/LPSCl cathodes can deliver high first cycle coulombic efficiencies >85% and discharge capacities >205 mA h g^{-1} even when cycled at room temperature and a low, practical external stack pressure 0.2 MPa and despite the relatively high volume expansion/contraction of the NMC. Critical to the performance was an optimized fabrication route that maximized NMC/LPSCl physical surface interaction and interfacial contact. Single crystal NMC particles showed greater robustness during mixing and densification in comparison with their polycrystalline NMC

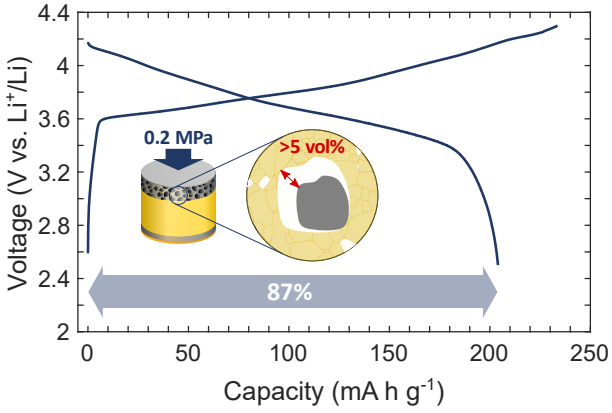


Fig. 4.21: Performance summary of a high-Ni single crystal/Li_6PS_5Cl-based cathode highlighting a large discharge capacity >205 mA h g^{-1} despite active material volume expansion of >5% and a low stack pressure of 0.2 MPa.

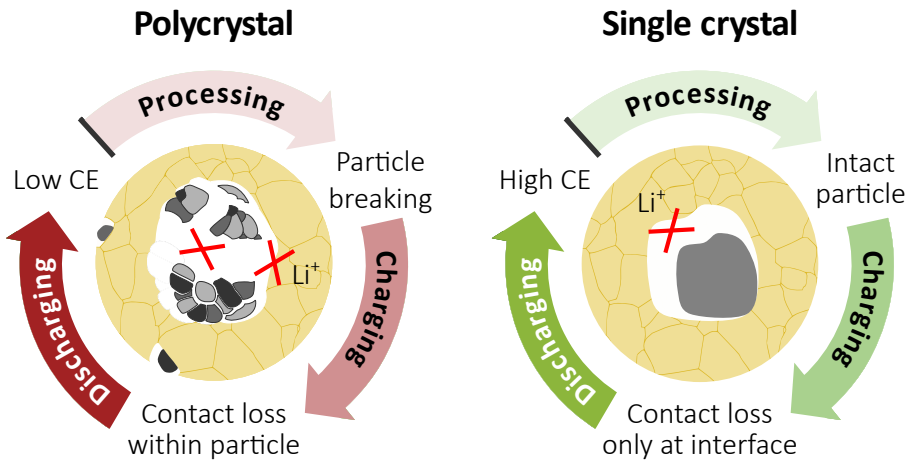


Fig. 4.22: Schematic comparison of polycrystalline and single crystal cathode active materials.

counterparts that suffered from intergranular cracks first during processing and then during cycling due to anisotropic volume expansion. The optimized single crystal NMC/LPSCl composite cathode microstructure facilitated a novel anode/cathode asymmetric pressure arrangement that allowed pressures as low as 2.5 MPa/0.2 MPa to be used successfully. Key results are also summarized graphically in Figs. 4.21–4.22.

4.4 Experimental details

Dynamic light scattering (DLS). The particle size distribution was measured at room temperature using DLS in a Horiba LA-960 analyser operating with a 650 nm red laser and a 450 nm blue light emitting diode (LED). The particles were first dispersed in deionized water using a bath sonicator for 1 min.

Electrode preparation. For the composite cathode, 70 wt% $LiNbO_3$-coated NMC, 27.5 wt% LPSCl-SP, and 2.5 wt% carbon black (Super C65) was mixed in a planetary ball mill with more details provided in chapter 3.1. $Li_4Ti_5O_{12}$ (LTO)/LPSCl anodes were prepared using the same mixing conditions comprising 60 wt% LTO, 35 wt% LPSCl, and 5 wt% carbon nanofibers.

Cell Assembly. Cells were assembled and cycled in a custom-designed device described in chapter 3.1.5. Stacked layers of 25 mg (50 mg for cells cycled at asymmetric pressure) of LPSCl-LP and then 4 mg (12 mg for the cell with a high loading in Fig. 4.19c) of the composite cathode mixture were pressed in a plastic mould. A Li foil of ∼30 µm thickness or 15 mg of the composite anode mixture was added to the stacked cell as anode.

Electrochemical measurements. Galvanostatic cycling was performed at 30 °C and a constant current (varying from 0.1 mA cm^{-2} to 2 mA cm^{-2}) between a cell voltage range 4.3–2.5 V and 2.8–1.0 V for Li and LTO based cells, respectively.

Electron backscatter diffraction (EBSD). Samples were prepared by coating NMC particles (1 g) dispersed in a polyvinylidene fluoride (PVDF)/N-Methyl-2-pyrrolidone (NMP) solution (50 mg/1 ml) onto an Al foil to obtain electrode sheets which were subsequently cross-sectioned by an automated Ar ion polishing system (PECS 2, Gatan). EBSD characterization was carried out in a Zeiss Merlin FEG-SEM system equipped with a Bruker e-flash high resolution EBSD detector. An accelerating voltage of 30 kV and a probe current of 10 nA was used to acquire Kikuchi patterns with resolution 400 × 300 at a step size of 50 nm. Data was expressed as band contrast (pattern quality) map and inverse pole figure. The lattice parameters of pristine materials shown in Table 4.1 were used for EBSD pattern indexing.

Finite Element Method (FEM) stress analysis. Geometries and calculations were implemented with Inventor software. It was assumed that the pellet was fixed at the outer surface due to its high friction with the plastic mould.

X-ray photoemission spectroscopy (XPS). XPS was conducted using a PHI VersaProbe III system generating monochromatic *Al* X-rays at 1486 eV. $LiNbO_3$-coated NMC powder was mounted on adhesive carbon tape inside a glovebox and

transferred into the XPS via a vacuum transfer vessel to avoid contamination and ambient exposure. Survey scans and high-resolution elemental scans were acquired at pass energies of 224 eV and 55 eV respectively. The powder was further etched using a monoatomic Ar^+ ion beam accelerated at 1 kV and rastered over a 3 $\times$ 3 mm^2 scan area for a total of 40 min, while profiling XPS spectra in 2 min (15 min) and 5 min (25 min) time intervals. The spectra were fitted to Gaussian-Lorentzian and Voigt lineshapes (where asymmetry was pronounced), and quantified using CasaXPS software.

Fast-charging all-solid-state battery cathodes with long cycle life

Many battery applications target fast charging that increase the state of charge (SOC) to at least 80% in <15 min. However, most all-solid-state cells take several hours to reach >80% SOC and a typical specific energy of 400 W h kg_{cell}^{-1}. This arises because of current density limitations at the anode and high interfacial resistances in the cathode, leading to high overpotentials even at elevated temperature. The fast-charging capability of a low resistance sulfide-based single crystal Li-Ni-Mn-Co oxide all-solid-state cathode is investigated using a 3-electrode arrangement that allows differentiation between anodic and cathodic contributions. At 30 °C and charging at 15 mA cm^{-2}, a specific capacity of 150 mA h g^{-1} in ∼8 min was achieved, with 80% capacity retention after 3000 cycles. There was a low void formation rate during cycling due to careful selection of materials, optimized cathode fabrication, and limits on the depth of charge/discharge. At 80 °C, a current density of 50 mA cm^{-2} charged a cathode areal capacity of 8 mA h cm^{-2} and 400 W h kg_{cell}^{-1} in only 10 min, suggesting practical all-solid-state battery cathodes for fast charging may be within reach.

5.1 Introduction

Solid-state batteries (SSBs) have the potential to be safer and have higher specific energy compared with conventional Li-ion batteries (LIBs) because they use an inorganic solid electrolyte (SE) instead of a flammable liquid electrolyte (LE) and Li metal instead of a graphite intercalation anode [13, 14, 150]. Sulfide SEs with a high

ionic conductivity beyond 1 mS cm^{-1} and favourable thermomechanical properties facilitate large-scale SSB manufacturing at room temperature, a major advantage over lower conductivity oxide SEs that require higher temperature processing [20, 30, 57, 126, 151, 152]. Although SSBs with high specific energy >400 W h kg_{cell}^{-1} at room temperature have been demonstrated, they suffer from long charging times (e.g. cycling at only C/10 to reach full charge after 10 h) deriving from a low current density <1 mA cm^{-2} required to avoid Li dendrite formation and short circuits. A high external uniaxial stack pressure (>5 MPa) is also usually required to maintain the integrity of SE-active material interfaces during cycling [128, 129, 153]. Even with these restrictions, SSB capacity nonetheless usually fades significantly during cycling and there is low (<70%) cathode active material (CAM) utilization [154]. Many practical applications require relatively short SSB charging times and therefore comparatively high charging current densities [155]. For the case of electric vehicles (EVs), miles of range per charging time relates directly to the charge current density, and a desirable EV battery charging time of <15 min (4C) at a practical cathode capacity of 3 mA h cm^{-2} requires a current density of >10 mA cm^{-2} [153, 156].

Unfortunately, current densities of this magnitude have scarcely been demonstrated, even at elevated temperature (e.g. 60 °C) [20, 26, 157], which is used to speed up otherwise relatively slow electrochemical reactions and ionic diffusion. For example, sulfide SE-based lithium cobalt oxide (LCO) 28 µm thick composite cathodes (CAM loading: 4.9 mg cm^{-2}) with a lithium titanium oxide (LTO) anode were charged and discharged at 12 mA cm^{-2} (18 C) at 100 °C [20]. More recently, a charge current density of 8.6 mA cm^{-2} (20 C) was explored for a lithium nickel cobalt oxide (NMC) and sulfide SE ∼7 µm ultra-thin cathode (CAM loading: 1.4 mg cm^{-2}). Even at 55 °C and >50 MPa stack pressure, the discharge capacity was restricted to ∼81 mA h g^{-1} [158]. A significantly thicker sulfide and again NMC-based cathode (100 µm, 30 mg cm^{-2}) with an anode-less design was cycled

successfully at 60 °C at a discharge current density up to 13.6 mA cm^{-2} and charge current density of 3.4 mA cm^{-2} (0.5 C) [26]. Most SSB designs are held back from higher charge current densities because of limitations arising at the anode such as high overpotential or Li dendrite formation.

Assuming a focus on cathode performance for an EV fast charge of <15 min, a relatively thick (>70 µm) electrode with a high CAM areal loading (>15 mg cm^{-2}) and a high cycle life (maximum 80% capacity fade over 1000 cycles) will typically be required [159–161]. To reach these targets, the composite CAM/SE cathode must not only be designed to have excellent ionic and electronic percolation but also comprise materials with slow degradation over many cycles. Both theoretical and experimental approaches have been conducted to find optimized particle sizes of the CAM and SE because the microstructure and arrangement of these constituents strongly affected performance [48, 49, 162]. Non-optimized architectures with, for instance, high tortuosity or high as-manufactured pore volume should be avoided [50, 163]. In terms of cathode cycle life, single crystal (SC) CAM particles have a lower rate of mechanical degradation (pulverization and de-agglomeration) than their polycrystalline counterparts [148, 164]. Combining requirements for a fast-charging composite cathode with long cycle life the following characteristics are specified [48, 142, 165]: (i) Single crystal instead of polycrystalline CAM, (ii) small (<5 µm) CAM particles, (iii) low (<3%) volume expansion of the CAM during cycling, (iv) carbon nanofibers (CNF) instead of carbon black (CB) for electronic percolation at low fraction, (v) small (<1 µm) SE particles to pack around the CAM particles, (vi) high intrinsic ionic conductivity of the SE (>1 mS cm^{-1}), (vii) homogenous mixing of cathode components, (viii) low (<10%) as-manufactured pore volume, and (ix) intact, crack-free CAM particles after densification and before cycling.

Here, a composite cathode conforming to the above design specification is investigated using a three-electrode arrangement that allows the cathode performance to be disentangled from restrictions due to the anode. It is demonstrated that fast charging times <10 min can be achieved in an argyrodite electrolyte-based NMC composite cathode at 15 mA cm^{-2} and 30 °C with a high discharge capacity of 150 mA h g^{-1} (CAM utilization of 71%). Capacity retention after 3000 cycles was 81% with voided volume in the composite cathode increasing from 3% to 6.9% after 1000 cycles. At 80 °C the discharge capacity increased to 190 mA h g^{-1} after only 10 min charging at 50 mA cm^{-2} and with an areal capacity of 8 mA h cm^{-2}. The cell performance demonstrates that fast charging can be realized in designed SSB cathodes close to room temperature. Where applications allow asymmetric charge/discharge times, the composite cathodes could make a valuable contribution to SSBs with practical charge times and cycle lives.

5.2 Results and discussion

5.2.1 Fast-charging rate performance at 30 °C

The design and performance of a fast-charging cathode following the design criteria (i-ix) above is described in this section. The cathode architecture comprised a composite of single crystal $LiNi_{0.83}Mn_{0.06}Co_{0.11}O_2$ (NMC, $d_{50} \sim 3$ µm) as the CAM particles, a percolating network of Li_6PS_5Cl (LPSCl, $d_{50} \sim 1$ µm) SE, and carbon nanofibers (CNFs) as shown schematically in Fig. 5.1. NMC with 83% Ni has an approximate volume change of only 3% for a SOC cycling in the range 10–80%, which nonetheless provides a relatively high capacity of >150 mA h g^{-1}. Cycling between 0–100% SOC will give more capacity (∼210 mA h g^{-1}) but at the price of a more pulverizing volume change of approximately 6%. To promote uniform ionic and electric percolation with a low interface resistance between the solid phases we used LPSCl SE with a high intrinsic ionic conductivity of 2.5 mS cm^{-1} at 30 °C, mixed with the CAM and the CNFs in a planetary ball mill. 3-electrode

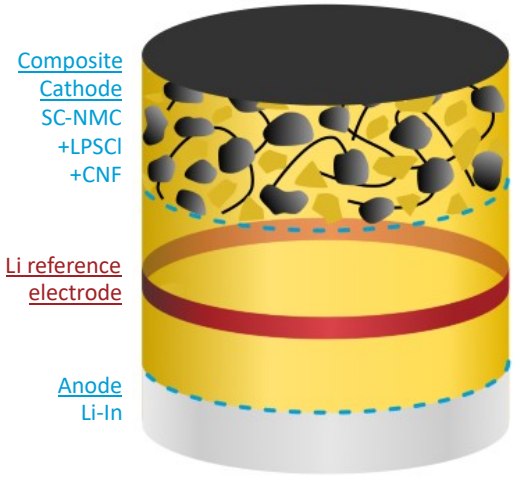


Fig. 5.1: Schematic of the 3-electrode cell set-up used to investigate rate performance.

cells according to Fig. 5.1 were then manufactured in an insulating plastic mould by cold pressing stacked layers of sulfide SE to form the separator, the ball-milled composite powder to form the cathode, and a Li-In alloy to form the anode, each at a uniaxial pressure of 500 MPa. The plastic moulds for the 3-electrode cells and cells for microstructure analysis after cycling are shown in Fig. 3.6 in chapter 3.1.5 with experimental details on the cell set-up and assembly. The cross-sectional scanning electron microscope (SEM) image and energy-dispersive X-ray spectroscopy (EDX) mapping of a typical cathode in Fig. 5.2 show the desired near-uniform distribution and high density of the constituents with non-fractured CAM particles.

Cells were cycled as it is commonly done in the plastic mould that allows a uniaxial stack pressure to be applied. However, to reduce the stack pressure as much as possible and towards practical levels, an asymmetric load that was much lower than typically used was applied during cycling. This arrangement is possible due to the high friction between the relatively thick (>1 mm) SSB pellet and the mould side wall. The external stack pressure at the cathode was set as 0.2 MPa and 10 MPa at the anode as shown in Fig. 5.3a [164]. Finite element

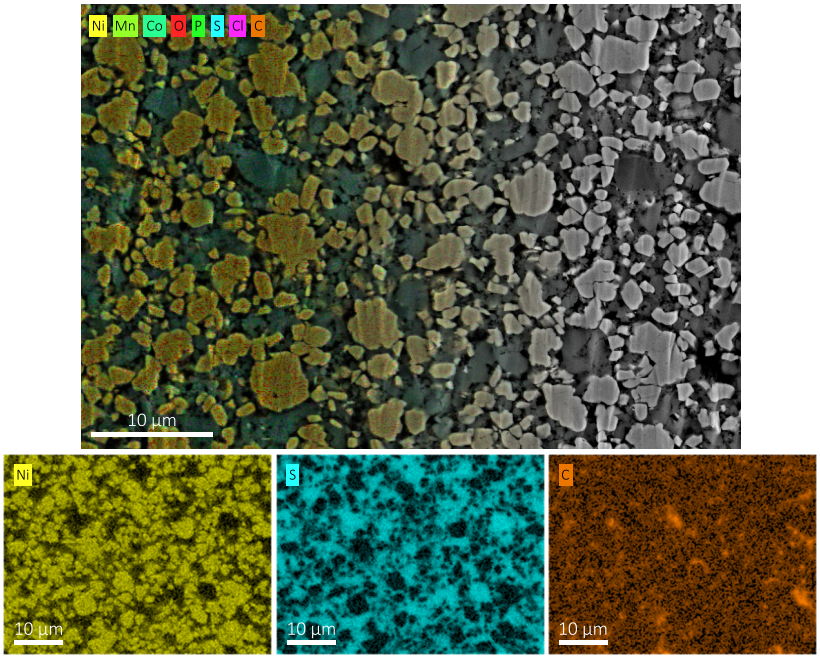


Fig. 5.2: SEM image and corresponding EDX maps of a cross-sectioned NMC/LPSCl/CNF composite cathode before cycling.

stress calculations shown in Fig. 5.3b-e suggest that under these external loads, axial stress on the cathode was below 1 MPa. Some residual compression may also be present due to the elastic deformation of the mould during the operations. However, given the ready deformation of the sulfide SE it is likely any significant residual strains will be relieved by flow/creep of the LPSCl.

Fig. 5.4a shows the discharge capacity resulting from a rate test at 30 °C as the charge current density increased from 1 to 15 mA cm^{-2} incrementally, every five cycles during charge. For all cases, the discharge current density was kept constant at 1 mA cm^{-2}. The discharge capacity decreased from 196 to 150 mA h g^{-1} as the charge current density was increased from 1 to 15 mA cm^{-2} i.e. from 3 h to 8 min. This indicated a capacity retention of 76%, and a high CAM utilization of 71% at 30 °C (assuming a theoretical capacity of 210 mA h g^{-1}). After 25 cycles the charge current density was reduced back to 1 mA cm^{-2}, and the initial capacity was almost fully retrieved, with little irreversible capacity loss. Fig. 5.4b shows the

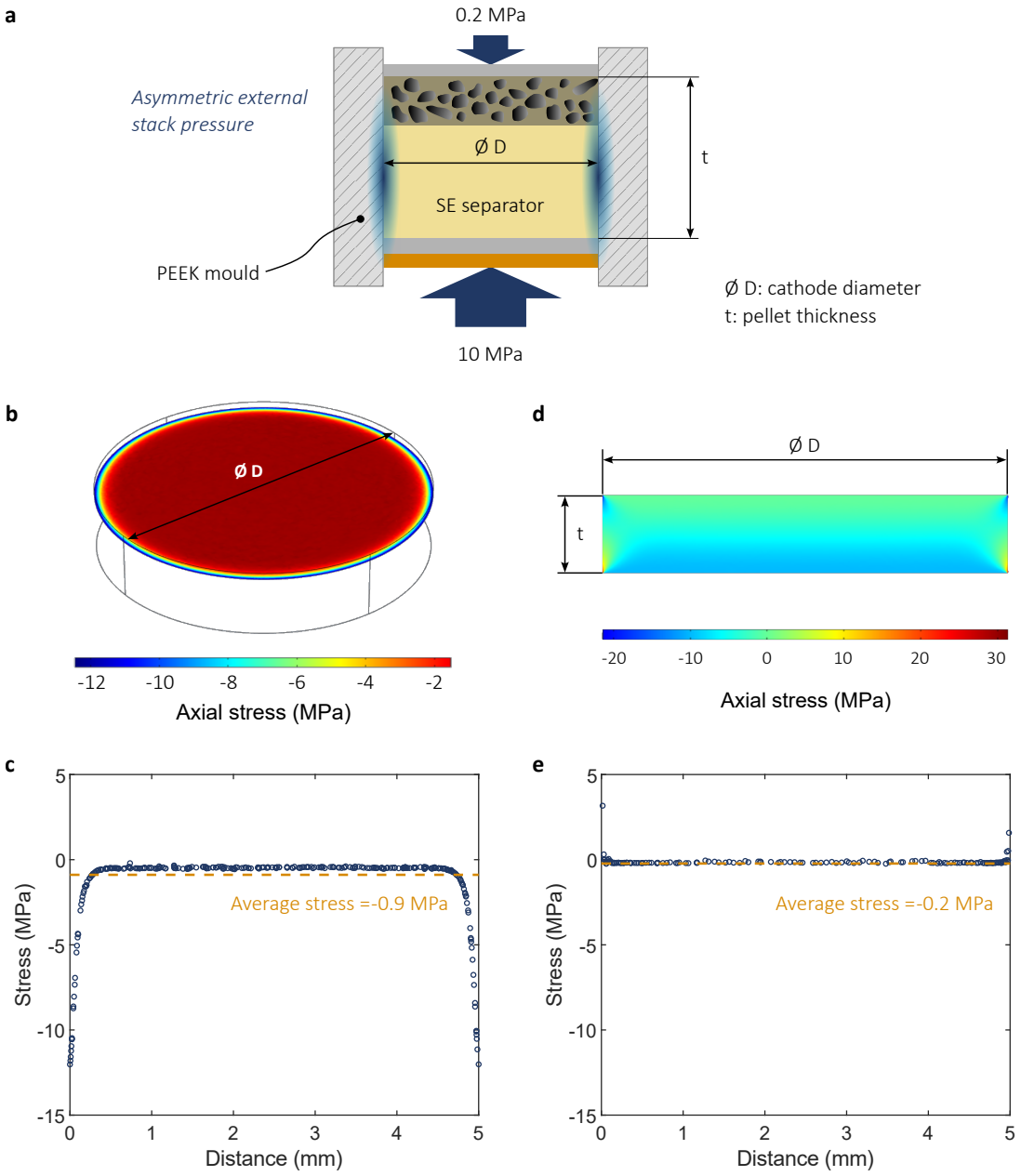


Fig. 5.3: (a) Applied asymmetric stack pressure on the pellet cell inside a PEEK mould. Stress in axial direction at (b-c) the separator/cathode interface, (d) the cell cross-section, and (e) the cathode/current collector interface.

corresponding voltage between the cathode and the Li reference electrode versus the capacity during the rate test. Fig. 5.5a–b shows that, as is typical, when the discharge current density was also increased, there was a further reduction in discharge capacity. The coulombic efficiency in the first cycle depended on

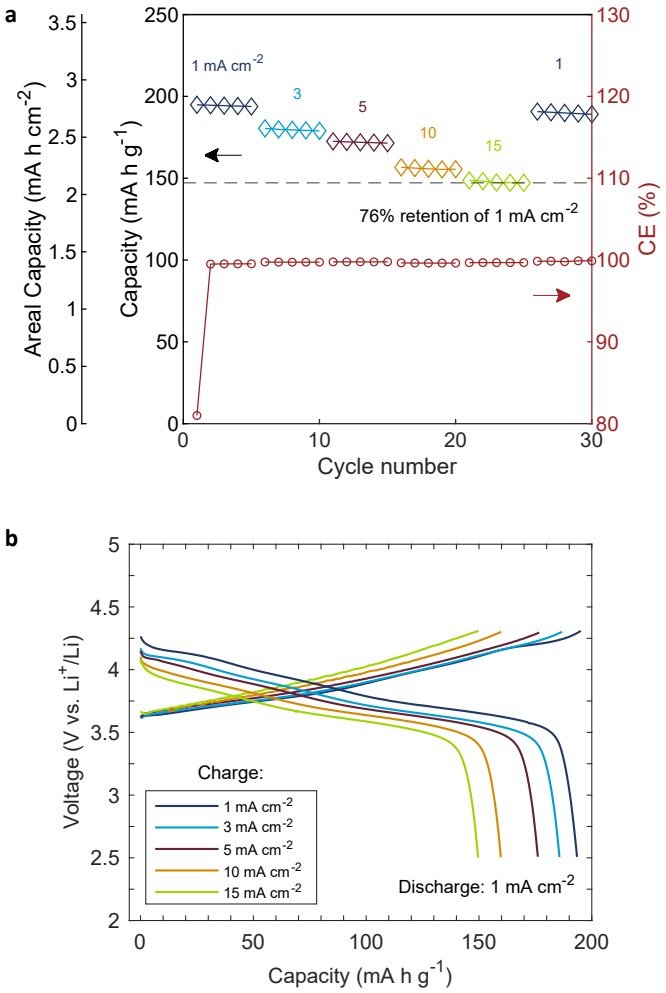


Fig. 5.4: (a) Discharge capacity of a rate performance test at different charge current densities up to 15 mA cm^{-2} at 30 °C. The discharge current density was kept constant at 1 mA cm^{-2}. (b) Corresponding charge/discharge curves. The average charge/discharge voltages were 3.915 V/3.812 V, 3.910 V/3.752 V, 3.917 V/3.731 V, 3.925 V/3.692 V, 3.939 V/3.651 V with increasing charge current density.

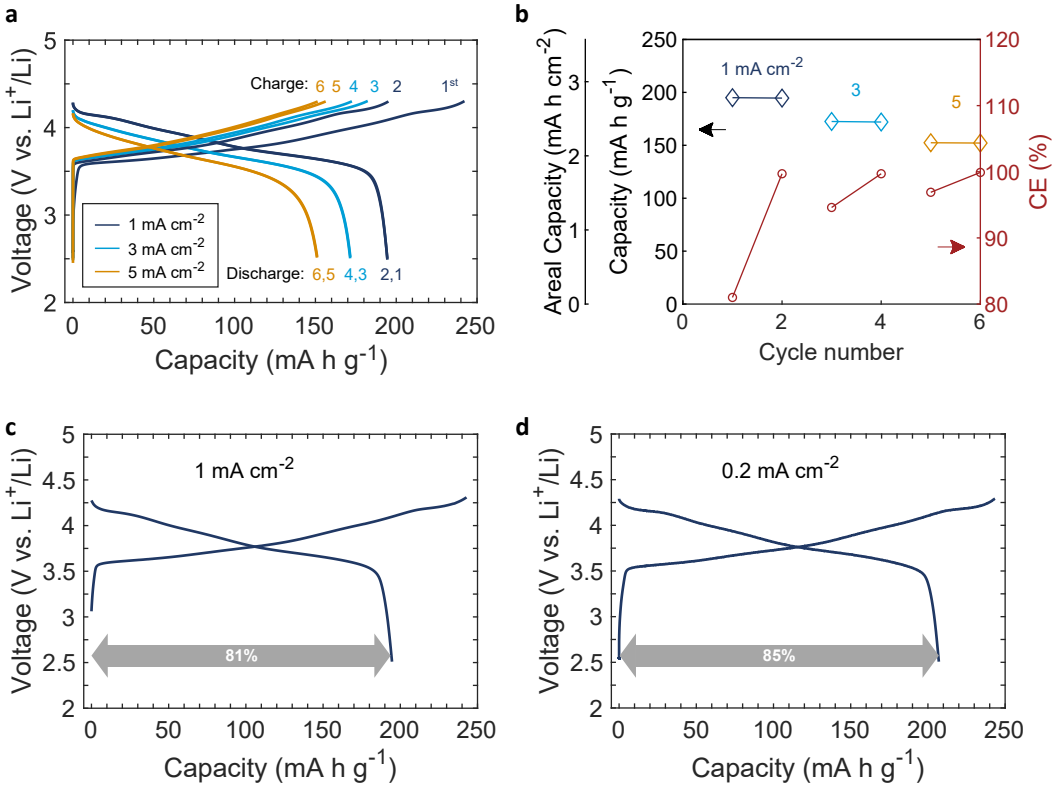


Fig. 5.5: (a) Rate performance test using the same charge/discharge current and (b) corresponding discharge capacity with the coulombic efficiency (CE). First charge/discharge cycle at (c) 1 mA cm^{-2} and (d) 0.2 mA cm^{-2}.

the current density and was 81 ± 0.3 % and 85 ± 0.2 % at 1 mA cm^{-2} and 0.2 mA cm^{-2}, respectively (Fig. 5.5c–d).

The excellent cathode charging performance was attributed to two factors. First, careful choice of materials and process conditions to meet criteria (i) to (ix) given above. Fig. 5.6 shows the Li extracted (y) during charge/discharge at 15/1 mA cm^{-2}, which translates to a SOC of 7% (y ∼ 0.17: discharge) and 79% (y ∼ 0.72: charge), and conforms to the target low volume expansion of ∼3%. Second, the three-electrode set-up, not often used for SSBs, allowed the underlying performance of the cathode to be investigated excluding any overpotential from the Li-In anode [71, 166, 167].

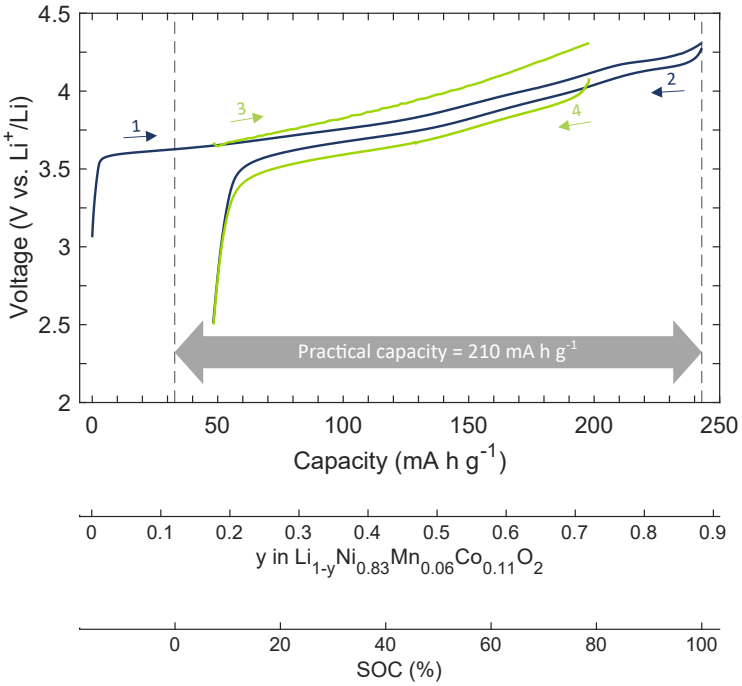


Fig. 5.6: Li content and SOC in the CAM during (1) first charge, (2) first discharge both at a current density of 1 mA cm^{-2}, (3) fast charge at 15 mA cm^{-2}, and (4) discharge at 1 mA cm^{-2}.

5.2.2 Fast-charging cycle performance at 30 °C

The cycle life of the composite cathode at a high charge current density of 15 mA cm^{-2} and a discharge current density of 5 mA cm^{-2} in a 2-electrode set-up, corresponding to rates of 4.8 C and 1.6 C respectively was investigated. The evolution of cathode voltage and current density with time for one exemplary cycle, applied after the rate test (Fig. 5.4) is shown in Fig. 5.7.

Fig. 5.8 shows that after 3000 asymmetric 4.8 C/1.6 C cycles the capacity reduced to 81 ± 2 % of the first cycle and CE was >99% per cycle. The corresponding areal capacity reduced to <2 mA h cm^{-2}, with CAM utilization reduced from 67% to 54% over 3000 fast-charging cycles.

To understand the capacity fade mechanism, the charging curves were further analysed as a function of cycle number in Fig. 5.9. The curves shifted to higher

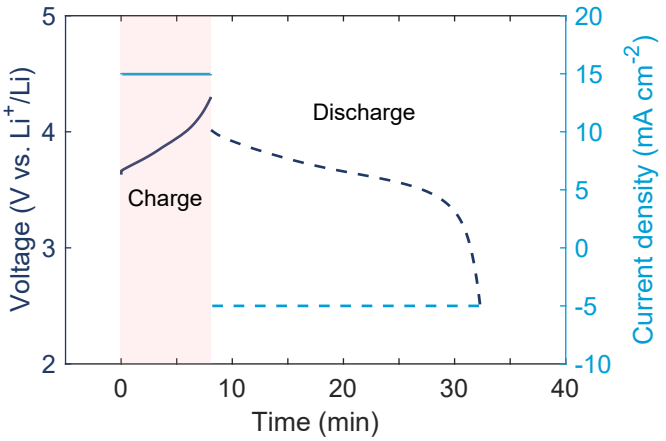


Fig. 5.7: One exemplary fast charge/discharge cycle over the time at 30 °C.

voltages more quickly in the first 50 cycles and then remained more similar in the last 1000 cycles. An ohmic resistance increase explains the progressive reduction in the cut-off voltage at higher cycle numbers (Fig. 5.9a) and therefore fading of capacity and reducing CAM utilization. Fig. 5.9b shows that the overpotential increase was similar at the beginning (10 mA h g^{-1}) and end (100 mA h g^{-1}) of the charging profile. This behaviour is consistent with a steady increase in ohmic resistance, arising from the progressive formation of an interfacial layer of lower ionic conductivity, or other impedance, at the SE/CAM interface. In contrast, the contribution to capacity fading due to CAM ionic or electronic isolation

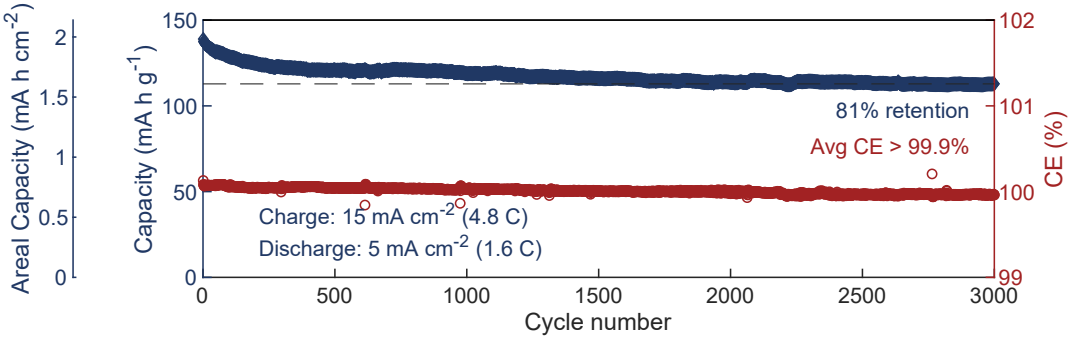


Fig. 5.8: Discharge capacity at 30 °C and 15/5 mA cm^{-2} with cycle numbers.

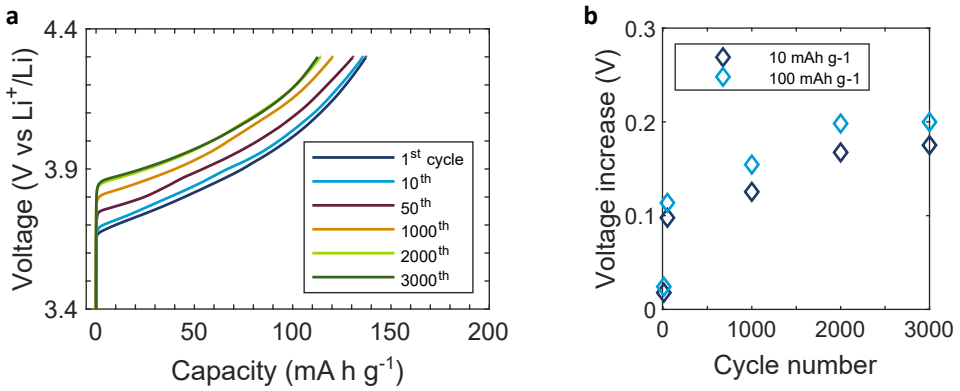


Fig. 5.9: Cycle life test at 30 °C. (a) Charge curve evolution, (b) voltage increase of the charge curve.

due to interfacial debonding and cracking was less significant because voltage increases would be expected to be more marked towards the end of charge [128]. The expected trends in voltage/capacity curves for ohmic increase or interfacial debonding mechanisms are shown schematically in Fig. 5.10.

To clarify whether the origin of the small but steady ohmic cell resistance increase arose at the anode or the cathode, electrochemical impedance spectroscopy (EIS) was performed using a combination of 2 and 3-electrode arrangements shown in Fig. 3.11, with typical Bode and Nyquist plots acquired before cycling and after

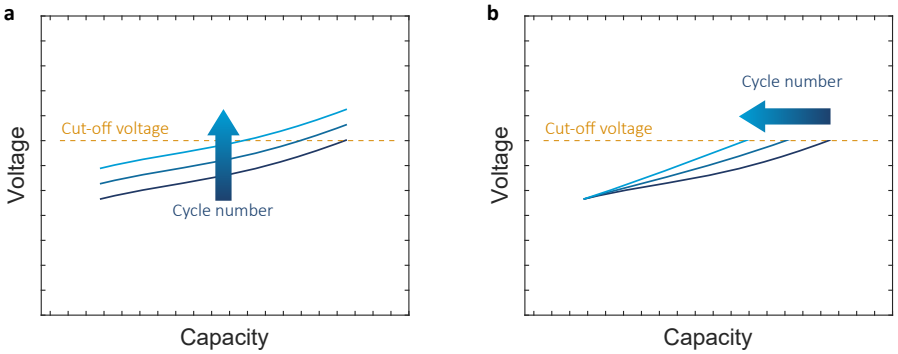


Fig. 5.10: Schematic of the voltage/capacity charge curve evolution with increasing cycle number assuming galvanostatic cycling caused by (a) an ohmic resistance increase e.g. by a passivation layer or (b) a non-ohmic resistance increase e.g. by loss of active material.

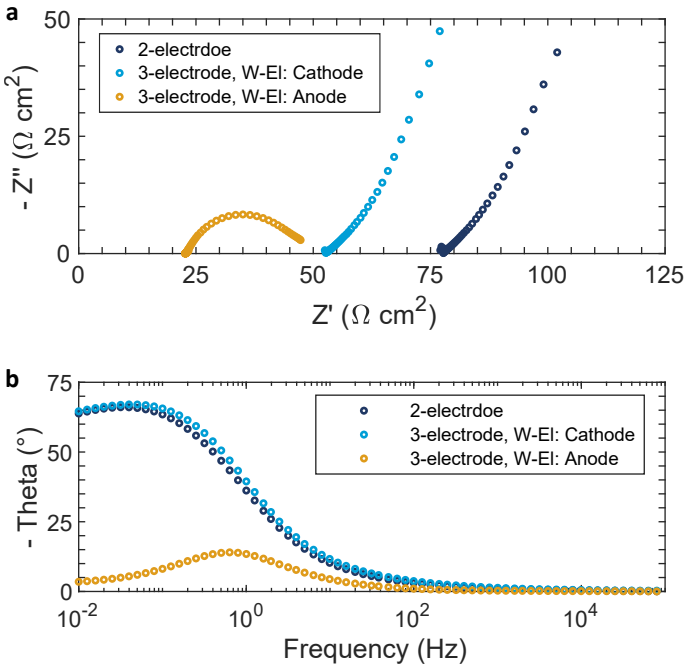


Fig. 5.11: (a) Bode plot and (b) Nyquist plot of a cell before cycling.

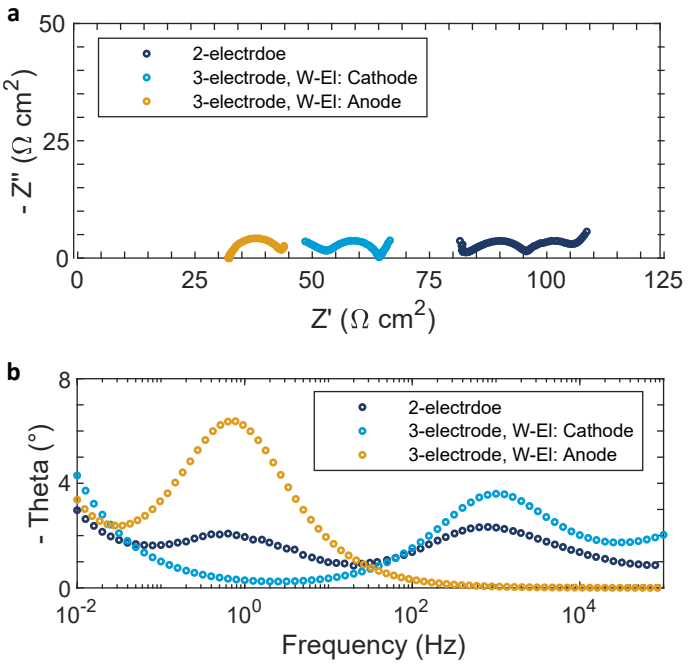


Fig. 5.12: (a) Bode plot and (b) Nyquist plot of a cell after charge.

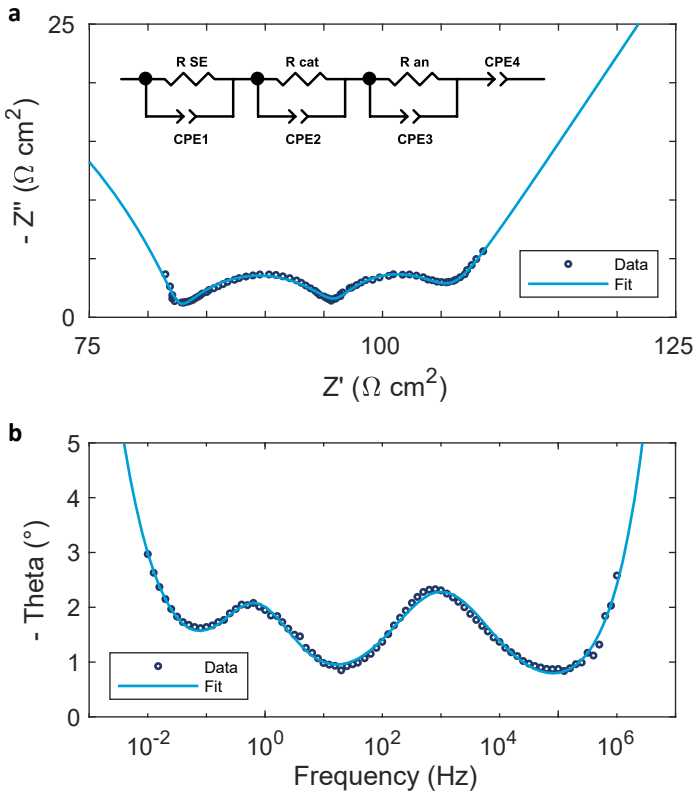


Fig. 5.13: Experimental data and fitted curve of a SSB after cycling using the equivalent circuit shown as (a) Nyquist plot and (b) Bode plot.

charge provided in Figs. 5.11–5.12. An equivalent circuit shown in Fig. 5.13a was used for fitting and accounted for resistances originating from the SE separator R_{SE}, the cathode R_{cat} and the anode R_{an}. Fig. 5.13 compares fitted with experimental data exemplary in a Nyquist and Bode plot.

The evolution of the Nyquist and Bode plots during cycling is shown in Fig. 5.14a–b. There was a progressive increase in the cathode interfacial resistance over cycling shown in Fig. 5.15, with a slower increase after approximately 300 cycles, suggesting that the ohmic resistance increase originated from the composite cathode. The dominant mechanism for resistance increase was therefore ascribed to the ongoing decomposition of the sulfide SE due to its limited electrochemical stability, with a more limited contribution due to solid-solid SE/CAM contact loss

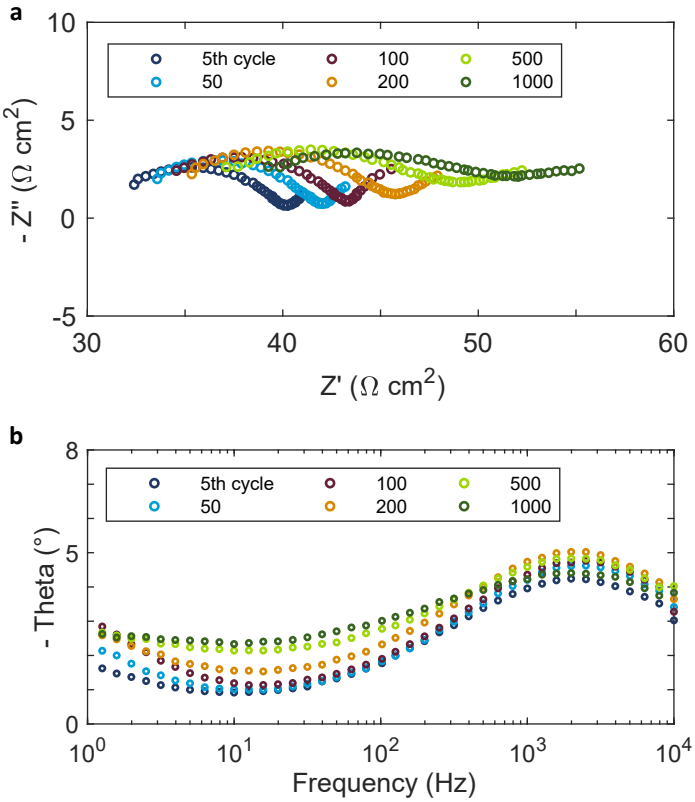


Fig. 5.14: Evolution of the cell impedance with cycle numbers (a) Nyquist plot (b) Bode plot.

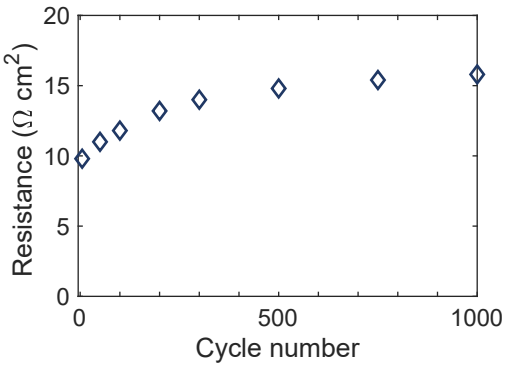


Fig. 5.15: Interfacial resistance in the composite cathode (R_{cat}) with cycle number, determined by fitting the results shown in Fig. 5.14.

because of CAM volume expansion/contraction [141, 142]. The absence of any discontinuous or catastrophic resistance increases suggests that even relatively low axial stack pressures can be effective in mitigating the effects of cyclic volume changes in the NMC/CAM [129, 148].

5.2.3 Pore evolution in the composite cathode

To confirm a relatively low rate of mechanical degradation, a combination of plasma-focused ion beam (P-FIB) depth milling, SEM imaging, and 3D image reconstruction was used [168, 169]. SEM images were acquired in parallel planes every 100 nm of milled depth and then reconstructed to form the 3D images shown in Fig. 5.16a–c before cycling, after 10 and 1000 cycles respectively. Using a grey level threshold, the pores were isolated in the images, and the pore volume before cycling was estimated at 3%, which underlines the efficacy of the combined materials selection and manufacturing approach. The pore volume after 10 cycles

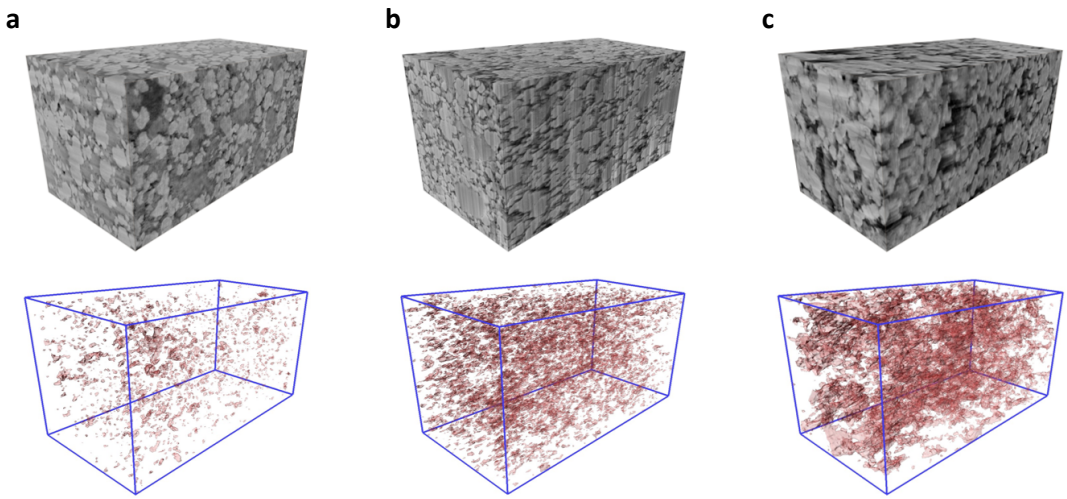


Fig. 5.16: Evolution of the cathode microstructure and the pore volume in the composite cathode (b) before cycling, (c) after 10, and (d) after 1000 cycles. The analysed volume was 20 µm × 20 µm × 40 µm. The data was obtained by the help of Junfu Bu (Post-doc, University of Oxford).

increased only slightly to 3.6% due to net CAM volume changes because of partial intercalation during discharge of Li-ions deintercalated during charge [66]. After 1000 cycles this progressive effect increased the pore volume to 6.9%, but nonetheless represented a comparatively slow rate pore volume increase that is ascribed to the low CAM volume expansion (3%) [168]. Despite the pore volume increase and relatively low axial stack pressure, the cathode microstructure after 1000 cycles remained largely intact, as shown in Fig. 5.16c, and with 81% capacity retained up to 3000 cycles (Fig. 5.8).

5.2.4 Increased cathode loading performance at 80 °C

The performance of composite cathodes with increased active loading (thickness) is shown in Fig. 5.17a–c, from 15 mg cm^{-2} (70 µm) to 30 mg cm^{-2} (140 µm) and 45 mg cm^{-2} (210 µm). A current density of 50 mA cm^{-2} was used to keep charging times short, even for the thicker cathodes, and is amongst the very highest charging rate reported for SSB cycling. To maintain CAM utilization >70%, the temperature was raised to 80 °C, which also led to extra capacity of ∼39 mA h g^{-1} compared with 30 °C and a charging current density of 15 mA cm^{-2} as shown in Fig. 5.18. Despite the higher cathode loading, the increased temperature facilitated a higher CAM utilization for the same current density (but therefore lower C-rate), as shown in Fig. 5.17. At 80 °C, CAM utilization was still 85%, even after ∼10 min of very high charging current densities of 50 mA cm^{-2} and an areal capacity of 8 mA h cm^{-2}. The retained capacity of the cathode with a relatively low areal loading (15 mg cm^{-2}) was almost 100% after 100 cycles as shown in Fig. 5.17a. Interestingly, the lower cathodic overpotential at elevated temperature for the thicker electrodes led to higher effective cut-off voltages, exacerbating sulfide electrochemical instability and CAM volume expansion and thus accelerating degradation over 100 cycles (Fig. 5.17b–c).

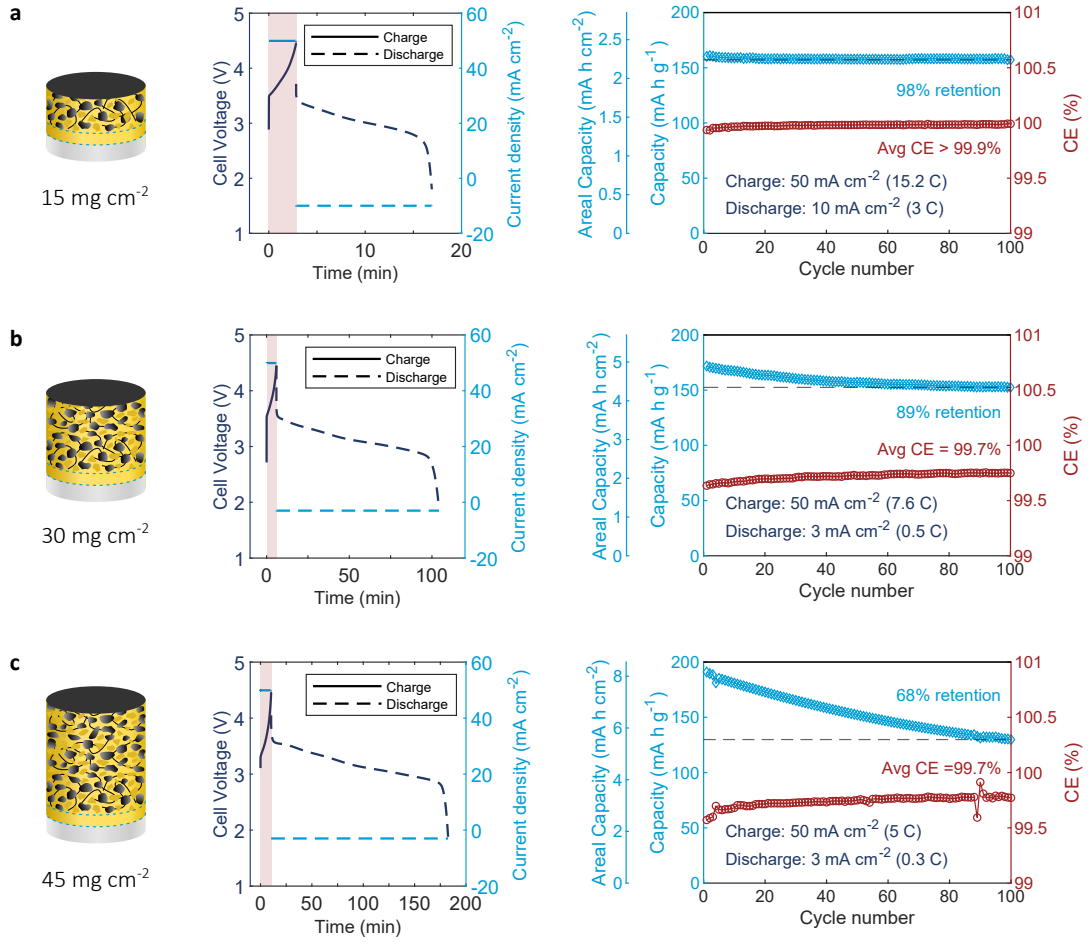


Fig. 5.17: Cycle behaviour at a charge current density of 50 mA cm^{-2} and 80 °C for different CAM loadings. One charge/discharge cycle and the corresponding capacity fade up to 100 cycles for an active loading of (a) 15 mg cm^{-2} (b) 30 mg cm^{-2} (c) 45 mg cm^{-2}. The cell voltage was measured at the cathode vs. the Li-In anode.

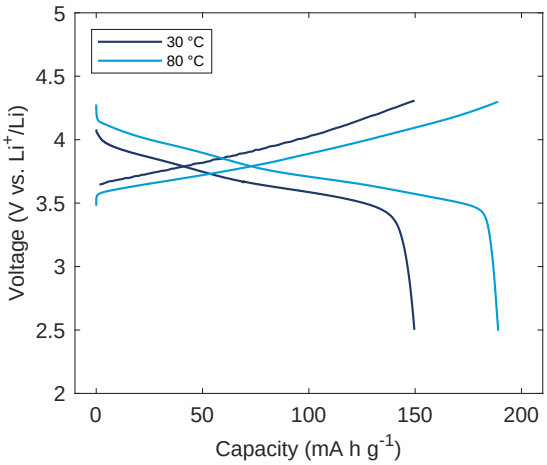


Fig. 5.18: Effect of temperature on SSB cells cycled at a charge/ discharge current density of 15/1 mA cm^{-2}.

5.2.5 Specific energy and current density comparison

A comparison of the specific energy of the different composite cathodes as a function of the current density is shown in Fig. 5.19. For consistency, only pellet-type SSBs cycled in a similar cell set-up used here were chosen from the literature and are shown in grey [20, 135, 148, 157, 158, 170]. Most prior work was conducted in a 2-electrode arrangement and was limited to a low current density and/or low areal capacity that led to a low specific energy, which may not reflect potentially encouraging cathode performance. Nonetheless, the current work shows a marked improvement over previous studies. It is worth noting that the high specific energy cannot be provided by conventional LIBs at the fast-charging times used here because Li plating in the graphite anode usually limits current densities to <4 mA cm^{-2} [156, 171]. Fig. 5.20 is the corresponding Ragone plot assuming for every point a separator SE thickness of 20 µm and a Li anode of 30 µm thickness. Based on these assumptions, composite cathodes in the present work could deliver a specific cell energy density of ∼400 W h kg_{cell}^{-1} (45 mg cm^{-2}) at 30 °C and 80 °C for low charging times of <1 h (10 mA cm^{-2}) and <10 min (50 mA cm^{-2}), respectively. The Ragone plot shows that the cathodes might deliver a high

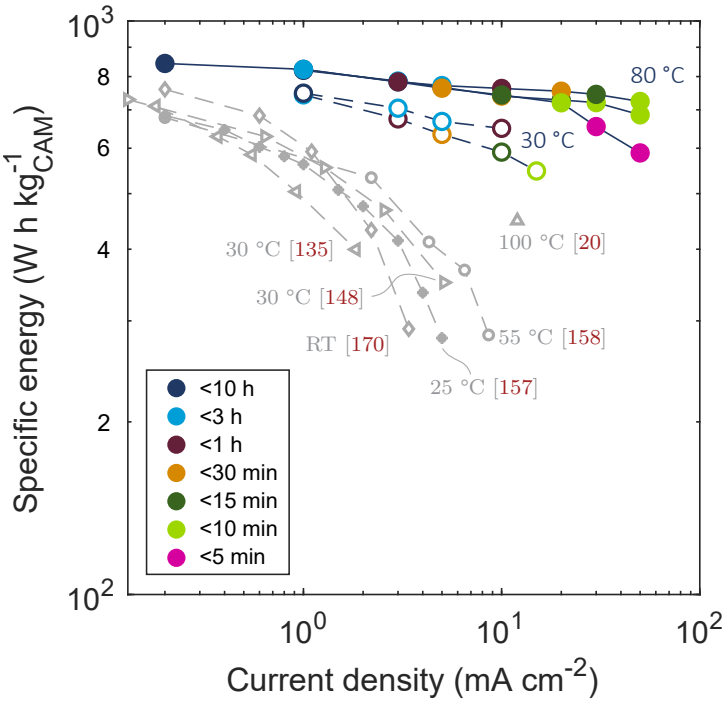


Fig. 5.19: Comparison of specific energy at different current densities. The specific energies from this study (colours) and the literature (grey) were calculated based on the cathode performance and CAM mass. The different colours indicate the charge time.

specific power of >1000 W kg^{-1}_{cell} for fast-charging SSBs while maintaining a high specific energy of ∼400 W h kg^{-1}_{cell}.

The results suggest that argyrodite-based composite cathodes designed according to criteria (i-ix) are suitable for fast-charging applications, elevating the SOC from 10% to 80% in only 10 min. Despite the thermodynamic instability of the sulfide SE, the cathode can be fully functioning for 3000 cycles at high charge current density. All cathodes investigated in this study were prepared without any CAM coating or polymer binder, and the use of the latter, likely required to form more scalable sheet-type cell formats, can be expected to undermine some of the performance data reported here. Nonetheless, the results suggest that with a focus on asymmetric fast charge/slow discharge, practical SSB cathodes could be within reach.

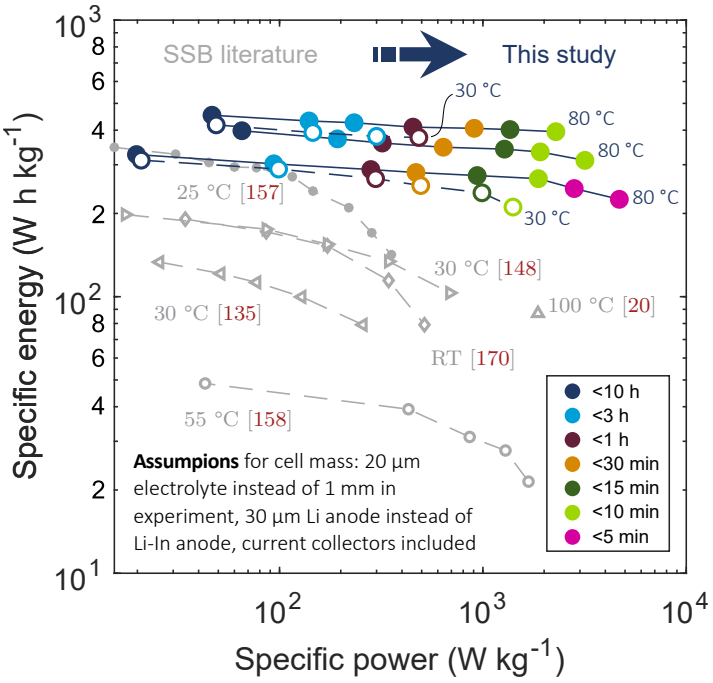


Fig. 5.20: Ragone plot. Comparison of the specific energy provided at different specific powers. The specific energies and specific powers from this study (colours) and the literature (grey) were calculated assuming the entire cell stack mass, and using an assumed 20 µm thick SE separator and a 30 µm thick Li anode. The different marker colours indicate the charge time.

5.3 Conclusions

An argyrodite-based solid-state cathode was cycled at a very high charge current density of 15 mA cm^{-2} in a 3-electrode arrangement and retained a high discharge capacity (150 mA h g^{-1}, 71% active material utilization, ~8 min charging time) at 30 °C. Fast charging (4.8 C) was demonstrated for 3000 cycles at 30 °C with 81% active capacity retention. There was only small capacity fading per cycle, despite the high charge current density and thermodynamic instability of the solid electrolyte. There was relatively slow and slight, progressive pore volume increase and any active particle isolation played only a small role in capacity

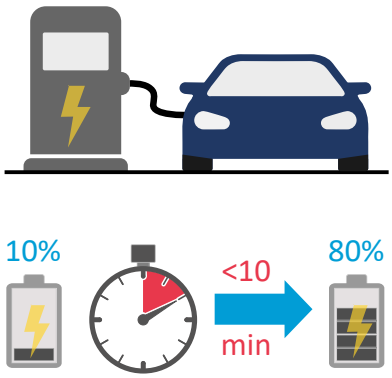


Fig. 5.21: Visualization of a desired fast charging time of <10 min from 10% to 80% SOC which was demonstrated with sulfide-based SSB cathodes in this study.

fading. When the temperature was increased to 80 °C, a charge current density of 50 mA cm^{-2} and a charge time of ∼10 min could be sustained at an areal capacity of 8 mA h cm^{-2} (85% active material utilization). The implementation of a 3-electrode arrangement showed that sulfide-based composite cathodes can operate well at fast-charging rates as summarized in Fig. 5.21, especially where electrode preparation provides a high as-manufactured density with dispersed active particles in intimate contact with the solid electrolyte. Future work will focus on how fast-charging performance may be translated to larger cell formats.

5.4 Experimental details

Cathode preparation. Commercial powders of $LiNi_{0.83}Mn_{0.06}Co_{0.11}O_2$ (NMC, MSE Supplies), Li_6PS_5Cl (LPSCl, MSE Supplies) solid electrolyte (SE), and carbon nanofibers (CNFs, Sigma-Aldrich) were mixed in a Fritsch ball mill at a weight ratio of 70:27.5:2.5 (volume ratio: 44:52:4) and milled at 140 rpm for 30 min. Single crystal NMC was chosen because it exhibited high mechanical integrity during cell manufacturing and cycling, with high intrinsic specific capacity. Mean particle diameters for NMC and LPSCl were 3 µm and 1 µm respectively.

Cell Assembly. 2-electrode cells were assembled by stacking a layer of LPSCl SE (30 mg) and a layer of the cathode mixture (4.2 mg and 12.6 mg to give 15 mg cm^{-2} and 45 mg cm^{-2}) in a polyether ether ketone (PEEK) mould and subsequent pressing at 500 MPa using the plungers of a WC die set. Li-In anodes were matched to the cathode loading and made from 1 to 3 stacks of a 70 µm thick In foil and a 30 µm thick Li foil. The anode stacks were placed on the SE pellet and pressed with a Cu current collector at 500 MPa for 5 min. An asymmetric stack pressure of 0.2 MPa on the cathode and 10 MPa on the anode was applied by a combination of a compression spring and a calibrated torque wrench.

Finite element method (FEM) calculations. Calculations were carried out in COMSOL 5.5. It was assumed that there was no relative movement at the PEEK/sulfide interface due to the high friction resulting from the pressure (500 MPa) under which the pellet was formed inside the mould. A load of 0.2 MPa was applied at the cathode and 10 MPa at the anode due to the compression spring and the clamping force of the bottom plunger, respectively. Note, this assumption of high pellet/mould interfacial friction was supported by the firm location in the cell after pressing and the impossibility of disassembly.

Electrochemical measurements. Electrochemical impedance spectroscopy (EIS) for the cycle performance analysis was conducted similarly to previous studies after charging to a cut-off voltage of 4.3 V vs. Li^+/Li [26, 172]. A narrow frequency window range from 10^4 to 1 Hz was chosen to acquire information from the cathode and to keep the measurement as short as necessary. The open circuit potential at the start of the measurement was significantly lower than the cut-off voltage at ∼4.1 V vs. Li^+/Li ($y = 0.72$) because of a high overpotential caused by the high charging rate (15 mA cm^{-2}). It was assumed that the Li diffusivity in the single crystal CAM particles stayed relatively constant for different Li concentrations in the range $y = 0.2$ to $y = 0.72$ and therefore had little or no effect

on the impedance change over the cycle number [173]. Electrochemical techniques are described in more detail in chapter 3.3.

Cathode microstructure. Scanning electron microscope (SEM)/energy-dispersive X-ray spectroscopy (EDX): Sulfide-based cathodes were cross-sectioned using an automated Ar ion polishing system (PECS 2, Gatan) and transferred under vacuum into a Zeiss Merlin SEM using an airtight transfer device. Images were taken by the in-lens secondary electron detector. EDX was carried out using an Oxford Instruments X-Max 150 silicon drift detector and analysis was conducted in AZtec software. SEM/P-FIB for void analysis: An in-house developed design for cell/mould disassembly, shown in Fig. 3.6b, was used to allow recovery of pristine and cycled cells from the PEEK mould which could then be analysed by a variety of techniques. Pore volume analysis: A Thermo Scientific Helios G4 Plasma FIB Dual Beam (or P-FIB) system was used to study the microstructure changes of pristine and cycled composite cathodes. A large trench was firstly milled in bulk cells using a focused Xe^+ beam at 30 kV and 2.5 µA around a selected region, which provided space for re-deposited materials and to avoid shadow effects during the SEM scanning process. The edge of the milled cross-section was further polished using a lower beam current from 60 nA down to 4 nA at 30 kV to remove FIB-induced roughness. SEM images were acquired in parallel planes every 100 nm of milled depth. The pores in the composite cathode were isolated using a gray-level threshold. ImageJ and Avizo software were used to process and generate 3D visualizations of the P-FIB datasets.

Specific energy calculations. An assumed 30 µm thick Li anode and a 20 µm thick separator together with experimental data of the composite cathodes were used in specific energy and power (Ragone plot) calculations.

Spray printing of thin layers for sulfide-based all-solid-state batteries

Although all-solid-state battery (SSB) performance has steadily improved in recent years, most research has focused on small (diameter <10 mm), thick (separator >500 µm) pellet-type cells that used non-scalable manufacturing routes and lead to a low cell energy density. Real applications require thinner and larger sheet-type cells made by scalable techniques. Herein a scalable layer-by-layer spray printing approach is used for the manufacture of sheet-type SSB components such as the SE separator, composite cathode, and metal-free anode. Sprayed sulfide SE separators with thicknesses as low as 10 µm and high ionic conductivity of 1 mS cm^{-1} are fabricated. A sprayed composite cathode is also demonstrated, and delivers a capacity retention of 63% after 800 cycles. The flexibility of spray printing for process integration is highlighted by the fabrication of an anode-free cell consisting of a sprayed Ag-C layer and a sprayed SE layer.

6.1 Introduction

Most SSBs have been constructed as uniaxially cold-pressed pellet-type cells, which have low process scalability, and use an impractical SE separator thickness that may be as high as 1 mm, resulting in a low overall cell energy density. Productive and scalable techniques are required for the manufacture of practical sheet-type SSBs with reduced SE separator thickness and larger cell area (e.g. A5 size), but which can preserve the most attractive performance aspects of the pellet-type cells.

The production of sulfide-based SSBs with high energy density at large scale faces several challenges, which apply to the SE separator, the cathode, and the anode. For example, in scaling from pellets to sheets, addition of a polymeric binder is required for the SE and cathode to stabilize internal cohesion and to ensure adhesion to the current collector, respectively. Unfortunately, high binder fraction impedes Li-ion and electron movement. Further, the instability of sulfides in the presence of water vapour exacerbates production difficulties as a dry room or inert atmosphere is required to prevent formation of toxic H_2S [69]. Both dry and wet chemical approaches have been investigated for sheet-type SSB production [71, 127]. Whereas dry processes based on polytetrafluoroethylene (PTFE) fibrillation showed remarkable performance it is still unclear whether the approach can be economic and produce cells at large scale [111, 112, 174]. A wet SSB manufacturing route that is similar to current LIB production (i.e. slurry casting) would have the advantage of drawing on existing capacity and expertise, and high productivity. However, the aforementioned high reactivity of sulfides limits the choice of solvents, which also must be carefully matched with a compatible binder e.g. nitrile butadiene rubber with xylene, for successful slurry formation [135, 175–177]. Whereas non-polar solvents such as xylene disperse sulfide particulates and dissolve binders, more polar solvents e.g. ethanol or isopropanol (IPA), can chemically dissolve the sulfides, which are then re-precipitated during drying of a slurry cast SE membrane or cathode. Re-precipitated sulfide, however, may be only semi-crystalline and with reduced ionic conductivity [99]. Nonetheless, the solution/reprecipitation approach can be beneficial in creating an intimate contact between the CAM and the sulfide SE in composite cathodes [93, 117, 178].

Assuming a Li metal anode for a cell with a high overall specific capacity, the manufacturing challenges of fabricating a thin (10–20 µm), large area layer of metallic Li with high purity at low cost and large scale are formidable. Li is highly reactive in solid, liquid, and gaseous forms, highly mobile, and although soft and

deformable when solid, its ready adhesion to tooling causes challenges in handling coatings or foils. To mitigate these difficulties, so-called anode-free designs have been developed in which the metallic anode is formed in situ from excess Li from the cathode on the first cell cycle [179]. To facilitate the uniform nucleation and growth of metallic Li at the anode on the first and subsequent cycles, an Ag-C interlayer between the current collector and the SE separator has been shown to be beneficial [26].

In this chapter, a scalable layer-by-layer spray printing approach is introduced that is applied to sulfide-based SSB manufacture. The spraying approach is shown to be suitable for all relevant SSB cell components, such as the separator, cathode, and anode. Large area (10×10 cm^2) sulfide SE separators with high ionic conductivity of 1 mS cm^{-1} are produced with a thickness as low as 10 µm. Two different solvents are suggested for the spray printing process and their effect on microstructure, crystallinity, and ionic conductivity of the sulfide SE coatings is described in detail. A spray-printed sulfide-based SSB cathode is then demonstrated with 63% capacity retention after 800 cycles. The opportunities provided by layer-by-layer formation for novel and potential architectures such as grading is highlighted [88]. Finally, the spray process is demonstrated for the production of first a nano-particulate Ag-C layer at the anode foil/SE interface and then a subsequent sulfide SE separator coating that might find application in future scalable anode-free SSBs.

6.2 Results and discussion

6.2.1 Spray printing of thin sulfide solid electrolyte separators

A layer-by-layer, large-area spray printing process was used for the manufacture of thin argyrodite SE separators, aiming to retain the high intrinsic ionic conductivity of argyrodite, for direct use in SSB cells. The process pumps a feedstock suspension/solution at a controlled rate to an atomizing nozzle operating with

Ar gas where it is atomized into a fine spray of droplets that are directed and deposited over a heated metallic foil. On deposition of the droplets, the liquid is evaporated almost instantly, as shown schematically in Fig. 6.1; more details were shown in Figs. 3.1–3.2. The spray head is scanned in the x-y plane at a constant spray height z by a computer numeric controlled gantry to cover uniformly an area of 10 × 10 cm^2 (or more) and the whole apparatus is operated automatically inside in an Ar-filled glovebox.

Two argyrodite-based suspension/solutions were investigated: (i) ethyl acetate (EA) with PVDF binder and Li_6PS_5Cl (LPSCl), and (ii) isopropanol (IPA) and LPSCl. Mixtures (i) and (ii) are referred to as EA/LPSCl and IPA/LPSCl and were chosen as exemplary systems to study a LPSCl suspension and solution, respectively. The spray printing process allows for a high flexibility in relation to the spray area and substrate shape [180, 181]. Typical spray-printed LPSCl-based SE coatings on different substrates are shown in Fig. 6.2a–b. Ionic conductivity

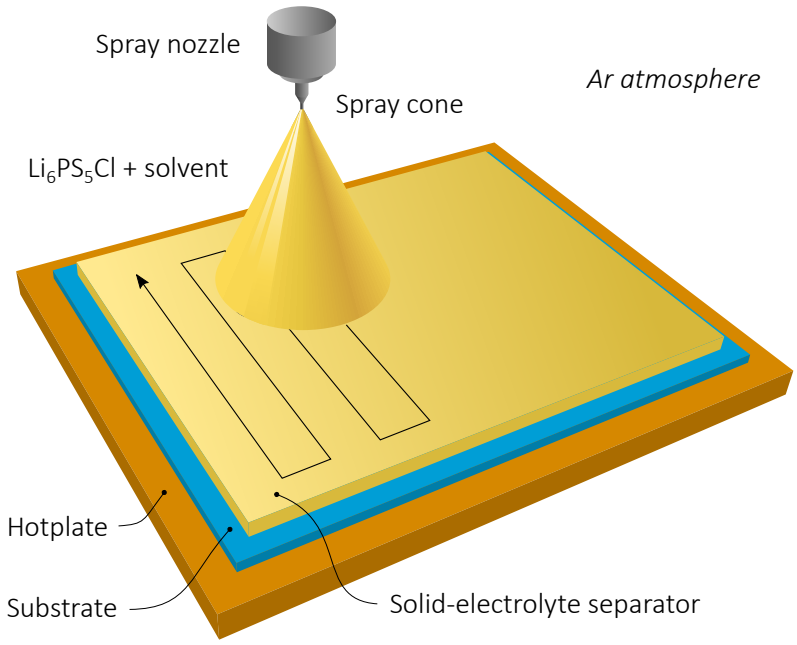


Fig. 6.1: Schematic of the spray printing process for the manufacture of SE separators.

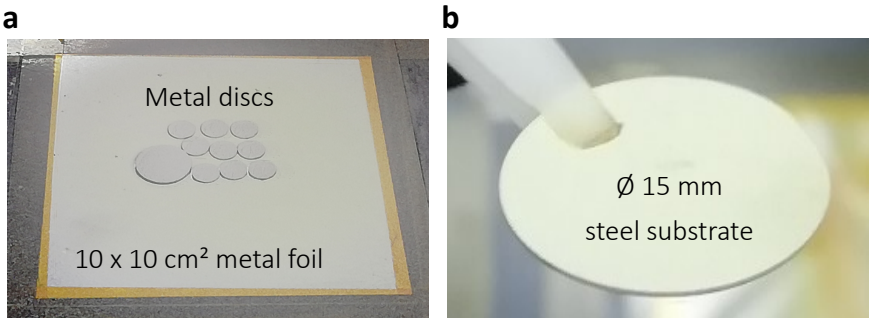


Fig. 6.2: A photograph of sprayed LPSCl-based SE onto different substrates: (a) a 10 × 10 cm² foil, and (b) 15 mm diameter stainless steel disc.

tests were conducted by SE deposition directly onto stainless-steel discs, typically comprising 5–20 sprayed layers depending on the concentration of the suspension and the target thickness.

Scanning electron microscope (SEM) images of as-sprayed IPA/LPSCl and EA/ LPSCl coatings are compared with pristine argyrodite powder in Fig. 6.3. In the

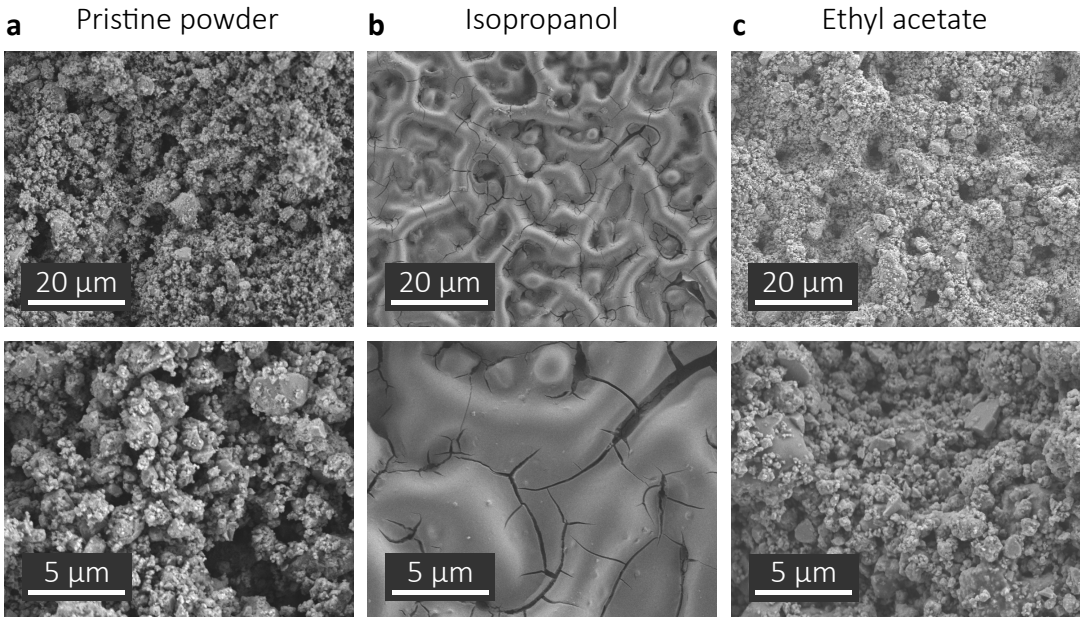


Fig. 6.3: SEM micrographs of (a) the pristine argyrodite powder and sprayed argyrodite coatings using a spray suspension based on (b) isopropanol and (c) ethyl acetate with 5 wt% PVDF binder

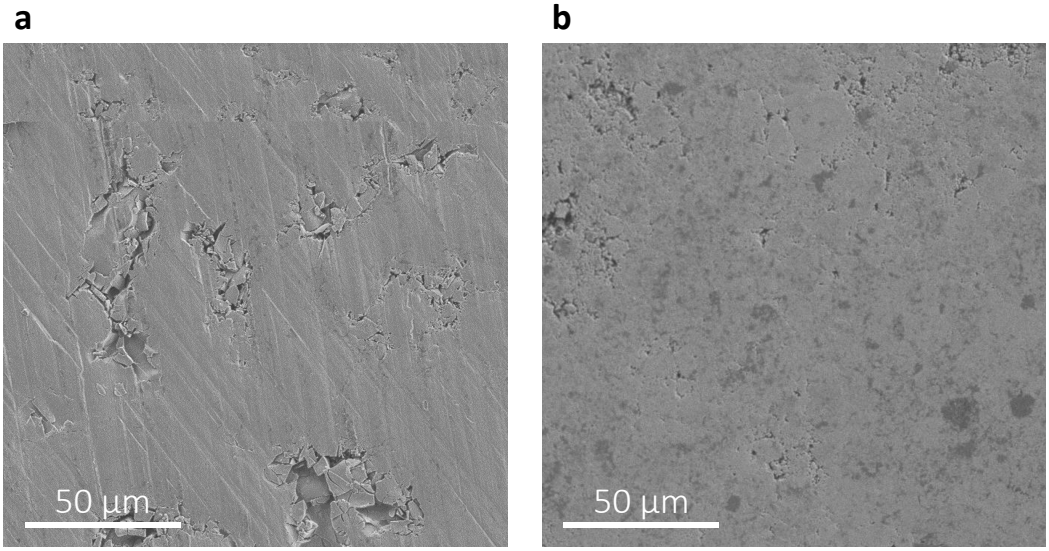


Fig. 6.4: SEM micrographs of sprayed sulfide coatings using (a) IPA/LPSCl and (b) EA/PVDF/LPSCl after densification at 500 MPa.

EA/LPSCl coating, the LPSCl particulate was preserved throughout the spraying process whereas the IPA/LPSCl coating comprised large-scale, non-particulate features suggesting that the feedstock particulate had dissolved and then re-precipitated as intended [177]. There was a significantly higher pore fraction in EA/LPSCl, estimated at >30 vol%. Conversely, precipitated IPA/LPSCl coatings had an estimated relative density of >90% but with many micro-cracks that formed during drying and likely reflected the absence of an elastic binder. Both as-sprayed coatings had a surface roughness of >5 µm (R_{max}).

Coating flatness was increased by uniaxial densification at room temperature and 500 MPa, as shown in Fig. 6.4. Fig. 6.5 shows a cross-sectional SEM image of the EA/LPSCl coating after densification at 500 MPa with almost no residual porosity, with the corresponding energy-dispersive X-ray spectroscopy (EDX) maps showing the binder located between the sulfide particles. The layer-by-layer nature of the spraying approach allowed control over coating thickness, which could be varied readily between 5 µm and 50 µm [182].

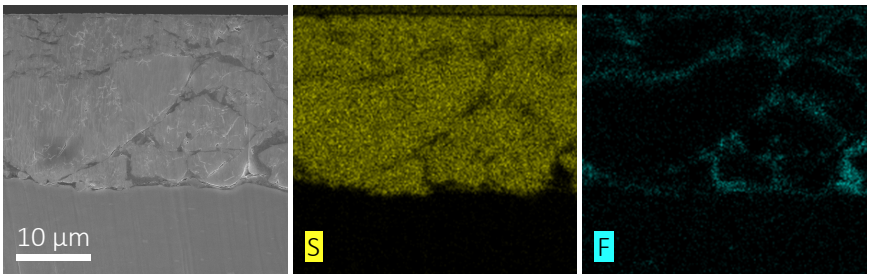


Fig. 6.5: Cross-sectional SEM image of a sprayed and densified sulfide coating with corresponding S and F EDX maps distinguishing between the electrolyte (S) and the binder (F) distribution, respectively.

Overall, a high coating density and potentially beneficial intimate solid/solid contact was suggested by the solution/reprecipitation approach. Reasonable coating densities were also achievable by the dispersion approach when combined with cold-pressing, although binder presence at particle-particle boundaries can be expected to increase ionic resistance.

The sprayed coating ionic conductivity was determined by electrochemical impedance spectroscopy (EIS) using two stainless steel blocking electrodes and the equivalent circuit previously shown in Fig. 3.10. Measurements were taken at pressures of up to 500 MPa to minimize contact resistance. Lower pressures

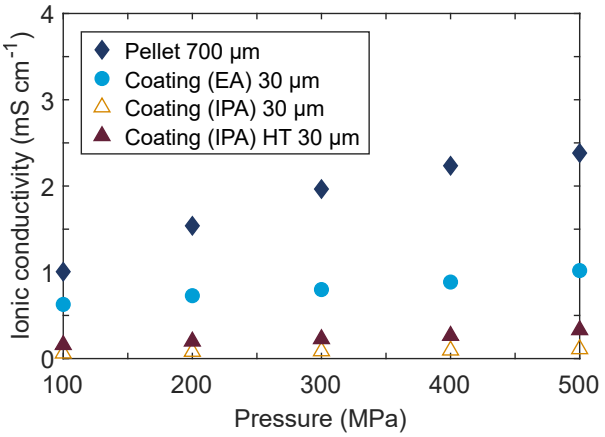


Fig. 6.6: Ionic conductivity of a pellet and sprayed coatings of LPSCl as a function of applied uniaxial pressure, as determined by EIS.

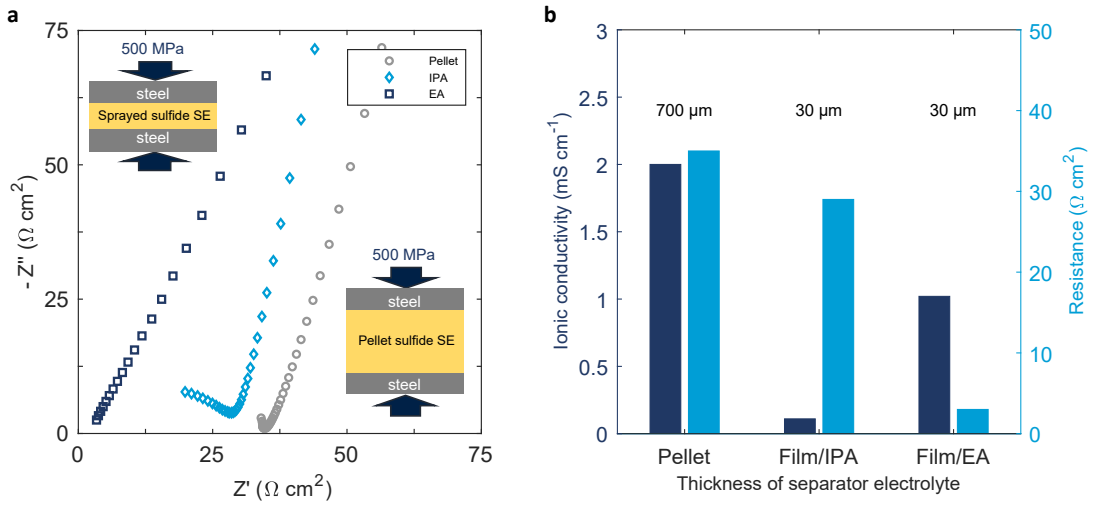


Fig. 6.7: (a) Nyquist plot of the sprayed argyrodite coatings compared with a conventional thick pellet. (b) Corresponding ionic conductivity and resistance. IPA/LPSCl and EA/LPSCl were made with 0 wt% and 5 wt% binder, respectively.

resulted in higher resistances and lower ionic conductivity, as shown in Fig. 6.6. The Nyquist plot in Fig. 6.7a shows the EIS response of the sprayed coatings alongside the response of a similar and more common 700 µm thick SE pellet, and the corresponding ionic conductivities and resistances are shown in Fig. 6.7b. The sprayed coatings had ionic conductivities of 1.1 mS cm^{-1} and 0.1 mS cm^{-1} for EA and IPA, respectively, lower than the cold-pressed pristine powder conductivity of 2.2 mS cm^{-1}. This arose because of: (i) chemical degradation of the sulfide by the organic solvent, and (ii) the influence of the ionically insulating binder in the EA sulfide coating. Despite the lower ionic conductivity, the resistance was significantly lower compared to the pellet because of the decreased thickness of the sprayed coatings. Heat treatment (HT) may increase the ionic conductivity of precipitated sulfide SEs made from a solution process, and so a 30 µm thick IPA/LPSCl coating was annealed at 300 °C [183]. As expected, the conductivity increased to 0.3 mS cm^{-1} and the corresponding Nyquist plot is shown in Fig. 6.8.

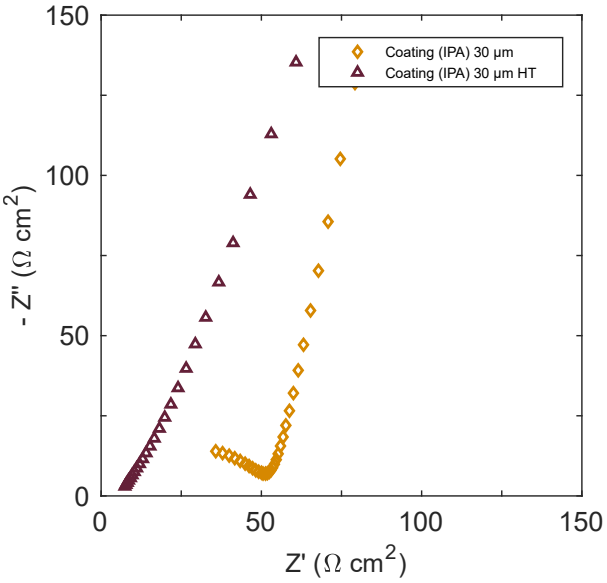


Fig. 6.8: Nyquist plot showing the influence of a heat treatment (HT) at 300 °C and 1 h on a 30 µm thick IPA/LPSCl sprayed coating.

To analyse any effect of the spray process on the interaction between solvent and argyrodite, the crystal structure was investigated by X-ray diffraction (XRD). Fig. 6.9 compares the XRD spectra of the sprayed coatings with the pristine pow-

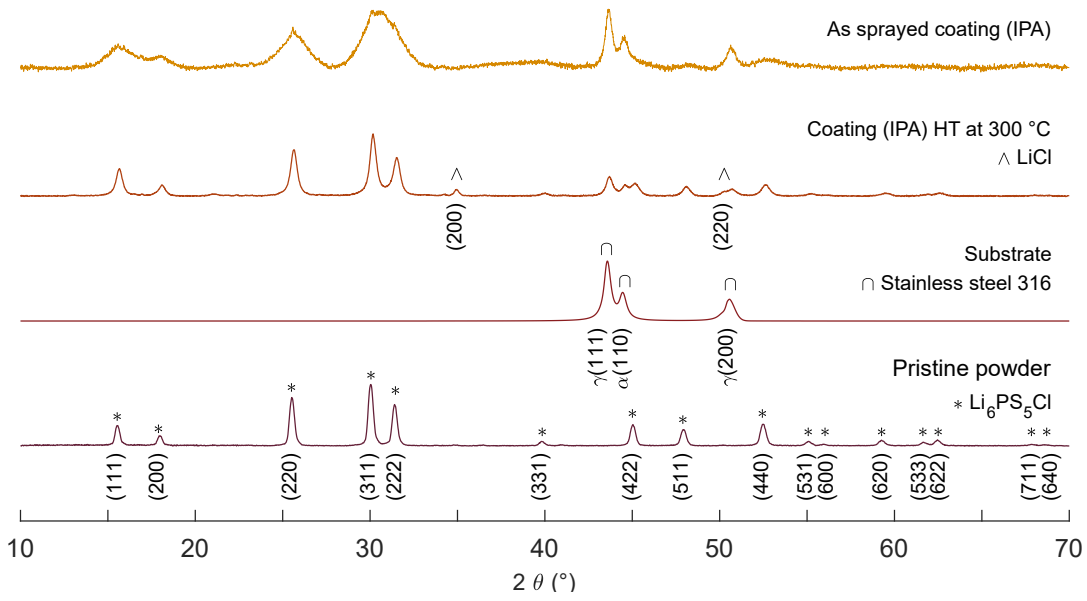


Fig. 6.9: XRD spectra of the sprayed coatings compared with the substrate and the pristine argyrodite powder [35, 184].

der. EA/LPSCl showed high crystallinity similarly to the pristine powder whereas IPA/LPSCl showed much lower intensities and much broader peaks [177]. This suggests that the conductivity decrease of the EA/LPSCl sample was predominantly caused by the addition of non-conducting binder rather than reduced crystallinity, and is consistent with previous reports [177]. In the case of IPA/LPSCl the lower crystallinity explains the lower ionic conductivity because of fewer highly mobile ionic pathways for Li-ions [183]. Annealed IPA/LPSCl showed increased crystallinity compared with as-sprayed, consistent with the increase in ionic conductivity. However, the XRD data suggested that the crystallinity was still lower than pristine powder, with LiCl and Li_2S impurities present that are known to be comparatively poor ionic conductors. Due to the absence of a polymer binder in the IPA/LPSCl coating, it can be assumed that in this case the ionic conductivity decrease probably comes from irreversible side reactions during the argyrodite/IPA exposure.

6.2.2 A spray-printed composite cathode

The processability of sulfide-based SSB cathodes by the spray printing process is explored in this section. SSB cathodes comprise active material, SE and electron conductive material. Additionally, elastic binders might be required for better adhesion and flexibility during manufacturing. Fig. 6.10 shows schematically the spray printing concept for a composite cathode, from formation of the cathode itself, through to final assembly into a functional cell. Following this scheme, first, a 30 µm thick composite cathode was spray printed from a LPSCl, $LiNi_{0.83}Mn_{0.06}Co_{0.11}O_2$ (NMC) and carbon black (CB) suspension, which were dispersed and mixed with the relatively better performing PVDF/EA mixture, and with a binder content of 3 wt%. Second, an argyrodite layer was spray printed directly onto this newly formed composite cathode to form the SE separator. The cathode and SE separator layers were then densified jointly to a

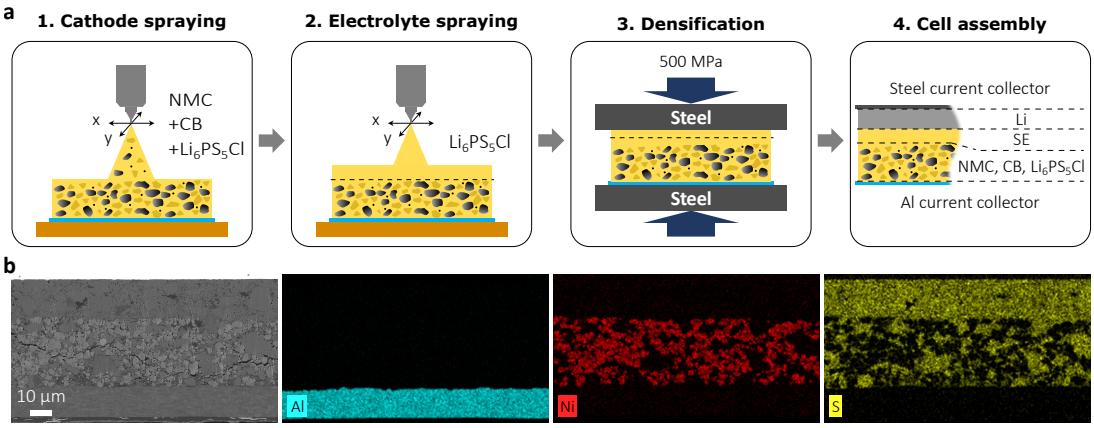


Fig. 6.10: (a) Fabrication process for a SSB based on a sprayed composite cathode. (b) Cross-sectional SEM image and corresponding Al, Ni and S EDX maps of the cathode and separator.

relative density >90% at a uniaxial pressure of 500 MPa and room temperature. Densification aims to promote solid/solid contact at (i) the individual SE/CAM particulate interfaces within the cathode, and (ii) the SE membrane/composite cathode interface. Finally, cell assembly was completed by adding a 30 µm Li foil as the anode, and then a steel foil "upper" current collector. The SEM image and corresponding Al, Ni, and S EDX maps in Fig. 6.10b show the multi-layer assembly, distinguishing the current collector (Al foil), the composite cathode (Ni from the NMC), and the percolating electrolyte pathways and thin sulfide (S) SE separator.

To investigate the intrinsic performance of the sprayed cathode alone, and to avoid short circuits that were an occasional feature of more complex spray-printed multi-layer arrangements, bespoke cells with a conservative but more robust 700 µm thick SE separator were fabricated for electrochemical investigation. These 5 mm diameter cells comprising a sprayed cathode, thick SE separator, and Li were cycled at a uniaxial stack pressure of 2.5 MPa in a PEEK mould under protective atmosphere [164]. The cathodes reproducibly delivered a discharge capacity of 157 mA h g^{-1} at 30 °C and 0.1 mA cm^{-2} (0.08 C), suggesting a CAM utilization

of 75% as shown in Fig. 6.11 (assuming a theoretical capacity of 210 mA h g^{-1}). To increase CAM utilization the cycling temperature was increased to 80 °C, which increased capacity by a further 60 mA h g^{-1} as shown in Fig. 6.11. The CAM utilization was close to a 100% at 80 °C considering an increased theoretical capacity of 220 mA h g^{-1} given the higher temperature [185]. Fig. 6.12a shows the effect of increasing C-rates at 80 °C, with capacity decreased by 26% between 0.08 C and 0.6 C. Fig. 6.12b shows that the cell with the sprayed cathode after 800 cycles at 0.6 C had a retained capacity of 63%. Capacity faded faster than in the cathode shown in the previous chapter because of the different electron conductive aid and the use of a Li anode instead of Li-In. Future improvements might be achieved by tuning the cathode architecture using the greater design freedom of the spray printing process that allows for the manufacture of graded structures of CAM particle size or binder, which has been successfully demonstrated for LIB electrodes [88, 186]. The work here shows that despite the significant differences in chemistry to LIBs, and the incorporation of a SE rather than requiring as sprayed porosity, spray printing could be a flexible platform for the manufacture of bespoke structured composite cathodes and multilayers.

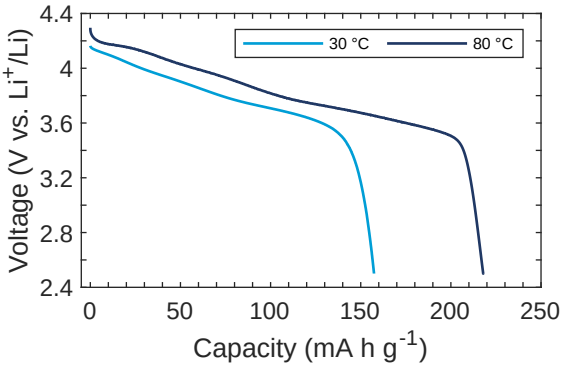


Fig. 6.11: Discharge curves of the sprayed cathode at different temperatures cycled at 0.08 C. The cathode loading was 6.1 mg cm^{-2} with a corresponding thickness of 33 µm. The weight ratio of SC-NMC, LPSCl, CNF was 70:27.5:2.5 with 3 wt% PVDF.

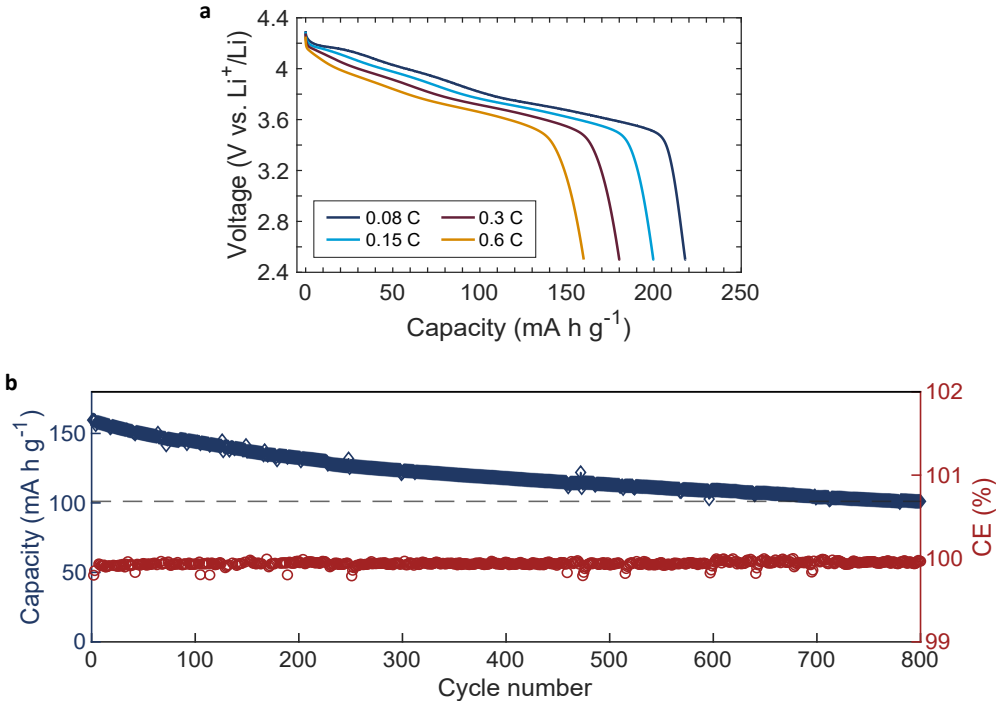


Fig. 6.12: (a) Discharge behaviour of a sprayed composite cathode at 2.5 MPa and 80 °C as a function of C-rate, and (b) discharge capacity as a function of cycle number at 0.6 C.

6.2.3 A spray-printed Ag-C layer for an anode-free cell design

To reach the high specific energy density for SSBs (400 W h kg_{cell}^{-1}) the use of a Li metal anode is preferred because other materials offer less capacity per unit mass or volume. Ideally, there should be little or no excess Li at the anode to minimize cost and maximize gravimetric and volumetric performance at the cell scale. One way to achieve this arrangement is to assemble the cell without a pre-existing Li anode, but instead to form the Li anode by plating in situ from a Li-rich cathode, on the first charge cycle [187]. Such an approach avoids the otherwise considerable difficulties in forming a Li metal anode from a highly reactive solid (foil), liquid, or vapour [21, 188].

Fig. 6.13 shows schematically the fabrication process of an anode-free high energy SSB using spray printing. To facilitate a more uniform distribution of Li plated

at the anodic current collector, Ag nanoparticles and graphite particles were dispersed in IPA/N-Methyl-2-pyrrolidone (NMP) with 10 wt% PVDF and sprayed to a thickness of ∼7 µm on the stainless-steel foil that forms the anodic current collector [26]. An argyrodite SE separator was then spray printed on top of the Ag-C layer as described above, and a NMC-based composite cathode, prepared separately by a solvent-free, dry-processing approach was pressed on top using a uniaxial pressure of 500 MPa [111]. A dry-processed cathode was preferred in this case because it was considered important to minimize the cathode binder fraction in order to reduce impedance at the CAM/SE inter-layer interface. The dry process successfully allowed the binder fraction to be reduced to 1 wt% of polytetrafluoroethylene (PTFE), rather than >2 wt% associated with slurry cast composite SSB cathodes and SE separators [189]. Fig. 6.14a shows a plan-view SEM image of the upper free surface of the dry-processed cathode showing ∼50 nm thick PTFE fibrils that formed during dry shear processing, anchored to the NMC particles, and forming a 3D mesh, or web that provided electrode mechanical stabilization. PTFE fibrils were confirmed by the F EDX map shown in Fig. 6.14b, which allowed for differentiation between fibrils and the CNFs identified in the C EDX map.

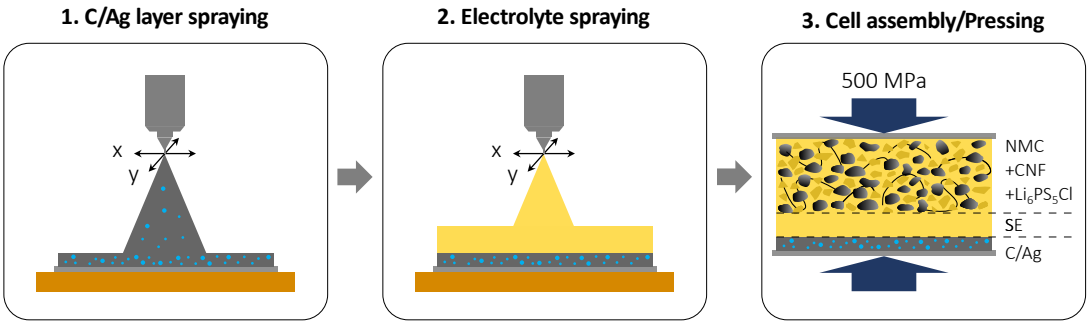


Fig. 6.13: Schematic of the fabrication process for a metal anode-free SSB.

To investigate the electrochemical performance of the sprayed Ag-C layer, a full cell according to the configuration shown in Fig. 6.13 was fabricated. To avoid any problem with short circuits due to the low thickness of the sprayed separator coatings that will require more sophisticated cell assembly with low tolerances during positioning and stacking, bespoke cells with a thicker more reliable SE separator but otherwise identical formulations were assembled and cycled at a

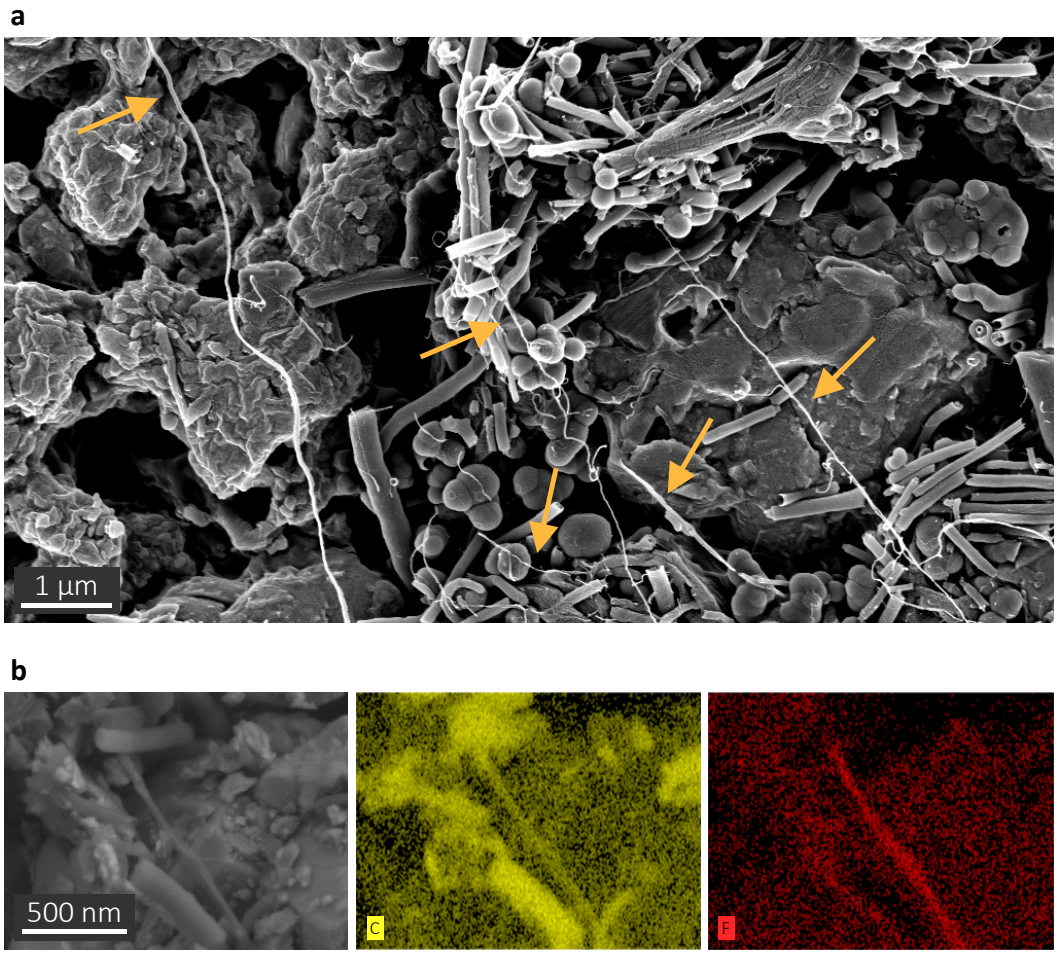


Fig. 6.14: (a) SEM image of a composite cathode made by a dry-mixing approach used with a so-called Li-free anode. The arrows show PTFE fibrils formed by shearing during processing. (b) C and F EDX maps differentiate the carbon nanofibres and fibrillated PTFE, respectively. SEM data was obtained by the help of Guillaume Matthews (Post-doc, University of Oxford).

stack pressure of 2.5 MPa. Fig. 6.15 shows the first two charge and discharge curves at a current density of 0.2 mA cm^{-2} and 30 °C. Cells showed reproducibly a first cycle coulombic efficiency (CE) of 78% and a discharge capacity of 190 mA h g^{-1}, representing a CAM utilization of 90%. Despite the encouraging data after one cycle, cell failure occurred in the beginning of the second charge. This suggests that the Li did not plate/strip uniformly. Current understanding of the underlying principle of the anode-free layer is that Li plates onto, or reacts with, the high surface area, porous Ag-C thin layer avoiding metallic Li and associated void and dendrite formation at the sulfide SE interface. However if Li-ions cannot continue to be transported through the Ag-C layer at the rate determined by the current density, Li plating at the Ag-C/LPSCl interface or in pores that are within the Ag-C layer might become energetically more favourable. The Ag-C layer might in this case act as a structured current collector with higher surface area than a plane foil [190].

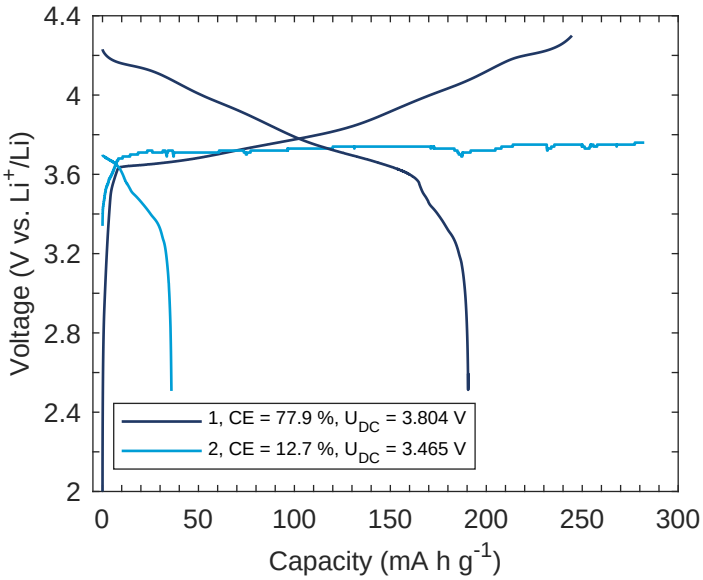


Fig. 6.15: First charge/discharge cycle of a metal anode free SSB using a Ag-C interlayer.

To investigate Li deposition during plating more carefully, pristine and cycled cross-sections of the Ag-C layer are compared in Fig. 6.16. The temperature was elevated to 60 °C where the higher Li mobility in the C was assumed to improve the functionality of the anode-free approach. Fig. 6.16a is a SEM cross-section image of the pristine sprayed Ag-C layer and the SE separator with corresponding Ag, C, S EDX maps showing differentiation between the layers and intimate inter-layer contact. The cross-section in Fig. 6.16b shows the Ag-C layer after a transferred charge of 2 mA h cm^{-2}. The cross-section after charging shows that Li was plated as previously observed at the current collector/Ag-C interface and forms a Ag-Li phase [26]. This suggests that the sprayed Ag-C layer provided some function in aiding Li deposition as expected. Nonetheless, more research is needed to better understand particularly the role of the Ag nanoparticles and the influence of the carbon structure on Li deposition.

Fig. 6.17 shows the influence of the SE thickness on the cell energy density per unit volume and mass, increasing by 10% and 15% to 1050 W h L^{-1} and 300 W h kg^{-1}, respectively when the SE thickness was reduced from 50 µm to 5 µm, which spans the range readily demonstrated by spray printing. Notwithstanding more regular

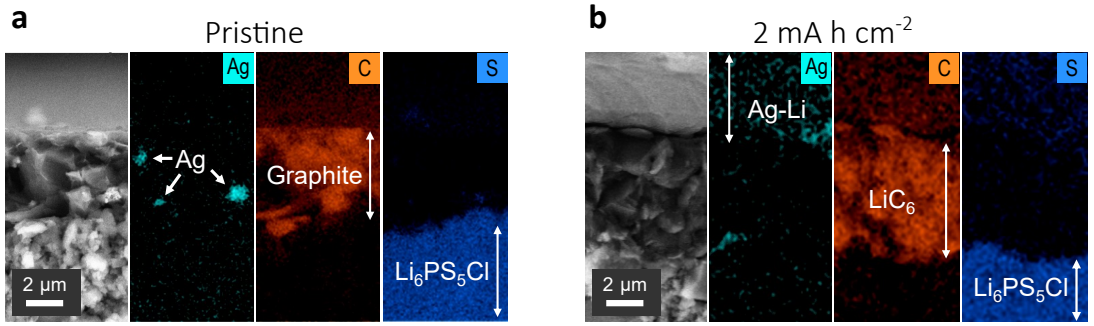


Fig. 6.16: SEM image of the microstructure and corresponding EDX maps of a sprayed Ag-C interlayer on the anodic current collector. (a) before and (b) after plating 2 mA h cm^{-2} at 60 °C. The data was obtained by the help of Dominic Spencer Jolly (Post-doc, University of Oxford).

avoidance of surface roughness-induced short-circuits in the sprayed separators the results highlight the desirability of reducing separator/membrane thickness and the potential for the spray printing approach, especially noting that spray printing has already been demonstrated successfully for ∼10 µm thick inorganic separators in conventional LIBs [182].

SSBs, especially involving interlayers such as Ag-C particulate explored here, naturally lend themselves to manufacture by an incremental layer-by-layer approach, including offering the opportunity for single-step fabrication simply by switching between feedstock suspensions and solutions. For the first time, it has been shown that this approach can also be adopted for air-sensitive materials such as sulfide-based SEs, with both electrolyte dissolution/reprecipitation and suspension routes demonstrated in a specially adapted glovebox. Relatively large areas can be achieved easily and almost instantaneous drying of each layer "freezes"

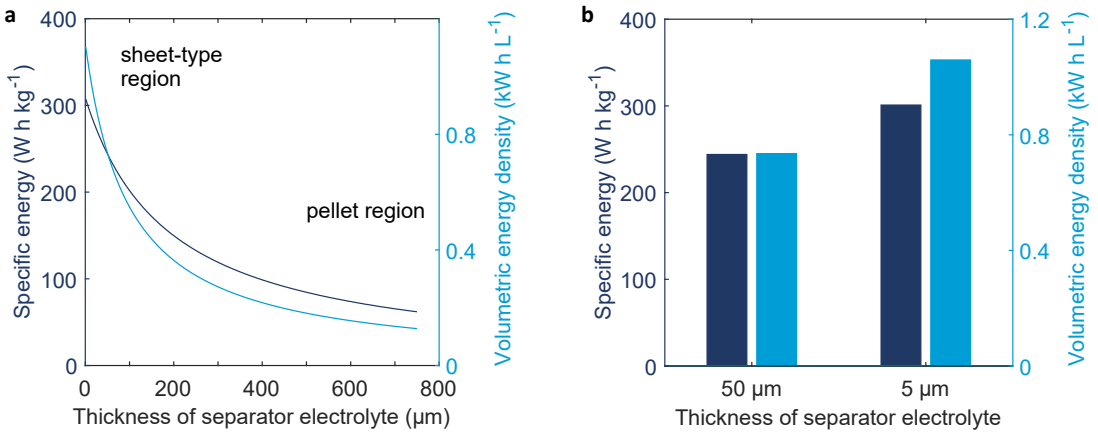


Fig. 6.17: The calculated impact of SE separator thickness on cell specific energy and volumetric energy density assuming a NMC-based cathode and a sprayed Ag-C interlayer of the type shown in Fig. 6.13 (mass of current collectors included). (a) Comparison of thick SE pellet-type and thin SE coating sheet-type formats, and (b) effect of a spray-printed 50 µm or 5 µm thick SE separator on overall cell performance.

its composition providing any re-suspension is avoided (by ensuring the liquid flow rate does not exceed the drying capacity of the heated substrate). In this way, additional spatial compositional control is possible, and limited inter-mixing of discrete layers is ensured. Spray printing is particularly attractive for thin (<50 µm) SE layers between the anode and cathode, which are difficult to produce by other techniques. But it is essential that surface asperities, most typically due to agglomeration of particulates in the feedstock, which lead to short circuits, are avoided. Separately, strategies for suppressing or delaying Li dendrite penetration of these thin SE layers at practical current densities will be needed, and might involve exploring spray printing's ability to produce thin "blocking" layers. Finally, both sprayed composite cathodes and SE separator layers benefit from post-deposition uniaxial compression that increased density, and this step should be incorporated into the workflow under protective environment on the pathway to realizing the scalability of the spray printing approach. In general, the workflow for SSB assembly should, in particular, minimize whenever possible handling or movement of sub-components to avoid cracking and contamination, most particularly large-area, thin SE membrane/separators.

6.3 Conclusions

A scalable layer-by-layer spray printing approach was explored for its potential to manufacture sulfide-based sheet-type SSB formats, including solid electrolyte separators, composite cathodes, and Li metal-free Ag-C nanoparticulate mediated anodes as summarized schematically in Fig. 6.18. Sprayed sulfide solid electrolyte coatings with an area of 10 × 10 cm^2 were readily fabricated as thin as a 10 µm and free of macro-defects, although coatings typically contained a network of fine microcracks in the as-sprayed condition. The morphology, ionic conductivity, and crystallinity of sprayed coatings depended on whether a dissolution/reprecipitation or suspension approach was used, and both provided functioning composite

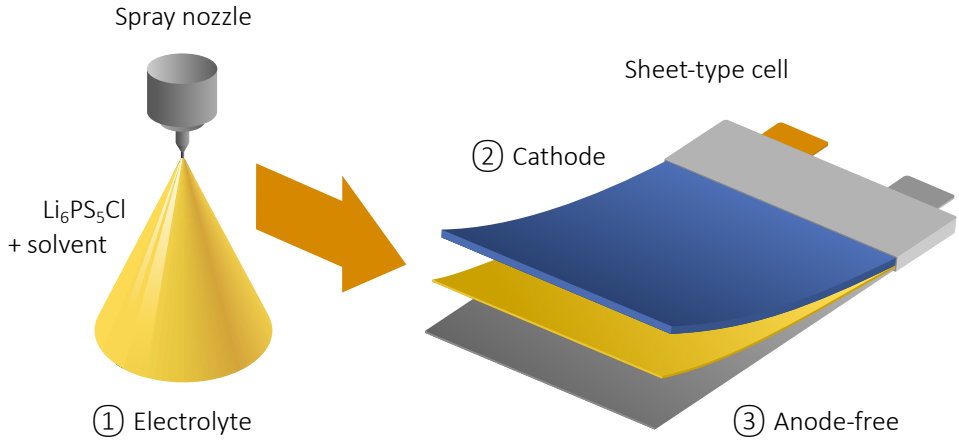


Fig. 6.18: Graphical summary of the spray printing process for the fabrication of sheet-type solid-state battery components such as a sulfide solid electrolyte separator, composite cathode, and anode-free Ag-C layer.

cathodes. Best-performing sulfide coatings had a high ionic conductivity of 1 mS cm^{-1} and were made from an ethyl acetate argyrodite dispersion. A sulfide-based sprayed cathode cycled for 800 cycles with a capacity retention of 63%. A Li metal-free cell was realized with a sprayed Ag-C interlayer to facilitate Li metal plating with a sprayed SE separator, suggesting a promising route for SSB manufacturing.

6.4 Experimental details

Spray mixtures. IPA/LPSCl: 1 g of commercial Li_6PS_5Cl (LPSCl, MSE Supplies) was stirred in 100 mL anhydrous IPA for 1 h. EA/LPSCl: 1 g of commercial LPSCl was suspended in a 100 mL solution of PVDF binder in anhydrous ethyl acetate binder (prepared 1 day earlier and left stirring at 80 °C) for 1h, then mixed and sonicated, giving a PVDF:LPSCl weight ratio of 5:95. Substrates were a 12.5 µm thick stainless steel foil and 0.5 mm thick 5–15 mm diameter stainless steel discs.

Cathode mixtures: Commercial powders of single crystal $LiNi_{0.83}Mn_{0.06}Co_{0.11}O_2$ (NMC, MSE Supplies), LPSCl and carbon black (Sigma-Aldrich) at a ratio of 70:27.5:2.5 by weight were suspended in a EA/PVDF solution, then mixed and sonicated, giving a PVDF:cathode weight ratio of 3:97. Substrate was a 15 µm thick Al foil.

Ag-C coating: A solution of PVDF in a mixture of solvents (97% IPA, 3% NMP by volume) was prepared. Ag nanoparticles and graphite were suspended in this solution in a ratio of 1:3 by weight, then mixed and sonicated, giving the same PVDF:Ag:graphite ratio as that described by Samsung [26]. Substrate was a 12.5 µm thick stainless steel foil. The composite interlayer was composed of 22.5 wt% Ag nanoparticles, 67.5 wt% graphite, and 10 wt% PVDF binder. Electrodes were cut from this sheet using a hollow punch and were uniaxially pressed against Li_6PS_5Cl powder.

Spraying: Spraying was conducted in a custom-made spray tool described in detail in chapter 3.1.4. The suspensions were atomized with compressed Ar gas, and spray-deposited on a metal foil at 110 °C during the deposition to evaporate the solvent. This yielded a 10 × 10 cm^2 sheet of sprayed particulate layers.

Heat treatment. The IPA/LPSCl coating was annealed at 300 °C in a box furnace under an Ar atmosphere (heating/cooling rate: 10 °C min^{-1}, holding temperature: 30 min) to increase ionic conductivity and crystallinity.

Dry Electrode preparation. Commercial powders of LPSCl, SC-NMC, and carbon nanofibers (CNFs, Sigma-Aldrich) were mixed at a weight ratio of 70:27.5:2.5 using pestle and mortar for 15 min. PTFE (Sigma-Aldrich) was suspended and mixed for another 15 min to give a binder:electrode ratio of 1:99 by weight. Further details are provided in chapter 3.1.2.

Scanning electron microscopy (SEM). The SEM analysis of dry composite cathodes was performed in a Zeiss Merlin at an accelerating voltage of 3 kV to

preserve the delicate features of the microstructure that are beam sensitive. In addition, the samples were coated with approximately 4 nm of platinum with a Leica EM ACE200 coating system, in order to avoid any charging on the surface and to improve the image resolution.

Cell Assembly. Cells were assembled and cycled in a custom-designed device described in chapter 3.1.5. All electrochemical tests used a sulfide solid separator of ∼1 mm and had a diameter of 5 mm. Sprayed cathodes were cut from the sprayed sheet using a hollow punch and were uniaxially pressed against Li_6PS_5Cl powder.

Electrochemical measurements. Electrochemical impedance spectroscopy (EIS) was performed in a Gamry Instruments Interface-1000 potentiostat using a voltage amplitude of 10 mV in the frequency range from 1.6 MHz to 0.1 Hz at stack pressure up to 500 MPa. Galvanostatic cycling was performed at a constant current (0.1 mA cm^{-2} to 0.8 mA cm^{-2}) between 4.3 V and 2.5 V at 30, 60 and 80 °C.

Conclusions

7.1 Summary

Cold-pressed single crystal (SC) Li-Ni-Mn-Co oxide (NMC)/argyrodite sulfide solid electrolyte (SE) composite cathodes for SSBs were developed that showed a high first cycle coulombic efficiency of >85% and a high discharge capacity of 210 mA h g^{-1} at 30 °C. Capacity in the SC-NMC faded mainly due to mechanical debonding at the NMC/sulfide SE interface in contrast to the commonly used polycrystalline (PC) NMC where anisotropic volume change during Li de/intercalation caused notable internal cathode active material (CAM) fracture. The stack pressure of the composite cathode was lowered as much as possible by an asymmetric mechanical load to explore a more realistic condition, and even at 0.2 MPa, almost full theoretical capacity (210 mA h g^{-1}) could be transferred to/from the cathode in the voltage range 2.5–4.3 V vs. Li^+/Li, despite the volume expansion of 5.5% during charge/discharge.

The excellent performance of the SC-NMC cathode was ascribed to the composite microstructure that had a low porosity with maximized NMC/LPSCl physical surface interaction and interfacial contact. The robustness of the SC-NMC also proved to be beneficial during cell fabrication, where particles remained intact after experiencing high friction and impact forces during mixing and subsequent densification at a uniaxial pressure of 500 MPa. PC-NMC active particles showed severe intergranular fracture even at 250 MPa, which resulted in pulverized CAM, which was often isolated from other ionically or electronically conducting particles. There were no visible cracks in the PC-NMC particles only at a fabrication

pressure of 50 MPa, which is arguably not sufficiently high to fabricate dense composite cathodes with low interfacial resistance. The advantages highlighted during manufacturing and cycling make SC particles the CAM of choice for SSBs where the mechanical integrity of the microstructure is even more important for long-lasting cyclability than for LIBs since particle debonding cannot be mitigated due to the lack of liquid electrolyte.

The intrinsic fast-charging capability of an evolution of this type of SSB was then studied. A more considered cathode architecture and operating window was designed to match the high demands during fast charging. Using a list of criteria, a 70 µm thick solid-state cathode was fabricated that could be cycled at a very high charge current density of 15 mA cm^{-2} (4.8 C), and retained a high discharge capacity of 150 mA h g^{-1} (71% active material utilization) at a charging time of only ∼8 min at 30 °C and 2.5–4.3 V vs. Li^+/Li. The high intrinsic cathode performance was revealed in a 3-electrode set-up specifically developed for a rate test that allowed for accurate cathode voltage measurement versus a Li reference electrode.

Fast charging at ∼5 C was demonstrated for 3000 cycles at 30 °C with 81% active capacity retention. There was only small capacity fading per cycle, despite the high charge current density and thermodynamic instability of the SE. 3D microstructural analysis of the cathode showed that there was relatively slow and slight, progressive pore volume increase and any active particle isolation played only a small role in capacity fading. Fast charging was also investigated on thicker (210 µm) cathodes using an areal loading of 45 mg cm^{-2} which was much higher than usually used in commercial LIBs. When the temperature was increased to 80 °C, a charge current density of 50 mA cm^{-2} and a charge time of ∼10 min could be sustained at an areal capacity of 8 mA h cm^{-2} (85% active material utilization). It was demonstrated that these cathodes could be used in pellet form

SSBs to provide a cell energy density of 400 W h kg^{-1} in a charging time of 1 h (15 mA cm^{-2}) and 10 min (50 mA cm^{-2}) at 30 °C and 80 °C, respectively, assuming a thin (20 µm) SE separator and a Li foil as anode. The combination of a carefully optimized cathode architecture of high as-manufactured density and well-dispersed active particles in intimate contact with the SE, and the implementation of a 3-electrode arrangement, showed that sulfide-based composite cathodes in SSBs can operate better than previously thought.

For the potential production of thin, large-area, and practical sheet-type SSBs (as opposed to pellet-type), the technical feasibility of spraying a sulfide SE in a scalable layer-by-layer approach was explored. The spray printing approach was successfully implemented, as a proof of principle, to manufacture sulfide-based sheet-type SSB formats, including SE separators, composite cathodes, and a Li metal-free Ag-C nanoparticulate mediated anode. Sprayed sulfide SE coatings had an area of 10 × 10 cm^2 and were readily fabricated as thin as 10 µm. The morphology, ionic conductivity, and crystallinity of sprayed coatings depended on whether a dissolution/reprecipitation or suspension approach was used. There were characteristic fine drying surface cracks and high porosities (∼30%) in the coating made from a mixture of IPA/sulfide and EA/sulfide, respectively. Best performing sulfide coatings had a high ionic conductivity of 1 mS cm^{-1} and were made from a mixture of ethyl acetate with dissolved PVDF as binder and dispersed argyrodite. A sulfide-based sprayed cathode made from the better-performing solvent cycled for 800 cycles with a capacity retention of 63%. Finally, it was demonstrated that spray printing was capable of fabricating a functional Ag-C interlayer to facilitate Li metal plating in a Li metal anode-free cell design. The possibility of subsequent spraying of different coatings, for example, the Ag-C layer immediately followed by an argyrodite layer, demonstrated the potential for process integration, and the benefits of a sprayed sheet-type cell were discussed. The spray printing process in a new, fully inert atmosphere provided a flexible

platform for fabrication of SE particulate coatings with promising application to sulfide-based SSBs.

7.2 Future work

SSB composite cathodes will benefit from further progress in the development of novel CAMs. Micrometer-sized SC-NMC with increased Ni content was scarcely available in the beginning of this project but is now becoming more popular and has reached commercialization. Future work should now involve these new NMCs, for example, with a higher Ni or lower Co concentration, which could potentially improve sustainability aspects of SSBs. It is also noteworthy to mention that commercial SC-NMC is often agglomerated and a more uniform CAM particle distribution, and reliable dispersion, might lead to enhanced performance. This thesis showed that it is possible to realize close to theoretical capacity of NMC cathodes, despite a volume change of 6%, although in general there remains a need for CAMs with lower volume change for improved cyclability particularly when full capacity is required. The low stack pressure of 0.2 MPa that was realized in an asymmetric set-up in this thesis might be applied on larger and thinner sheet-type cells. Although the asymmetric arrangement shown herein is probably limited to pellet-type cells, the low axial load suggests that composite cathodes consisting of an optimized and dense microstructure that undergo only a limited volume change can be realized, perhaps only a low stack pressure will be sufficient.

Results shown herein demonstrated that a very high current density of 15 mA cm^{-2} can be used at room temperature with high CAM utilization in small pellet-type cells. Future work should focus on how fast-charging performance may be translated to larger area SSB cathodes. The addition of a polymer binder that is likely necessary in the fabrication process might lead to a worse performance due to increased resistance, but recent work suggests the binder fraction might be kept at <1 wt% using a dry process approach that relies on thin PTFE fibrils. Even

though capacity fading was relatively slow over 3000 cycles, further improvements in cycle life may be achieved by CAM coatings, which could also improve calendar life. The thesis further suggests that Li-In is a suitable anode, particularly for a matching cathode investigation that requires a high current density, and other alloys might be explored more carefully, especially at different Li concentrations. The 3-electrode set-up developed here played a critical role in probing the actual rate performance of the cathode in detail and should be applied more often in the field of SSBs to separate interfering processes, and to report voltages more precisely to a known reference.

Spray printing in an inert atmosphere might be further applied to fabricate ionically conducting separators made of two or more layered coatings that combine different qualities, for example, stability at high electrochemical potentials on the cathode side and high stability with Li on the anode side. Especially, recently developed halide SEs with high ionic conductivity have shown good electrochemical stability with CAMs operating at high voltage but had insufficient stability with Li metal. The spray printing approach would offer the possibility to add a highly conductive sulfide layer to protect halide degradation on the anode side. Future work could therefore focus on the exploration of suitable solvents for the spray deposition of halide SEs. The layered approach also allows for exploration of materials that might have a better contact with Li and possibly increase the critical current density similarly to a recent study that used a separator made of sulfide SE and lithium phosphorus oxynitride (LiPON) [191]. Another manufacturing option could be to explore dendrite mitigating layers, for instance by using different polymers that might increase the integrity of the separator to counteract crack formation during plating [192].

There is an opportunity to use the developed spray printing process for making sulfide-based cathodes with a graded microstructure that matches local require-

ments such as adjusted binder amount at different interfaces. High-performance cathode architectures might be fabricated by using ionically conductive polymer because it might be difficult to reduce the Li-ion blocking of inert binders at higher fraction. Thicker cathodes might be explored by the spraying process for high energy density applications as the layer-by-layer approach confines thin layers to be dried almost instantly after depositing which avoids crack formation regularly observed in other methods such as slurry casting.

The Ag-C particulate coatings described here suggest promise for future anode-free SSBs. The working mechanism of the Ag-C layer is not yet fully understood (and beyond the scope of the thesis), but the spray process provides a very flexible platform to explore different materials (and their combination). A follow-up study could focus on the investigation of different carbons and other Li alloying nanoparticles such as Zn as an alternative to Ag.

Finally, another strength of the spray process is to combine different coatings with one another. A promising and efficient route could be to spray print first a Ag-C layer with a subsequent SE separator made of one or more coatings as mentioned above. Much thicker cathodes e.g. made from a dry process could then be stacked with the sprayed layers to fabricate an energy-dense SSB. Future work would need to focus on making such sheet-type SSBs at larger scale. The combination of several sprayed coatings might require a flattening or densification step in between spraying to avoid surface asperities or cracks causing short circuits in thin layers.

References

[1] S. Grzesiak and A. Sulich, "Car Engines Comparative Analysis: Sustainable Approach," *Energies*, vol. 15, no. 14, 2022.

[2] M. Mascal and E. B. Nikitin, "Direct, High-Yield Conversion of Cellulose into Biofuel," *Angewandte Chemie*, vol. 120, no. 41, pp. 8042–8044, 2008.

[3] T. Wilberforce, Z. El-Hassan, F. N. Khatib, A. Al Makky, A. Baroutaji, J. G. Carton, and A. G. Olabi, "Developments of electric cars and fuel cell hydrogen electric cars," *International Journal of Hydrogen Energy*, vol. 42, no. 40, pp. 25695–25734, 2017.

[4] J. A. Sanguesa, V. Torres-Sanz, P. Garrido, F. J. Martinez, and J. M. Marquez-Barja, "A review on electric vehicles: Technologies and challenges," *Smart Cities*, vol. 4, no. 1, pp. 372–404, 2021.

[5] M. V. Reddy, A. Mauger, C. M. Julien, A. Paolella, and K. Zaghib, "Brief history of early lithium-battery development," *Materials*, vol. 13, no. 8, 2020.

[6] K. Mizushima, P. Jones, P. Wiseman, and J. Goodenough, "A New Cathode Material For Batteries Of High Energy Density," *Mat. Res. Bull.*, vol. 15, pp. 783–789, 1980.

[7] X. Sun, M. Ouyang, and H. Hao, "Surging lithium price will not impede the electric vehicle boom," *Joule*, vol. 6, no. 8, pp. 1738–1742, 2022.

[8] S. O'Neill, "Electric Air Taxis Create Megadeal Buzz," *Engineering*, vol. 13, pp. 5–8, 2022.

[9] M. J. Welfens, J. Nordmann, and A. Seibt, "Drivers and barriers to return and recycling of mobile phones. Case studies of communication and collection campaigns," *Journal of Cleaner Production*, vol. 132, pp. 108–121, 2016.

[10] Y. Liang, C. Z. Zhao, H. Yuan, Y. Chen, W. Zhang, J. Q. Huang, D. Yu, Y. Liu, M. M. Titirici, Y. L. Chueh, H. Yu, and Q. Zhang, "A review of rechargeable batteries for portable electronic devices," *InfoMat*, vol. 1, no. 1, pp. 6–32, 2019.

[11] D. Carlstedt and L. E. Asp, "Performance analysis framework for structural battery composites in electric vehicles," *Composites Part B: Engineering*, vol. 186, p. 107822, 2020.

[12] M. Ragone, V. Yurkiv, A. Ramasubramanian, B. Kashir, and F. Mashayek, "Data driven estimation of electric vehicle battery state-of-charge informed by automotive simulations and multi-physics modeling," *Journal of Power Sources*, vol. 483, p. 229108, 2021.

[13] J. Janek and W. G. Zeier, "A Solid Future for Battery Development," *Nature Energy*, vol. 1, no. 9, pp. 1–4, 2016.

[14] J. Betz, G. Bieker, P. Meister, T. Placke, M. Winter, and R. Schmuch, "Theoretical versus Practical Energy: A Plea for More Transparency in the Energy Calculation of Different Rechargeable Battery Systems," *Advanced Energy Materials*, vol. 9, no. 6, p. 1803170, 2018.

[15] P. G. Bruce, S. A. Freunberger, L. J. Hardwick, and J. M. Tarascon, "Li-O_2 and Li-S batteries with high energy storage," *Nature Materials*, vol. 11, no. 1, pp. 19–29, 2012.

[16] J. B. Goodenough and K.-s. Park, "The Li-Ion Rechargeable Battery : A Perspective," *Journal of the American Ceramic Society*, vol. 135, pp. 1167–1176, 2013.

[17] Y.-K. Sun, "Future of Electrochemical Energy Storage," *ACS Energy Letters*, vol. 2, no. 3, pp. 716–716, 2017.

[18] Y. Seino, T. Ota, K. Takada, A. Hayashi, and M. Tatsumisago, "A sulphide lithium super ion conductor is superior to liquid ion conductors for use in rechargeable batteries," *Energy and Environmental Science*, vol. 7, no. 2, pp. 627–631, 2014.

[19] J. Kasemchainan and P. G. Bruce, "All-Solid-State Batteries and their Remaining Challenges A potential route towards safer, higher performing batteries," *Johnson Matthey Technology Review*, vol. 62, no. 2, pp. 177–180, 2018.

[20] Y. Kato, S. Hori, T. Saito, K. Suzuki, M. Hirayama, A. Mitsui, M. Yonemura, H. Iba, and R. Kanno, "High-power all-solid-state batteries using sulfide superionic conductors," *Nature Energy*, vol. 1, no. 4, p. 16030, 2016.

[21] J. Schnell, T. Günther, T. Knoche, C. Vieider, L. Köhler, A. Just, M. Keller, S. Passerini, and G. Reinhart, "All-Solid-State Lithium-Ion and Lithium Metal Batteries – Paving the Way to Large-Scale Production," *Journal of Power Sources*, vol. 382, pp. 160–175, 2018.

[22] J. Kasemchainan, S. Zekoll, D. Spencer Jolly, Z. Ning, G. O. Hartley, T. J. Marrow, and P. G. Bruce, "Critical Stripping Current Leads to Dendrite Formation on Plating in Lithium Anode Solid Electrolyte Cells," *Nature Materials*, vol. 18, pp. 1105–1111, 2019.

[23] D. Spencer Jolly, Z. Ning, G. O. Hartley, B. Liu, D. L. R. Melvin, P. Adamson, J. Marrow, and P. G. Bruce, "Temperature Dependence of Lithium Anode Voiding in Argyrodite Solid-State Batteries," *ACS Applied Materials & Interfaces*, vol. 13, no. 19, pp. 22708–22716, 2021.

[24] J. A. Lewis, K. A. Cavallaro, Y. Liu, and M. T. McDowell, "The promise of alloy anodes for solid-state batteries," *Joule*, vol. 6, no. 7, pp. 1418–1430, 2022.

[25] A. L. Santhosha, L. Medenbach, J. R. Buchheim, and P. Adelhelm, "The Indium-Lithium Electrode in Solid-State Lithium-Ion Batteries: Phase Formation, Redox Potentials, and Interface Stability," *Batteries & Supercaps*, vol. 2, no. 6, pp. 524–529, 2019.

[26] Y.-g. Lee, S. Fujiki, C. Jung, N. Suzuki, N. Yashiro, R. Omoda, D.-s. Ko, T. Shiratsuchi, T. Sugimoto, S. Ryu, J. H. Ku, T. Watanabe, Y. Park, Y. Aihara, D. Im, and I. T. Han, "High-energy long-cycling all-solid-state lithium metal batteries enabled by silver – carbon composite anodes," *Nature Energy*, vol. 5, pp. 299–308, 2020.

[27] J. B. Goodenough and Y. Kim, "Challenges for Rechargeable Li Batteries," *Chem. Mater.*, vol. 22, no. 3, pp. 587–603, 2010.

[28] X. Yao, B. Huang, J. Yin, G. Peng, Z. Huang, C. Gao, D. Liu, and X. Xu, "All-solid-state lithium batteries with inorganic solid electrolytes: Review of fundamental science," *Chinese Physics B*, vol. 25, no. 1, p. 018802, 2015.

[29] S. Chen, D. Xie, G. Liu, J. P. Mwizerwa, Q. Zhang, Y. Zhao, X. Xu, and X. Yao, "Sulfide solid electrolytes for all-solid-state lithium batteries: Structure, conductivity, stability and application," *Energy Storage Materials*, vol. 14, pp. 58–74, 2018.

[30] H. J. Deiseroth, S. T. Kong, H. Eckert, J. Vannahme, C. Reiner, T. Zaiß, and M. Schlosser, "Li_6PS_5X: A class of crystalline Li-rich solids with an unusually high Li^+ mobility," *Angewandte Chemie - International Edition*, vol. 47, no. 4, pp. 755–758, 2008.

[31] R. P. Rao and S. Adams, "Studies of lithium argyrodite solid electrolytes for all-solid-state batteries," *physica status solidi (a)*, vol. 208, no. 8, pp. 1804–1807, 2011.

[32] S. Boulineau, M. Courty, J. M. Tarascon, and V. Viallet, "Mechanochemical synthesis of Li-argyrodite Li_6PS_5X (X = Cl, Br, I) as sulfur-based solid electrolytes for all solid state batteries application," *Solid State Ionics*, vol. 221, pp. 1–5, 2012.

[33] C. Yu, S. Ganapathy, J. Hageman, L. Van Eijck, E. R. Van Eck, L. Zhang, T. Schwietert, S. Basak, E. M. Kelder, and M. Wagemaker, "Facile Synthesis toward the Optimal Structure-Conductivity Characteristics of the Argyrodite Li_6PS_5Cl Solid-State Electrolyte," *ACS Applied Materials and Interfaces*, vol. 10, no. 39, pp. 33296–33306, 2018.

[34] A. Miura, N. C. Rosero-Navarro, A. Sakuda, K. Tadanaga, N. H. H. Phuc, A. Matsuda, N. Machida, A. Hayashi, and M. Tatsumisago, "Liquid-phase syntheses of sulfide electrolytes for all-solid-state lithium battery," *Nature Reviews Chemistry*, vol. 3, pp. 189–198, 2019.

[35] L. Zhou, K.-H. Park, X. Sun, F. Lalére, T. Adermann, P. Hartmann, and L. F. Nazar, "Solvent-Engineered Design of Argyrodite," *ACS Energy Letters*, vol. 4, pp. 265–270, 2019.

[36] F. Stadler and C. Fietzek, "Crystalline Halide Substituted Li-Argyrodites as Solid Electrolytes for Lithium Secondary Batteries," *ECS Transactions*, vol. 25, no. 36, pp. 177–183, 2010.

[37] Z. Zhang, L. Zhang, Y. Liu, C. Yu, X. Yan, B. Xu, and L. min Wang, "Synthesis and characterization of argyrodite solid electrolytes for all-solid-state Li-ion batteries," *Journal of Alloys and Compounds*, vol. 747, pp. 227–235, 2018.

[38] C. Wang, Y. Gong, B. Liu, K. Fu, Y. Yao, E. Hitz, Y. Li, J. Dai, S. Xu, W. Luo, E. D. Wachsman, and L. Hu, "Conformal, Nanoscale ZnO Surface Modification of Garnet-Based Solid-State Electrolyte for Lithium Metal Anodes," *Nano Letters*, vol. 17, no. 1, pp. 565–571, 2017.

[39] Y. Zhu, X. He, and Y. Mo, "Origin of Outstanding Stability in the Lithium Solid Electrolyte Materials: Insights from Thermodynamic Analyses Based on First-Principles Calculations," *ACS Applied Materials and Interfaces*, vol. 7, no. 42, pp. 23685–23693, 2015.

[40] S. Wenzel, S. J. Sedlmaier, C. Dietrich, W. G. Zeier, and J. Janek, "Interfacial Reactivity and Interphase Growth of Argyrodite Solid Electrolytes at Lithium Metal Electrodes," *Solid State Ionics*, vol. 318, pp. 102–112, 2018.

[41] F. Han, Y. Zhu, X. He, Y. Mo, and C. Wang, "Electrochemical Stability of $Li_{10}GeP_2S_{12}$ and $Li_7La_3Zr_2O_{12}$ Solid Electrolytes," *Advanced Energy Materials*, vol. 6, no. 8, p. 1501590, 2016.

[42] Q. Liu, Z. Geng, C. Han, Y. Fu, S. Li, Y. bing He, F. Kang, and B. Li, "Challenges and perspectives of garnet solid electrolytes for all solid-state lithium batteries," *Journal of Power Sources*, vol. 389, pp. 120–134, 2018.

[43] J. L. Allen, J. Wolfenstine, E. Rangasamy, and J. Sakamoto, "Effect of substitution (Ta, Al, Ga) on the conductivity of $Li_7La_3Zr_2O_12$," *Journal of Power Sources*, vol. 206, pp. 315–319, 2012.

[44] E. Rangasamy, J. Wolfenstine, and J. Sakamoto, "The role of Al and Li concentration on the formation of cubic garnet solid electrolyte of nominal composition $Li_7La_3Zr_2O_{12}$," *Solid State Ionics*, vol. 206, pp. 28–32, 2012.

[45] T. Thompson, S. Yu, L. Williams, R. D. Schmidt, R. Garcia-Mendez, J. Wolfenstine, J. L. Allen, E. Kioupakis, D. J. Siegel, and J. Sakamoto, " Electrochemical Window of the Li-Ion Solid Electrolyte $Li_7La_3Zr_2O_{12}$," *ACS Energy Letters*, vol. 2, no. 2, pp. 462–468, 2017.

[46] S. Ohta, T. Kobayashi, and T. Asaoka, "High lithium ionic conductivity in the garnet-type oxide $Li_{7-X}La_3(Zr_{2-X}, Nb_X)O_{12}$ (X = 0-2)," *Journal of Power Sources*, vol. 196, no. 6, pp. 3342–3345, 2011.

[47] K. Nie, Y. Hong, J. Qiu, Q. Li, X. Yu, H. Li, and L. Chen, "Interfaces Between Cathode and Electrolyte in Solid State Lithium Batteries: Challenges and Perspectives," *Frontiers in Chemistry*, vol. 6, pp. 1–19, 2018.

[48] F. Strauss, T. Bartsch, L. De Biasi, A. Y. Kim, J. Janek, P. Hartmann, and T. Brezesinski, "Impact of Cathode Material Particle Size on the Capacity of Bulk-Type All-Solid-State Batteries," *ACS Energy Letters*, vol. 3, no. 4, pp. 992–996, 2018.

[49] T. Shi, Q. Tu, Y. Tian, Y. Xiao, L. J. Miara, O. Kononova, and G. Ceder, "High Active Material Loading in All-Solid-State Battery Electrode via Particle Size Optimization," *Advanced Energy Materials*, vol. 10, no. 1, p. 1902881, 2020.

[50] A. Bielefeld, D. A. Weber, and J. Janek, "Modeling Effective Ionic Conductivity and Binder Influence in Composite Cathodes for All-Solid-State Batteries.," *ACS applied materials & interfaces*, vol. 12, pp. 12821–12833, 2020.

[51] K. Takada, "Progress in solid electrolytes toward realizing solid-state lithium batteries," *Journal of Power Sources*, vol. 394, pp. 74–85, 2018.

[52] S. H. Jung, K. Oh, Y. J. Nam, D. Y. Oh, P. Brüner, K. Kang, and Y. S. Jung, "Li_3BO_3-Li_2CO_3: Rationally Designed Buffering Phase for Sulfide All-Solid-State Li-Ion Batteries," *Chemistry of Materials*, vol. 30, no. 22, pp. 8190–8200, 2018.

[53] Y. S. Jung, D. Y. Oh, Y. J. Nam, and K. H. Park, "Issues and challenges for bulk-type all-solid-state rechargeable lithium batteries using sulfide solid electrolytes," *Israel Journal of Chemistry*, vol. 55, no. 5, pp. 472–485, 2015.

[54] K. Kerman, A. Luntz, V. Viswanathan, Y.-M. Chiang, and Z. Chen, "Review—Practical Challenges Hindering the Development of Solid State Li Ion Batteries," *Journal of The Electrochemical Society*, vol. 164, no. 7, pp. A1731–A1744, 2017.

[55] F. Hao, F. Han, Y. Liang, C. Wang, and Y. Yao, "Architectural design and fabrication approaches for solid-state batteries," *MRS Bulletin*, vol. 43, no. 10, pp. 775–781, 2018.

[56] K. H. Park, Q. Bai, D. H. Kim, D. Y. Oh, Y. Zhu, Y. Mo, and Y. S. Jung, "Design Strategies, Practical Considerations, and New Solution Processes of Sulfide Solid Electrolytes for All-Solid-State Batteries," *Advanced Energy Materials*, vol. 8, no. 18, p. 1800035, 2018.

[57] A. Sakuda, A. Hayashi, and M. Tatsumisago, "Sulfide solid electrolyte with favorable mechanical property for all-solid-state lithium battery," *Scientific Reports*, vol. 3, pp. 2–6, 2013.

[58] Y. Kim, H. Jo, J. L. Allen, H. Choe, J. Wolfenstine, and J. Sakamoto, "The Effect of Relative Density on the Mechanical Properties of Hot-Pressed Cubic $Li_7La_3Zr_2O_{12}$," *Journal of the American Ceramic Society*, vol. 99, no. 4, pp. 1367–1374, 2016.

[59] S. Troy, A. Schreiber, T. Reppert, H. G. Gehrke, M. Finsterbusch, S. Uhlenbruck, and P. Stenzel, "Life Cycle Assessment and resource analysis of all-solid-state batteries," *Applied Energy*, vol. 169, pp. 757–767, 2016.

[60] N. C. Rosero-Navarro, T. Yamashita, A. Miura, M. Higuchi, and K. Tadanaga, "Effect of Sintering Additives on Relative Density and Li-ion Conductivity of Nb-Doped $Li_7La_3ZrO_{12}$ Solid Electrolyte," *Journal of the American Ceramic Society*, vol. 100, no. 1, pp. 276–285, 2017.

[61] G. T. Hitz, D. W. McOwen, L. Zhang, Z. Ma, Z. Fu, Y. Wen, Y. Gong, J. Dai, T. R. Hamann, L. Hu, and E. D. Wachsman, "High-rate lithium cycling in a scalable trilayer Li-garnet-electrolyte architecture," *Materials Today*, vol. 22, pp. 50–57, 2018.

[62] Y. Ren, T. Liu, Y. Shen, Y. Lin, and C. W. Nan, "Chemical compatibility between garnet-like solid state electrolyte $Li_{6.75}La_3Zr_{1.75}Ta_{0.25}O_{12}$ and major commercial lithium battery cathode materials," *Journal of Materiomics*, vol. 2, no. 3, pp. 256–264, 2016.

[63] A. Aboulaich, R. Bouchet, G. Delaizir, V. Seznec, L. Tortet, M. Morcrette, P. Rozier, J. M. Tarascon, V. Viallet, and M. Dollé, "A new approach to develop safe all-inorganic monolithic li-ion batteries," *Advanced Energy Materials*, vol. 1, no. 2, pp. 179–183, 2011.

[64] C. L. Tsai, Q. Ma, C. Dellen, S. Lobe, F. Vondahlen, A. Windmüller, D. Grüner, H. Zheng, S. Uhlenbruck, M. Finsterbusch, F. Tietz, D. Fattakhova-Rohlfing, H. P. Buchkremer, and O. Guillon, "A garnet structure-based all-solid-state Li battery without interface modification: Resolving incompatibility issues on positive electrodes," *Sustainable Energy and Fuels*, vol. 3, no. 1, pp. 280–291, 2019.

[65] F. Schipper, E. M. Erickson, C. Erk, J.-Y. Shin, F. F. Chesneau, and D. Aurbach, "Review—Recent Advances and Remaining Challenges for Lithium Ion Battery Cathodes," *Journal of The Electrochemical Society*, vol. 164, no. 1, pp. A6220–A6228, 2017.

[66] R. Koerver, W. Zhang, L. De Biasi, S. Schweidler, A. O. Kondrakov, S. Kolling, T. Brezesinski, P. Hartmann, W. G. Zeier, and J. Janek, "Chemo-Mechanical Expansion of Lithium Electrode Materials – on the Route to Mechanically Optimized All-Solid-State Batteries," *Energy and Environmental Science*, vol. 11, no. 8, pp. 2142–2158, 2018.

[67] A. Hayashi, A. Sakuda, and M. Tatsumisago, "Development of Sulfide Solid Electrolytes and Interface Formation Processes for Bulk-Type All-Solid-State Li and Na Batteries," *Frontiers in Energy Research*, vol. 4, pp. 1–13, 2016.

[68] W. Zhang, D. Schröder, T. Arlt, I. Manke, R. Koerver, R. Pinedo, D. A. Weber, J. Sann, W. G. Zeier, and J. Janek, "(Electro)chemical expansion during cycling: Monitoring the pressure changes in operating solid-state lithium batteries," *Journal of Materials Chemistry A*, vol. 5, no. 20, pp. 9929–9936, 2017.

[69] H. Muramatsu, A. Hayashi, T. Ohtomo, S. Hama, and M. Tatsumisago, "Structural change of Li_2S-P_2S_5 sulfide solid electrolytes in the atmosphere," *Solid State Ionics*, vol. 182, no. 1, pp. 116–119, 2011.

[70] A. Hayashi, H. Muramatsu, T. Ohtomo, S. Hama, and M. Tatsumisago, "Improvement of chemical stability of Li_3PS_4 glass electrolytes by adding MxOy (M = Fe, Zn, and Bi) nanoparticles," *Journal of Materials Chemistry A*, vol. 1, no. 21, pp. 6320–6326, 2013.

[71] Y. J. Nam, D. Y. Oh, S. H. Jung, and Y. S. Jung, "Toward practical all-solid-state lithium-ion batteries with high energy density and safety: Comparative study for electrodes fabricated by dry- and slurry-mixing processes," *Journal of Power Sources*, vol. 375, pp. 93–101, 2018.

[72] L. Cheng, H. Hou, S. Lux, R. Kostecki, R. Davis, V. Zorba, A. Mehta, and M. Doeff, "Enhanced lithium ion transport in garnet-type solid state electrolytes," *Journal of Electroceramics*, vol. 38, no. 2-4, pp. 168–175, 2017.

[73] M. A. Kraft, S. P. Culver, M. Calderon, F. Böcher, T. Krauskopf, A. Senyshyn, C. Dietrich, A. Zevalkink, J. Janek, and W. G. Zeier, "Influence of Lattice Polarizability on the Ionic Conductivity in the Lithium Superionic Argyrodites Li_6PS_5X (X = Cl, Br, I)," *Journal of the American Chemical Society*, vol. 139, no. 31, pp. 10909–10918, 2017.

[74] S. Cao, S. Song, X. Xiang, Q. Hu, C. Zhang, Z. Xia, and Y. Xu, "Modeling, Preparation, and Elemental Doping of $Li_7La_3Zr_2O_{12}$ Garnet-Type Solid Electrolytes: A Review," *Journal of the Korean Ceramic Society*, vol. 56, no. 2, pp. 111–129, 2019.

[75] R. M. Pasquarelli, D. S. Ginley, and R. O'Hayre, "Solution processing of transparent conductors: from flask to film," *Chem. Soc. Rev.*, vol. 40, pp. 5406–5441, 2011.

[76] M. Schmitt, P. Scharfer, and W. Schabel, "Slot die coating of lithium-ion battery electrodes: Investigations on edge effect issues for stripe and pattern coatings," *Journal of Coatings Technology and Research*, vol. 11, no. 1, pp. 57–63, 2014.

[77] J. Li, B. L. Armstrong, C. Daniel, J. Kiggans, and D. L. Wood, "Optimization of multicomponent aqueous suspensions of lithium iron phosphate ($LiFePO_4$) nanoparticles and carbon black for lithium-ion battery cathodes," *Journal of Colloid and Interface Science*, vol. 405, pp. 118–124, 2013.

[78] M. Singh, J. Kaiser, and H. Hahn, "A systematic study of thick electrodes for high energy lithium ion batteries," *Journal of Electroanalytical Chemistry*, vol. 782, no. 7, pp. 245–249, 2016.

[79] D. L. Wood, J. Li, and C. Daniel, "Prospects for reducing the processing cost of lithium ion batteries," *Journal of Power Sources*, vol. 275, pp. 234–242, 2015.

[80] N. Singh, C. Galande, A. Miranda, A. Mathkar, W. Gao, A. L. M. Reddy, A. Vlad, and P. M. Ajayan, "Paintable battery," *Scientific Reports*, vol. 2, pp. 6–10, 2012.

[81] C. Huang, N. P. Young, J. Zhang, H. J. Snaith, and P. S. Grant, "A two layer electrode structure for improved Li Ion diffusion and volumetric capacity in Li Ion batteries," *Nano Energy*, vol. 31, pp. 377–385, 2017.

[82] S. H. Lee, A. Mahadevegowda, C. Huang, J. D. Evans, and P. S. Grant, "Spray printing of self-assembled porous structures for high power battery electrodes," *Journal of Materials Chemistry A*, vol. 6, no. 27, pp. 13133–13141, 2018.

[83] K. H. Choi, D. B. Ahn, and S. Y. Lee, "Current Status and Challenges in Printed Batteries: Toward Form Factor-Free, Monolithic Integrated Power Sources," *ACS Energy Letters*, vol. 3, no. 1, pp. 220–236, 2018.

[84] C. Reyes, R. Somogyi, S. Niu, M. A. Cruz, F. Yang, M. J. Catenacci, C. P. Rhodes, and B. J. Wiley, "Three-Dimensional Printing of a Complete Lithium Ion Battery with Fused Filament Fabrication," *ACS Applied Energy Materials*, vol. 1, no. 10, pp. 5268–5279, 2018.

[85] L. J. Deiner and T. L. Reitz, "Inkjet and Aerosol Jet Printing of Electrochemical Devices for Energy Conversion and Storage," *Advanced Engineering Materials*, vol. 19, no. 7, p. 1600878, 2017.

[86] T. Kato, S. Iwasaki, Y. Ishii, M. Motoyama, W. C. West, Y. Yamamoto, and Y. Iriyama, "Preparation of thick-film electrode-solid electrolyte composites on $Li_7La_3Zr_2O_{12}$ and their electrochemical properties," *Journal of Power Sources*, vol. 303, pp. 65–72, 2016.

[87] D. Hanft, J. Exner, and R. Moos, "Thick-films of garnet-type lithium ion conductor prepared by the Aerosol Deposition Method: The role of morphology and annealing treatment on the ionic conductivity," *Journal of Power Sources*, vol. 361, pp. 61–69, 2017.

[88] C. Cheng, R. Drummond, S. R. Duncan, and P. S. Grant, "Micro-scale graded electrodes for improved dynamic and cycling performance of Li-ion batteries," *Journal of Power Sources*, vol. 413, no. November 2018, pp. 59–67, 2019.

[89] A. Sakuda, K. Kuratani, M. Yamamoto, M. Takahashi, T. Takeuchi, and H. Kobayashi, "All-Solid-State Battery Electrode Sheets Prepared by a Slurry Coating Process," *Journal of The Electrochemical Society*, vol. 164, no. 12, pp. A2474–A2478, 2017.

[90] T. Pichonat, C. Lethien, N. Tiercelin, S. Godey, E. Pichonat, P. Roussel, M. Colmont, and P. A. Rolland, "Further studies on the lithium phosphorus oxynitride solid electrolyte," *Materials Chemistry and Physics*, vol. 123, no. 1, pp. 231–235, 2010.

[91] S. Sicolo, M. Fingerle, R. Hausbrand, and K. Albe, "Interfacial instability of amorphous LiPON against lithium: A combined Density Functional Theory and spectroscopic study," *Journal of Power Sources*, vol. 354, pp. 124–133, 2017.

[92] D. Y. Oh, Y. J. Nam, K. H. Park, S. H. Jung, S. J. Cho, Y. K. Kim, Y. G. Lee, S. Y. Lee, and Y. S. Jung, "Excellent Compatibility of Solvate Ionic Liquids with Sulfide Solid Electrolytes: Toward Favorable Ionic Contacts in Bulk-Type All-Solid-State Lithium-Ion Batteries," *Advanced Energy Materials*, vol. 5, no. 22, p. 1500865, 2015.

[93] S. Yubuchi, M. Uematsu, M. Deguchi, A. Hayashi, and M. Tatsumisago, "Lithium-Ion-Conducting Argyrodite-Type Li_6PS_5X (X = Cl, Br, I) Solid Electrolytes Prepared by a Liquid-Phase Technique Using Ethanol as a Solvent," *ACS Applied Energy Materials*, vol. 1, no. 8, p. 3622–3629, 2018.

[94] S. Yubuchi, S. Teragawa, K. Aso, K. Tadanaga, A. Hayashi, and M. Tatsumisago, "Preparation of high lithium-ion conducting Li_6PS_5Cl solid electrolyte from ethanol solution for all-solid-state lithium batteries," *Journal of Power Sources*, vol. 293, pp. 941–945, 2015.

[95] N. C. Rosero-Navarro, A. Miura, and K. Tadanaga, "Composite cathode prepared by argyrodite precursor solution assisted by dispersant agents for bulk-type all-solid-state batteries," *Journal of Power Sources*, vol. 396, pp. 33–40, 2018.

[96] N. C. Rosero-Navarro, T. Kinoshita, A. Miura, M. Higuchi, and K. Tadanaga, "Effect of the binder content on the electrochemical performance of composite cathode using Li_6PS_5Cl precursor solution in an all-solid-state lithium battery," *Ionics*, vol. 23, no. 6, pp. 1619–1624, 2017.

[97] F. Han, J. Yue, X. Fan, T. Gao, C. Luo, Z. Ma, L. Suo, and C. Wang, "High-performance all-solid-state lithium-sulfur battery enabled by a mixed-conductive Li_2S nanocomposite," *Nano Letters*, vol. 16, no. 7, pp. 4521–4527, 2016.

[98] M. Yamamoto, Y. Terauchi, A. Sakuda, and M. Takahashi, "Binder-free sheet-type all-solid-state batteries with enhanced rate capabilities and high energy densities," *Scientific Reports*, vol. 8, no. 1, pp. 2–11, 2018.

[99] D. H. Tan, A. Banerjee, Z. Deng, E. A. Wu, H. Nguyen, J. M. Doux, X. Wang, J. H. Cheng, S. P. Ong, Y. S. Meng, and Z. Chen, "Enabling Thin and Flexible Solid-State Composite Electrolytes by the Scalable Solution Process," *ACS Applied Energy Materials*, vol. 2, no. 9, pp. 6542–6550, 2019.

[100] Y. J. Nam, S. J. Cho, D. Y. Oh, J. M. Lim, S. Y. Kim, J. H. Song, Y. G. Lee, S. Y. Lee, and Y. S. Jung, "Bendable and thin sulfide solid electrolyte film: A new electrolyte opportunity for free-standing and stackable high-energy all-solid-state lithium-ion batteries," *Nano Letters*, vol. 15, no. 5, pp. 3317–3323, 2015.

[101] S. Choi, J. Ann, J. Do, S. Lim, C. Park, and D. Shin, "Application of Rod-Like Li_6PS_5Cl Directly Synthesized by a Liquid Phase Process to Sheet-Type Electrodes for All-Solid-State Lithium Batteries," *Journal of The Electrochemical Society*, vol. 166, no. 3, pp. A5193–A5200, 2019.

[102] M. Yamamoto, M. Takahashi, Y. Terauchi, Y. Kobayashi, S. Ikeda, and A. Sakuda, "Fabrication of Composite Positive Electrode Sheet with High Active Material Content and Effect of Fabrication Pressure for All-Solid-State Battery," *Journal of the Ceramic Society of Japan*, vol. 125, no. 5, pp. 391–395, 2017.

[103] D. Y. Oh, D. H. Kim, S. H. Jung, J. G. Han, N. S. Choi, and Y. S. Jung, "Single-step wet-chemical fabrication of sheet-type electrodes from solid-electrolyte precursors for all-solid-state lithium-ion batteries," *Journal of Materials Chemistry A*, vol. 5, no. 39, pp. 20771–20779, 2017.

[104] S. Ito, S. Fujiki, T. Yamada, Y. Aihara, Y. Park, T. Y. Kim, S. W. Baek, J. M. Lee, S. Doo, and N. Machida, "A rocking chair type all-solid-state lithium ion battery adopting Li_2O-ZrO_2 coated $LiNi_{0.8}Co_{0.15}Al_{0.05}O_2$ and a sulfide based electrolyte," *Journal of Power Sources*, vol. 248, pp. 943–950, 2014.

[105] X. Yao, N. Huang, F. Han, Q. Zhang, H. Wan, J. P. Mwizerwa, C. Wang, and X. Xu, "High-Performance All-Solid-State Lithium–Sulfur Batteries Enabled by Amorphous Sulfur-Coated Reduced Graphene Oxide Cathodes," *Advanced Energy Materials*, vol. 7, no. 17, p. 1602923, 2017.

[106] C. Yu, L. van Eijck, S. Ganapathy, and M. Wagemaker, "Synthesis, structure and electrochemical performance of the argyrodite Li_6PS_5Cl solid electrolyte for Li-ion solid state batteries," *Electrochimica Acta*, vol. 215, pp. 93–99, 2016.

[107] S. Wang, Y. Zhang, X. Zhang, T. Liu, Y. Lin, Y. Shen, L. Li, and C. Nan, "High-Conductivity Argyrodite Li_6PS_5Cl Solid Electrolytes Prepared via Optimizing Sintering Processes for All-Solid-State Lithium-Sulfur Batteries," *ACS Applied Materials & Interfaces*, vol. 10, no. 49, pp. 42279–42285, 2018.

[108] S. Ohno, R. Koerver, G. Dewald, C. Rosenbach, P. Titscher, D. Steckermeier, A. Kwade, J. Janek, and W. G. Zeier, "Observation of chemo-mechanical failure and influence of cut-off potentials in all-solid-state Li-S batteries," *Chemistry of Materials*, vol. 31, no. 8, pp. 2930–2940, 2019.

[109] S. Boulineau, J. M. Tarascon, V. Seznec, and V. Viallet, "Electrochemical properties of all-solid-state lithium secondary batteries using Li-argyrodite Li_6PS_5Cl as solid electrolyte," *Materials Research Society Symposium Proceedings*, vol. 1496, pp. 7–12, 2013.

[110] H. U. Choi, J. S. Jin, J. Y. Park, and H. T. Lim, "Performance improvement of all-solid-state Li-S batteries with optimizing morphology and structure of sulfur composite electrode," *Journal of Alloys and Compounds*, vol. 723, pp. 787–794, 2017.

[111] F. Hippauf, B. Schumm, S. Doerfler, H. Althues, S. Fujiki, T. Shiratsushi, T. Tsujimura, Y. Aihara, and S. Kaskel, "Overcoming binder limitations of sheet-type solid-state cathodes using a solvent-free dry-film approach," *Energy Storage Materials*, vol. 21, pp. 390–398, 2019.

[112] Z. Zhang, L. Wu, D. Zhou, W. Weng, and X. Yao, "Flexible Sulfide Electrolyte Thin Membrane with Ultrahigh Ionic Conductivity for All-Solid-State Lithium Batteries," *Nano Letters*, vol. 21, no. 12, pp. 5233–5239, 2021.

[113] K. K. Fu, Y. Gong, G. T. Hitz, D. W. McOwen, Y. Li, S. Xu, Y. Wen, L. Zhang, C. Wang, G. Pastel, J. Dai, B. Liu, H. Xie, Y. Yao, E. D. Wachsman, and L. Hu, "Three-dimensional bilayer garnet solid electrolyte based high energy density lithium metal–sulfur batteries," *Energy Environ. Sci.*, vol. 10, no. 7, pp. 1568–1575, 2017.

[114] S. Xu, D. W. McOwen, L. Zhang, G. T. Hitz, C. Wang, Z. Ma, C. Chen, W. Luo, J. Dai, Y. Kuang, E. M. Hitz, K. Fu, Y. Gong, E. D. Wachsman, and L. Hu, "All-in-one lithium-sulfur battery enabled by a porous-dense-porous garnet architecture," *Energy Storage Materials*, vol. 15, pp. 458–464, 2018.

[115] C. Yang, L. Zhang, B. Liu, S. Xu, T. Hamann, D. McOwen, J. Dai, W. Luo, Y. Gong, E. D. Wachsman, and L. Hu, "Continuous plating/stripping behavior of solid-state lithium metal anode in a 3D ion-conductive framework," *Proceedings of the National Academy of Sciences*, vol. 115, no. 15, pp. 3770–3775, 2018.

[116] C. Wang, X. Wang, Y. Yang, A. Kushima, J. Chen, Y. Huang, and J. Li, "Slurryless Li_2S/reduced graphene oxide cathode paper for high-performance lithium sulfur battery," *Nano Letters*, vol. 15, no. 3, pp. 1796–1802, 2015.

[117] D. H. Kim, D. Y. Oh, K. H. Park, Y. E. Choi, Y. J. Nam, H. A. Lee, S.-m. Lee, and Y. S. Jung, "Infiltration of Solution-Processable Solid Electrolytes into Conventional Li-Ion-Battery Electrodes for All-Solid-State Li-Ion Batteries," *Nano Letters*, vol. 17, no. 5, pp. 3013–3020, 2017.

[118] D. H. Kim, H. A. Lee, Y. B. Song, J. W. Park, S. M. Lee, and Y. S. Jung, "Sheet-type Li_6PS_5 Cl-infiltrated Si anodes fabricated by solution process for all-solid-state lithium-ion batteries," *Journal of Power Sources*, vol. 426, pp. 143–150, 2019.

[119] X. Yao, D. Liu, C. Wang, P. Long, G. Peng, Y. S. Hu, H. Li, L. Chen, and X. Xu, "High-Energy All-Solid-State Lithium Batteries with Ultralong Cycle Life," *Nano Letters*, vol. 16, no. 11, pp. 7148–7154, 2016.

[120] A. Hwang, Y. Ma, Y. Cao, Q. Li, L. Wang, X. Cheng, P. Zuo, and C. Du, "Fabrication and Electrochemical Properties of $Li_4Ti_5O_{12}$ @ Li_6PS_5Cl for All-solid-state Lithium Batteries using Simple Mechanical Method," *International Journal of Electrochemical Science*, vol. 12, pp. 7795–7806, 2017.

[121] M. L. Stewart, "A Computational Approach for Evaluating Helical Compression Springs," *International Journal of Research in Engineering and Technology*, vol. 3, no. 12, pp. 224–229, 2014.

[122] R. Raccichini, M. Amores, and G. Hinds, "Critical review of the use of reference electrodes in li-ion batteries: A diagnostic perspective," *Batteries*, vol. 5, no. 1, pp. 1–24, 2019.

[123] A. J. Bard and L. R. Faulkner, *Electrochemical Methods: Fundamentals and Applications*. Wiley, 2nd ed., 2001.

[124] P. Vadhva, J. Hu, M. J. Johnson, R. Stocker, M. Braglia, D. J. Brett, and A. J. Rettie, "Electrochemical Impedance Spectroscopy for All-Solid-State Batteries: Theory, Methods and Future Outlook," *ChemElectroChem*, vol. 8, no. 11, pp. 1930–1947, 2021.

[125] J. A. Dawson, P. Canepa, M. J. Clarke, T. Famprikis, D. Ghosh, and M. S. Islam, "Toward Understanding the Different Influences of Grain Boundaries on Ion Transport in Sulfide and Oxide Solid Electrolytes," *Chemistry of Materials*, vol. 31, no. 14, pp. 5296–5304, 2019.

[126] M. Pasta, D. Armstrong, Z. L. Brown, J. Bu, M. R. Castell, P. Chen, A. Clocks, S. A. Corr, E. J. Cussen, E. Darnbrough, V. Deshpande, C. Doerrer, M. S. Dyer, H. El-shinawi, N. Fleck, J. T. S. Irvine, H. J. Lee, G. Li, E. Liberti, I. Mcclelland, C. Monroe, P. D. Nellist, P. R. Shearing, E. Shoko, W. Song, D. S. Jolly, C. I. Thomas, S. J. Turrell, M. Vestli, C. K. Williams, Y. Zhou, and P. G. Bruce, "2020 Roadmap on Solid-State Batteries," *Journal of Physics: Energy*, vol. 2, no. 3, p. 32008, 2020.

[127] D. Cao, Y. Zhao, X. Sun, A. Natan, Y. Wang, P. Xiang, W. Wang, and H. Zhu, "Processing Strategies to Improve Cell-Level Energy Density of Metal Sulfide Electrolyte-Based All-Solid-State Li Metal Batteries and Beyond," *ACS Energy Letters*, vol. 5, pp. 3468–3489, 2020.

[128] S. H. Jung, U. H. Kim, J. H. Kim, S. Jun, C. S. Yoon, Y. S. Jung, and Y. K. Sun, "Ni-Rich Layered Cathode Materials with Electrochemo-Mechanically Compliant Microstructures for All-Solid-State Li Batteries," *Advanced Energy Materials*, vol. 10, no. 6, p. 1903360, 2019.

[129] L. Zhou, C. Y. Kwok, A. Shyamsunder, Q. Zhang, X. Wu, and L. Nazar, "A new halospinel superionic conductor for high-voltage all solid state lithium batteries," *Energy & Environmental Science*, vol. 13, pp. 2056–2063, 2020.

[130] R. Ruess, S. Schweidler, H. Hemmelmann, G. Conforto, A. Bielefeld, D. A. Weber, J. Sann, M. T. Elm, and J. Janek, "Influence of NCM Particle Cracking on Kinetics of Lithium-Ion Batteries with Liquid or Solid Electrolyte," *Journal of The Electrochemical Society*, vol. 167, no. 10, p. 100532, 2020.

[131] Qian, G.; Zhang, Y.; Li, L.; Zhang, R.; Xu, J.; Cheng, Z.; Xie, S.; Wang, H.; Rao, Q.; He, Y. et al, "Single-crystal Nickel-Rich Layered-Oxide Battery Cathode Materials: Synthesis, Electrochemistry, and Intra-Granular Fracture," *Energy Storage Materials*, vol. 27, pp. 140–149, 2020.

[132] X. Fan, G. Hu, B. Zhang, X. Ou, J. Zhang, W. Zhao, H. Jia, L. Zou, P. Li, and Y. Yang, "Crack-Free Single-Crystalline Ni-Rich Layered NCM Cathode Enable Superior Cycling Performance of Lithium-Ion Batteries," *Nano Energy*, vol. 70, p. 104450, 2020.

[133] C. Wang, R. Yu, S. Hwang, J. Liang, X. Li, C. Zhao, Y. Sun, J. Wang, N. Holmes, R. Li, H. Huang, S. Zhao, L. Zhang, S. Lu, D. Su, and X. Sun, "Single Crystal Cathodes Enabling High-performance All-Solid-State Lithium-Ion Batteries," *Energy Storage Materials*, vol. 30, pp. 98–103, 2020.

[134] X. Li, W. Peng, R. Tian, D. Song, Z. Wang, H. Zhang, L. Zhu, and L. Zhang, "Excellent Performance Single-Crystal NCM Cathode under High Mass Loading for All-Solid-State Lithium Batteries," *Electrochimica Acta*, vol. 363, p. 137185, 2020.

[135] X. Liu, B. Zheng, J. Zhao, W. Zhao, Z. Liang, Y. Su, C. Xie, K. Zhou, Y. Xiang, J. Zhu, H. Wang, G. Zhong, Z. Gong, J. Huang, and Y. Yang, "Electrochemo-Mechanical Effects on Structural Integrity of Ni-Rich Cathodes with Different Microstructures in All Solid-State Batteries," *Advanced Energy Materials*, vol. 11, no. 8, p. 2003583, 2021.

[136] L. De Biasi, A. O. Kondrakov, H. Geßwein, T. Brezesinski, P. Hartmann, and J. Janek, "Between Scylla and Charybdis: Balancing among Structural Stability and Energy Density of Layered NCM Cathode Materials for Advanced Lithium-Ion Batteries," *Journal of Physical Chemistry C*, vol. 121, no. 47, pp. 26163–26171, 2017.

[137] G. Gabrielli, P. Axmann, T. Diemant, and J. Behm, "Combining Optimized Particle Morphology with a Niobium-Based Coating for Long Cycling-Life, High-Voltage Lithium-Ion Batteries," *ChemSusChem*, vol. 9, pp. 1670–1679, 2016.

[138] K. J. Kim, M. Balaish, M. Wadaguchi, L. Kong, and J. L. Rupp, "Solid-State Li–Metal Batteries: Challenges and Horizons of Oxide and Sulfide Solid Electrolytes and Their Interfaces," *Advanced Energy Materials*, vol. 11, no. 1, p. 2002689, 2021.

[139] D. S. Jolly, Z. Ning, G. O. Hartley, B. Liu, D. L. R. Melvin, P. Adamson, J. Marrow, and P. G. Bruce, "Temperature Dependence of Lithium Anode Voiding

in Argyrodite Solid-State Batteries," *ACS Applied Materials and Interfaces*, vol. 13, pp. 22708–22716, 2021.

[140] A. Banerjee, H. Tang, X. Wang, J. H. Cheng, H. Nguyen, M. Zhang, D. H. Tan, T. A. Wynn, E. A. Wu, J. M. Doux, T. Wu, L. Ma, G. E. Sterbinsky, M. S. D'Souza, S. P. Ong, and Y. S. Meng, "Revealing Nanoscale Solid-Solid Interfacial Phenomena for Long-Life and High-Energy All-Solid-State Batteries," *ACS Applied Materials and Interfaces*, vol. 11, no. 46, pp. 43138–43145, 2019.

[141] T. K. Schwietert, V. A. Arszelewska, C. Wang, C. Yu, A. Vasileiadis, N. J. J. de Klerk, J. Hageman, T. Hupfer, I. Kerkamm, Y. Xu, E. van der Maas, E. M. Kelder, S. Ganapathy, and M. Wagemaker, "Clarifying the Relationship Between Redox Activity and Electrochemical Stability in Solid Electrolytes," *Nature Materials*, vol. 19, no. 4, pp. 428–435, 2020.

[142] D. H. S. Tan, E. A. Wu, H. Nguyen, Z. Chen, M. A. T. Marple, J.-m. Doux, X. Wang, H. Yang, A. Banerjee, and Y. S. Meng, "Elucidating Reversible Electrochemical Redox of Li_6PS_5Cl Solid Electrolyte," *ACS Energy Letters*, vol. 4, pp. 2418–2427, 2019.

[143] Y. Zhou, C. Doerrer, J. Kasemchainan, P. G. Bruce, M. Pasta, and L. Hardwick, "Observation of Interfacial Degradation of Li_6PS_5Cl against Lithium Metal and $LiCoO_2$ via In Situ Electrochemical Raman Microscopy," *Batteries & Supercaps*, vol. 3, pp. 647–652, 2020.

[144] C. Ghanty, B. Markovsky, E. M. Erickson, M. Talianker, O. Haik, Y. Tal-Yossef, A. Mor, D. Aurbach, J. Lampert, A. Volkov, J.-Y. Shin, A. Garsuch, F. F. Chesneau, and C. Erk, "Li^+-Ion Extraction/Insertion of Ni-Rich $Li_{1+x}(Ni_yCo_zMn_z)_wO_2$($0.005<x<0.03$; y:z=8:1, $w\approx1$) Electrodes: In Situ XRD and Raman Spectroscopy Study," *ChemElectroChem*, vol. 2, no. 10, pp. 1479–1486, 2015.

[145] P. Li, Y. Zhao, Y. Shen, and S.-H. Bo, "Fracture Behavior in Battery Materials," *Journal of Physics: Energy*, vol. 2, no. 2, p. 022002, 2020.

[146] J. M. Doux, H. Nguyen, D. H. Tan, A. Banerjee, X. Wang, E. A. Wu, C. Jo, H. Yang, and Y. S. Meng, "Stack Pressure Considerations for Room-Temperature All-Solid-State Lithium Metal Batteries," *Advanced Energy Materials*, vol. 10, no. 1, p. 1903253, 2020.

[147] C. Hänsel, P. V. Kumar, and D. Kundu, "Stack Pressure Effect in Li_3PS_4 and Na_3PS_4 Based Alkali Metal Solid-State Cells: The Dramatic Implication of Interlayer Growth," *Chemistry of Materials*, vol. 32, no. 24, pp. 10501–10510, 2020.

[148] Y. Han, S. H. Jung, H. Kwak, S. Jun, H. H. Kwak, J. H. Lee, S.-t. Hong, and Y. S. Jung, "Single- or Poly-Crystalline Ni-Rich Layered Cathode, Sulfide or Halide Solid Electrolyte: Which Will be the Winners for All-Solid-State Batteries?," *Advanced Energy Materials*, vol. 11, no. 21, p. 2100126, 2021.

[149] J. M. Doux, Y. Yang, D. H. Tan, H. Nguyen, E. A. Wu, X. Wang, A. Banerjee, and Y. S. Meng, "Pressure Effects on Sulfide Electrolytes for All Solid-State Batteries," *Journal of Materials Chemistry A*, vol. 8, no. 10, pp. 5049–5055, 2020.

[150] Y. K. Sun, "Promising All-Solid-State Batteries for Future Electric Vehicles," *ACS Energy Letters*, vol. 5, no. 10, pp. 3221–3223, 2020.

[151] P. Adeli, J. D. Bazak, K. H. Park, I. Kochetkov, A. Huq, G. R. Goward, and L. F. Nazar, "Boosting Solid-State Diffusivity and Conductivity in Lithium Superionic Argyrodites by Halide Substitution," *Angewandte Chemie - International Edition*, vol. 58, no. 26, pp. 8681–8686, 2019.

[152] R. Pfenninger, M. Struzik, I. Garbayo, E. Stilp, and J. L. Rupp, "A low ride on processing temperature for fast lithium conduction in garnet solid-state battery films," *Nature Energy*, vol. 4, no. 6, pp. 475–483, 2019.

[153] B. S. Vishnugopi, E. Kazyak, J. A. Lewis, J. Nanda, M. T. Mcdowell, N. P. Dasgupta, and P. P. Mukherjee, "Challenges and Opportunities for Fast Charging of Solid-State Lithium Metal Batteries," *ACS Energy Letters*, vol. 6, no. 10, pp. 3734–3749, 2021.

[154] S. Randau, D. A. Weber, O. Kötz, R. Koerver, P. Braun, A. Weber, E. Ivers-Tiffée, T. Adermann, J. Kulisch, W. G. Zeier, F. H. Richter, and J. Janek, "Benchmarking the performance of all-solid-state lithium batteries," *Nature Energy*, vol. 5, pp. 1–12, 2020.

[155] Y. Liu, Y. Zhu, and Y. Cui, "Challenges and opportunities towards fast-charging battery materials," *Nature Energy*, vol. 4, no. 7, pp. 540–550, 2019.

[156] M. Weiss, R. Ruess, J. Kasnatscheew, Y. Levartovsky, N. R. Levy, P. Minnmann, L. Stolz, T. Waldmann, M. Wohlfahrt-Mehrens, D. Aurbach, M. Winter, Y. Ein-Eli, and J. Janek, "Fast Charging of Lithium-Ion Batteries: A Review of Materials Aspects," *Advanced Energy Materials*, vol. 11, no. 33, p. 2101126, 2021.

[157] D. H. S. Tan, Y.-t. Chen, H. Yang, W. Bao, B. Sreenarayanan, J.-m. Doux, W. Li, B. Lu, S.-y. Ham, B. Sayahpour, J. Scharf, E. A. Wu, G. Deysher, H. E. Han, H. J. Hah, H. Jeong, J. B. Lee, L. Si, and L. Si, "Carbon-free high-loading silicon anodes enabled by sulfide solid electrolytes," *Science*, vol. 1499, pp. 1494–1499, 2021.

[158] L. Ye and X. Li, "A dynamic stability design strategy for lithium metal solid state batteries," *Nature*, vol. 593, 2021.

[159] C. Bauer, S. Burkhardt, N. P. Dasgupta, L. A. W. Ellingsen, L. L. Gaines, H. Hao, R. Hischier, L. Hu, Y. Huang, J. Janek, C. Liang, H. Li, J. Li, Y. Li, Y. C. Lu, W. Luo, L. F. Nazar, E. A. Olivetti, J. F. Peters, J. L. Rupp, M. Weil, J. F. Whitacre, and S. Xu, "Charging sustainable batteries," *Nature Sustainability*, vol. 5, no. 3, pp. 176–178, 2022.

[160] C. P. Grey and J. M. Tarascon, "Sustainability and in situ monitoring in battery development," *Nature Materials*, vol. 16, no. 1, pp. 45–56, 2016.

[161] Z. Yang, H. Huang, and F. Lin, "Sustainable Electric Vehicle Batteries for a Sustainable World: Perspectives on Battery Cathodes, Environment, Supply Chain, Manufacturing, Life Cycle, and Policy," *Advanced Energy Materials*, vol. 12, no. 26, p. 2200383, 2022.

[162] P. Minnmann, F. Strauss, A. Bielefeld, R. Ruess, P. Adelhelm, S. Burkhardt, S. L. Dreyer, E. Trevisanello, H. Ehrenberg, T. Brezesinski, F. H. Richter, and J. Janek, "Designing Cathodes and Cathode Active Materials for Solid-State Batteries," *Advanced Energy Materials*, vol. 12, no. 35, p. 2201425, 2022.

[163] A. Bielefeld, D. A. Weber, R. Rueß, V. Glavas, and J. Janek, "Influence of Lithium Ion Kinetics, Particle Morphology and Voids on the Electrochemical Performance of Composite Cathodes for All-Solid-State Batteries," *Journal of The Electrochemical Society*, vol. 169, no. 2, p. 020539, 2022.

[164] C. Doerrer, I. Capone, S. Narayanan, J. Liu, C. R. M. Grovenor, M. Pasta, and P. S. Grant, "High Energy Density Single-Crystal NMC/Li_6PS_5Cl Cathodes for All-Solid-State Lithium-Metal Batteries," *ACS Applied Materials and Interfaces*, vol. 13, no. 31, pp. 37809–37815, 2021.

[165] J. E. Harlow, X. Ma, J. Li, E. Logan, Y. Liu, N. Zhang, L. Ma, S. L. Glazier, M. M. E. Cormier, M. Genovese, S. Buteau, A. Cameron, J. E. Stark, and J. R. Dahn, "A Wide Range of Testing Results on an Excellent Lithium-Ion Cell Chemistry to be used as Benchmarks for New Battery Technologies," *Journal of The Electrochemical Society*, vol. 166, no. 13, pp. A3031–A3044, 2019.

[166] A. Ikezawa, G. Fukunishi, T. Okajima, F. Kitamura, K. Suzuki, M. Hirayama, R. Kanno, and H. Arai, "Performance of $Li_4Ti_5O_{12}$-based Reference Electrode for the Electrochemical Analysis of All-solid-state Lithium-ion Batteries," *Electrochemistry Communications*, vol. 116, p. 106743, 2020.

[167] R. Dugas, Y. Dupraz, E. Quemin, T. Koç, and J.-M. Tarascon, "Engineered Three-Electrode Cells for Improving Solid State Batteries," *Journal of The Electrochemical Society*, vol. 168, no. 9, p. 090508, 2021.

[168] T. Shi, Y.-Q. Zhang, Q. Tu, Y. Wang, M. C. Scott, and G. Ceder, "Characterization of mechanical degradation in an all-solid-state battery cathode," *Journal of Materials Chemistry A*, vol. 8, pp. 17399–17404, 2020.

[169] X. Gao, B. Liu, B. Hu, Z. Ning, D. S. Jolly, S. Zhang, J. Perera, J. Bu, J. Liu, C. Doerrer, E. Darnbrough, D. Armstrong, P. S. Grant, and P. G. Bruce, "Solid-state lithium battery cathodes operating at low pressures," *Joule*, vol. 6, no. 3, pp. 636–646, 2022.

[170] L. Zhou, T.-t. Zuo, C. Y. Kwok, S. Y. Kim, A. Assoud, Q. Zhang, J. Janek, and L. F. Nazar, "High areal capacity, long cycle life 4 V ceramic all-solid-state Li-ion batteries enabled by chloride solid electrolytes," *Nature Energy*, vol. 2, 2022.

[171] K. G. Gallagher, S. E. Trask, C. Bauer, T. Woehrle, S. F. Lux, M. Tschech, P. Lamp, B. J. Polzin, S. Ha, B. Long, Q. Wu, W. Lu, D. W. Dees, and A. N. Jansen, "Optimizing Areal Capacities through Understanding the Limitations of Lithium-Ion Electrodes," *Journal of The Electrochemical Society*, vol. 163, no. 2, pp. A138–A149, 2016.

[172] W. Zhang, F. H. Richter, S. P. Culver, T. Leichtweiss, J. G. Lozano, C. Dietrich, P. G. Bruce, W. G. Zeier, and J. Janek, "Degradation Mechanisms at the $Li_{10}GeP_2S_{12}$/$LiCoO_2$Cathode Interface in an All-Solid-State Lithium-Ion Battery," *ACS Applied Materials and Interfaces*, vol. 10, no. 26, pp. 22226–22236, 2018.

[173] E. Trevisanello, R. Ruess, G. Conforto, F. H. Richter, and J. Janek, "Polycrystalline and Single Crystalline NCM Cathode Materials—Quantifying Particle Cracking, Active Surface Area, and Lithium Diffusion," *Advanced Energy Materials*, vol. 11, p. 2003400, 2021.

[174] C. Wang, R. Yu, H. Duan, Q. Lu, Q. Li, K. R. Adair, D. Bao, Y. Liu, R. Yang, J. Wang, S. Zhao, H. Huang, and X. Sun, "Solvent-Free Approach for Interweaving Freestanding and Ultrathin Inorganic Solid Electrolyte Membranes," *ACS Energy Letters*, vol. 7, no. 1, pp. 410–416, 2022.

[175] X. Yang, K. R. Adair, X. Gao, and X. Sun, "Recent advances and perspectives on thin electrolytes for high-energy-density solid-state lithium batteries," *Energy and Environmental Science*, vol. 14, no. 2, pp. 643–671, 2021.

[176] G. L. Zhu, C. Z. Zhao, H. J. Peng, H. Yuan, J. K. Hu, H. X. Nan, Y. Lu, X. Y. Liu, J. Q. Huang, C. He, J. Zhang, and Q. Zhang, "A Self-Limited Free-Standing Sulfide Electrolyte Thin Film for All-Solid-State Lithium Metal Batteries," *Advanced Functional Materials*, vol. 31, no. 32, p. 2101985, 2021.

[177] S. Wang, X. Zhang, S. Liu, C. Xin, C. Xue, F. Richter, L. Li, L. Fan, Y. Lin, Y. Shen, J. Janek, and C.-w. Nan, "High-conductivity free-standing Li_6PS_5Cl/poly(vinylidene difluoride) composite solid electrolyte membranes for lithium-ion batteries," *Journal of Materiomics*, vol. 6, no. 1, pp. 70–76, 2020.

[178] D. H. Kim, Y.-h. Lee, Y. B. Song, H. Kwak, and S.-y. Lee, "Thin and Flexible Solid Electrolyte Membranes with Ultrahigh Thermal Stability Derived from Solution-Processable Li Argyrodites for All-Solid-State Li-Ion Batteries," *ACS Energy Letters*, vol. 5, no. 3, pp. 718–727, 2020.

[179] D. H. S. Tan, Y. S. Meng, and J. Jang, "Scaling up high-energy-density sulfidic solid-state batteries: A lab-to-pilot perspective," *Joule*, vol. 6, no. 8, pp. 1755–1769, 2022.

[180] W. Ping, C. Wang, R. Wang, Q. Dong, Z. Lin, A. H. Brozena, J. Dai, J. Luo, and L. Hu, "Printable, high-performance solid-state electrolyte films," *Science Advances*, vol. 6, no. 47, p. eabc8641, 2020.

[181] J. Bu, P. Leung, C. Huang, S. H. Lee, and P. S. Grant, "Co-spray printing of $LiFePO_4$ and PEO-$Li_{1.5}Al_{0.5}Ge_{1.5}(PO_4)_3$ hybrid electrodes for all-solid-state Li-ion battery applications," *Journal of Materials Chemistry A*, vol. 7, pp. 19094–19103, 2019.

[182] J. D. Evans, Y. Sun, and P. S. Grant, "Sequential Deposition of Integrated Cathode - Inorganic Separator - Anode Multilayers for High Performance Li-Ion Batteries," *ACS Applied Materials & Interfaces*, vol. 14, no. 30, pp. 34538–34551, 2022.

[183] S. Yubuchi, H. Tsukasaki, A. Sakuda, S. Mori, A. Hayashi, and M. Tatsumisago, "Quantitative analysis of crystallinity in an argyrodite sulfide-based solid electrolyte synthesized via solution processing," *RSC Advances*, vol. 9, no. 25, pp. 14465–14471, 2019.

[184] W. D. Jung, J.-S. Kim, Y. J. Kim, H. Jeong, D. Han, K.-W. Nam, D. Ahn, D.-H. Kwon, H.-G. Jung, J.-H. Lee, and H. Kim, "Annealing-free thioantimonate argyrodites with high li-ion conductivity and low elastic modulus," *Advanced Functional Materials*, p. 2211185, 2022.

[185] H. Zhou, F. Xin, B. Pei, and M. S. Whittingham, "What Limits the Capacity of Layered Oxide Cathodes in Lithium Batteries?," *ACS Energy Letters*, vol. 4, no. 8, pp. 1902–1906, 2019.

[186] R. Diehm, J. Kumberg, C. Dörrer, M. Müller, W. Bauer, P. Scharfer, and W. Schabel, "In Situ Investigations of Simultaneous Two-Layer Slot Die Coating of Component-Graded Anodes for Improved High-Energy Li-Ion Batteries," *Energy Technology*, vol. 8, no. 5, p. 1901251, 2020.

[187] W. Z. Huang, C. Z. Zhao, P. Wu, H. Yuan, W. E. Feng, Z. Y. Liu, Y. Lu, S. Sun, Z. H. Fu, J. K. Hu, S. J. Yang, J. Q. Huang, and Q. Zhang, "Anode-Free Solid-State Lithium Batteries: A Review," *Advanced Energy Materials*, vol. 12, no. 26, p. 2201044, 2022.

[188] L. Xu, Y. Lu, C. Z. Zhao, H. Yuan, G. L. Zhu, L. P. Hou, Q. Zhang, and J. Q. Huang, "Toward the Scale-Up of Solid-State Lithium Metal Batteries: The Gaps between Lab-Level Cells and Practical Large-Format Batteries," *Advanced Energy Materials*, vol. 11, no. 4, p. 2002360, 2021.

[189] J. H. Teo, F. Strauss, D. Tripkovic, S. Schweidler, Y. Ma, M. Bianchini, J. Janek, and T. Brezesinski, "Design-of-experiments-guided optimization of slurry-cast cathodes for solid-state batteries," *Cell Reports Physical Science*, vol. 2, no. 6, p. 100465, 2021.

[190] X. Xing, Y. Li, S. Wang, H. Liu, Z. Wu, S. Yu, J. Holoubek, H. Zhou, and P. Liu, "Graphite-Based Lithium-Free 3D Hybrid Anodes for High Energy Density All-Solid- State Batteries," *ACS Energy Letters*, vol. 6, pp. 1831–1838, 2021.

[191] J. Su, M. Pasta, Z. Ning, X. Gao, P. G. Bruce, and C. R. M. Grovenor, "Interfacial modification between argyrodite-type solid-state electrolytes and Li metal anodes using LiPON Interlayers," *Energy and Environmental Science*, vol. 15, pp. 3805–3814, 2022.

[192] Z. Ning, D. S. Jolly, G. Li, R. De Meyere, S. D. Pu, Y. Chen, J. Kasemchainan, J. Ihli, C. Gong, B. Liu, D. L. Melvin, A. Bonnin, O. Magdysyuk, P. Adamson, G. O. Hartley, C. W. Monroe, T. J. Marrow, and P. G. Bruce, "Visualizing plating-induced cracking in lithium-anode solid-electrolyte cells," *Nature Materials*, vol. 20, no. 8, pp. 1121–1129, 2021.